Assessing the Alterations In Berea Sandstone Mechanical Properties Induced by the Permeation of Bentonite Gels of Varying NaCl Concentrations: A Wellbore Strengthening Perspective

KARL EERIK KRAAVI

Assessing the Alterations In Berea Sandstone Mechanical Properties Induced by the Permeation of Bentonite Gels of Varying NaCl Concentrations: A Wellbore Strengthening Perspective

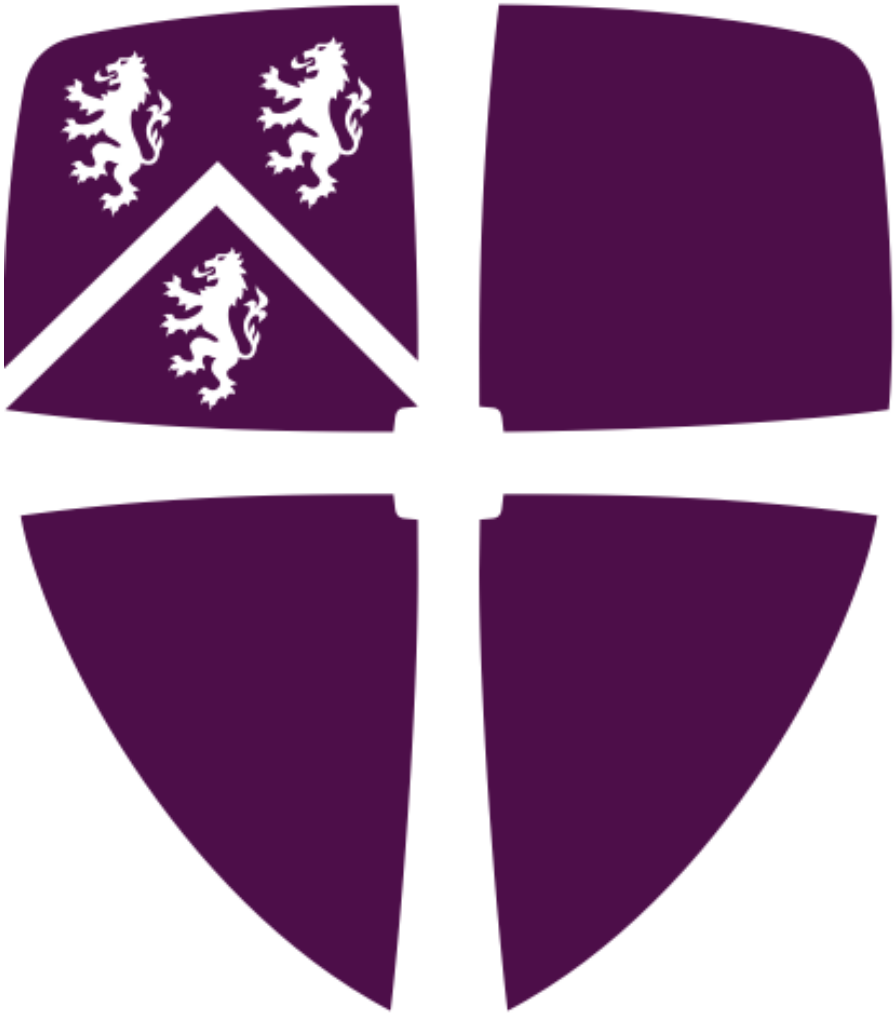

Karl Eerik Kraavi

This thesis is submitted in partial fulfilment of the requirements for the degree of Master of Science by Research

Supervisor:

Prof. H. Chris Greenwell

Department of Earth Sciences, Durham University

October 2022

I hereby declare that all information in this document has been obtained and presented in accordance with academic rules and ethical conduct. I also declare that I have fully cited and referenced all material, and results, that are not original to this work

Karl Eerik Kraavi

Abstract

Lost circulation, which is the loss of drilling fluid into a formation during drilling, is commonly induced by wellbore pressure exceeding that of the fracture initiation pressure (FIP) and fracture propagation pressure (FPP) of the formation. This expensive occurrence can be mitigated by increasing the FIP and FPP by altering the drilling fluid composition, which has a large effect on the mechanical behaviour of rock and subsequently on the FIP and FPP. Bentonite is used both as a base fluid, as well as a lost circulation material. It is therefore imperative to understand the effect that bentonite, at different swelling capacities, has on the mechanical properties of rock to optimise its use in drilling operations to better attenuate lost circulation. In this study, Berea sandstone cores, of four permeability ranges, were permeated with bentonite gels of four NaCl concentrations, using a novel apparatus. Two batches of gel-permeated cores were prepared, one set was allowed to dry, to observe an ageing effect, and the other was kept at 4°C to preserve moisture. The cores were then indented to obtain stress-strain curves. The results of the indentation testing showed a statistically significant increase in peak strength and Young's modulus in the wet gel-permeated cores relative to the non-permeated samples, whereas the cores with the dried gel displayed a decrease in these properties compared to the control, The dry gel-permeated cores, however, exhibited a significantly longer displacement distance compared to the control, implying these cores take longer to fully fracture apart. In addition to indentation, viscometry experiments were carried out to assess the rheological properties of the gels, this, alongside SEM and CT imaging of the samples, was done in an attempt to understand potential mechanisms behind the alterations in mechanical properties caused by gel permeation. The research carried out shows an initial set of promising results for the use of bentonite gels for wellbore-strengthening

applications during drilling. The work undertaken also highlights the need for future research into interactions between non-Newtonian fluids and solids, and the potential that these interactions provide in altering the physicochemical properties of materials.

Acknowledgements

I would first and foremost like to extend my sincere gratitude to Professor Chris Greenwell and Miss Tara Love, without whom this thesis would not have been possible. I would like to thank Chris, my supervisor, for his unending kindness and support in both academic and personal matters. He has seen me through two very difficult years of my life without once losing his patience, cheer, nor his good will towards me, even though my shortcomings have been numerous. He has offered me opportunities both within and outside of the university, going far beyond what is expected of a supervisor and showing sincere care towards those under his supervision, for which I am deeply grateful. Tara, although under no obligation, has helped me immensely throughout my project. She carried out both the indentation and CT experiments on my sandstone cores at Cambridge University. Furthermore, she taught me how to use Avizo software for CT analysis, as well as helping me interpret and conceptualise the data obtained during the course of this research. Beyond the scope of academia, she has provided both guidance and support in personal matters and I am glad to consider her a friend. I would also like to thank Catriona Sellick for teaching me how to use both the viscometer and filter press, as well as the useful discussion she has provided concerning different aspects of my project. Thanks must also go to Stephen Lishman for helping develop the press apparatus throughout its

many iterations. For their company and friendship during days in the lab, I would like to thank Hector Escamilla-Garcia and Oliver Wagstaff. I also thank Ian Chaplin and Leon Bowen for their help with attempting the SEM analysis. Last but not least, I would like to thank my family for their unwavering support through the good and the bad.

This work was severely impacted by COVID, delays in procuring samples, failed experiments, the lengthy development to obtain a working model of a novel piece of kit, and the unforeseen illness of a collaborative partner. Without the help of all the people mentioned above, helping me to navigate and circumvent these problems, this work would not have been possible to complete.

Table of Contents

1. Introduction

Drilling fluids (also known as drilling muds) are used to clear rock cuttings and provide hydrostatic pressure against the overlying seawater during oil and gas drilling operations. Their flow into wellbore rock is an unavoidable and, to an extent, a beneficial phenomenon in petroleum extraction. Drilling mud particulate build-up in pores at the surfaces of freshly exposed rock during overbalanced drilling (where the drilling fluid pressure exceeds pore pressure) will lead to the formation of a filter cake (a term used to denote the said particulate matter in and on the wellbore rock), which is desirable, provided it has the right thickness and porosity. In water-based muds (WBM, muds are denoted according to the primary or base fluid used in their manufacture) that use bentonite as the main viscosifier, the porosity and thickness of the filter cake is directly correlated with the percentage by weight (wt%) of bentonite (Vipulanandan and Mohammed, 2020). Formation of a thin, impermeable, and flexible filter cake reduces damage to the formation from permeating drilling fluid and fine particles and allows for near complete isolation of drilling muds from the rock unit pore fluids, preventing lost circulation. Another scenario in which fluid flow into the rock is useful, is its use as a medium to introduce lost circulation material (LCM) into the formation. LCMs are materials used to plug fractures and highly permeable formations through which lost circulation occurs, with bentonite also having found success in its use as such a material in its pelletised form (e.g., Miranda *et al.*, 2017). Lost circulation itself is the economically disadvantageous flow of drilling fluid into the formation, defined as a situation where less fluid is returned from the wellbore than is pumped into it (Lavrov, 2016). Drilling fluid loss gives rise to several problems, such as formation damage, reduced cuttings transport out of the well, and reduced fluid pressure (ibid). In well drilling operations, events of lost circulation are estimated to

cost USD 2 to 4 billion annually (Cook *et al.*, 2011). Research conducted in an effort to minimise these economic losses that have resulted from lost circulation, has provided valuable insights into the mechanisms behind reservoir rock-fluid interactions. Drilling mud invasion into reservoir rock has been extensively studied with the aim of minimising this lost circulation (e.g., Howard and Scott, 1951; Fuh *et al.*, 1992; Wang *et al.*, 2008). Some developments in understanding drilling mud invasion include: determining the rate and extent of invasion based on petrophysical properties of the reservoir (e.g., Donaldson and Chernoglazov, 1987 & Civan and Engler, 1994), effect of mud properties on invasion rate (e.g., Wu et al., 2005), and drilling mud effects on various rock properties, such as wetting and strength (e.g., Cuiec, 1989; Gamal, Elkatatny and Abdulraheem, 2020; Gamal *et al.*, 2020).

However, research carried out thus far on rock strength has focused on the effect that whole muds and mud filtrates have on the rock rather than individual constituents. The study at hand aims to analyse the effect that bentonite gels with a range of different rheologies (achieved using NaCl at various concentrations as an additive) have on rock strength, and attempting to qualitatively and semi-quantitatively assess these rock strength alteration mechanisms via scanning electron microscopy (SEM) and computer tomography (CT) analysis of the internal pore structures. In order to draw valid conclusions from strength testing (which in this study will be limited to quasi-static indentation to obtain stress-strain curves), an understanding is needed of the clay-gel structure and the clay-gel interactions with itself and with the rock components. The structure and properties of the rock itself, including what factors govern its cohesion, and how the gel may impact these properties must also be determined. Core samples used in this study are from the Berea sandstone formation, selected as a representative model for siliciclastic oil reservoirs that are commonplace in the North

Sea. Berea sandstone is primarily made up of quartz, followed by small amounts of feldspars and clays, and then some trace minerals (Kareem *et al.*, 2017). Berea sandstone has long been used in the petroleum industry as a standard material when undertaking research (e.g., Churcher *et al*., 1991; Øren and Bakke, 2003; Hannibal 2020). The reason for Berea's frequent use is due to its relative homogeneity, ease of availability, and extensive characterisation in the literature (Øren and Bakke, 2003), and hence why it was chosen for this study as well. While other standards, such as Indiana limestone and Baker dolomite, are also frequently used (Churcher *et al*., 1991), it was decided to limit the study at hand to one material type due to budget and time constraints.

As bentonite and sodium chloride play a major role in many WBMs, such as in the formation of the filter cake, as a lost circulation material, as well as making up a high percentage by mass of the drilling fluid that flows into formation during lost circulation events, it is imperative to understand the rock-fluid interactions between these constituents and the reservoir rock. This would allow for improved optimisation of drilling fluid composition and understanding of the effect that different gel rheologies have on rock fracture toughness, and initiation and propagation pressure during undesirable fracture formation in the rock unit.

1.1 Bentonite gels

1.1.1 Drilling fluids.

Pumped down through the drill string and returned to the drilling rig deck for cleaning and recirculation, drilling fluids/muds (classified as either petroleum oil based (OBM), synthetic oil based (SBM) or water based (WBM)) are shear thinning fluids (become

liquid like under applied stress, but gel like when resting), consisting of mixtures of chemical compounds and mineral additives. Drilling muds have the purpose of cooling and lubricating the drill bit, cleaning the hole bottom, carrying cuttings to the surface, and controlling formation pressures (Fink, 2015). Approximately 80% of all wells use water based drilling fluids, owing to their reduced logistical challenges (generally made at point of use) and improved environmental impact (Oilfield Market Report 2004). In water based drilling fluids, bentonite, a natural clay mineral consisting of mainly sodium montmorillonite, additives are used due to their rheological properties in aqueous solution and their subsequent ability to form a filter cake (Benna *et al.*, 2001). In solution, bentonites, which are highly colloidal, swell to form a thixotropic gel (Fink, 2015). Thixotropy is a beneficial property in drilling fluids due to their effective viscosity being low (allowing for them to flow easily) at high shear rates in the drill pipe, leading to reduction in pumping pressures, and effective viscosity being high at low shear rates (forming resilient gels) in the annulus, allowing for increased cutting carrying capacity (Caenn et al., 1988) when pumping ceases to extend the drill string. The desired rate of rapid shear thinning (low pressure required to transition from gel to liquid behaviour) thixotropy is achieved by adjusting the ratio of clay viscosifier to electrolytes and other additives, such as thickeners (e.g., carboxymethyl cellulose).

1.1.2 Bentonite clay

Bentonite is a naturally occurring clay, predominantly formed in marine environments from alteration of volcanic ash, with the majority of bentonite deposits formed during the Tertiary to Mesozoic period. Bentonite is made up primarily of the smectite clay group mineral montmorillonite alongside minor amounts of quartz, and feldspar. Clay

itself is defined as a naturally occurring material which is primarily composed of fine-grained minerals, it exhibits plasticity at appropriate water contents and will harden when dried or fired (The Clay Minerals Society, 2019). Clays are classed into groups based on composition and structure, with the primary groups being kaolin, smectite, illite, and chlorite. Smectites are phyllosilicates (compounds in which silicate tetrahedrons ($(SiO_4)^{-4}$) are arranged in a sheet by shared oxygen anions, known as a tetrahedral sheet) with 2:1 unit layers (an example provided in Figure 1). A 2:1 unit layer consists of two tetrahedral silica sheets sharing oxygen atoms with one octahedral sheet. An octahedral sheet, in turn, is composed of coordinating cations surrounded by either six bridging oxygens or oxygen atoms of hydroxyl groups. Clays can be classified as either dioctahedral or trioctahedral, indicating that each O or OH ion in the octahedral sheet is surrounded by two +3 ions (e.g., Al^{+3}) or three +2 ions (e.g., Mg^{2+}, Fe^{+2}) respectively. Montmorillonite is a dioctahedral smectite with the repeating unit formula $(Na,Ca)_{0.33}(Al,Mg)_2(Si_4O_{10})(OH)_2 \cdot nH_2O$ (illustrated in Figure 1). Unit layers are held together by van der Waals forces to form the crystal lattice of the clay for uncharged clay minerals, such as pyrophyllite, hydrogen bonding for 1:1 clay minerals such as kaolinite, and Coulombic interactions between layer units and interlayer cations for clay minerals with permanent layer charge (Luckham and Rossi, 1999). Van der Waals forces are weak electrostatic forces occurring due to fluctuating or rotating dipoles of atoms and molecules and their interactions with one another.

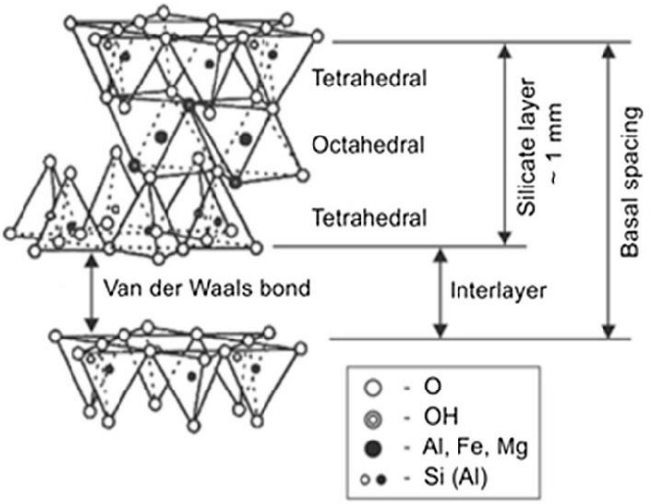

Figure 1. Montmorillonite layer structure **(**adapted from Cheraghian et al., 2014**)**

1.1.3 Isomorphic substitution and cation exchange

Isomorphic substitution is defined as the process of replacing one structural cation within the clay mineral layer unit for another of similar size (Barton, 2002). This substitution effect results in the gain of either a negative or positive charge within the clay minerals (with most clays exhibiting a net negative charge) (ibid). As an example, when Mg^{2+} sits within an Al^{3+} site in the octahedral sheet, or Al^{3+} sits in a Si^{4+} site in the tetrahedral sheet, the clay particle becomes negatively charged (M'Bodj *et al.*, 2004). As such, the extent to which isomorphic substitution occurs determines the net charge, and hence the cation exchange capacity (CEC) of the material. CEC is the measure of exchangeable cations a material can adsorb at a given pH, crystal size and cation type. Ion exchange reactions (between a material with a known CEC and a cation containing solution) are primarily determined by concentration of different ion species in each phase, as determined by the law of mass action. The cation charge and structural properties determine the material's selectivity for an ion. The selectivity exhibited between each ion of a certain element and the material, can be expressed as a selectivity coefficient. The selectivity sequence order for all clays is $Cs^{+} > Rb^{+} >$

$K^+ > Na^+ > Li^+$ (Gast, 1972). With the clay becoming more saturated with the preferred cation, there tends to be a decrease in the selectivity coefficient for that ion (ibid).

Montmorillonite has negative charges on its surface due to some Si^{+4} cations being replaced by Al^{+3} in tetrahedral sheets and some Al^{+3} cations being replaced by Mg^{+2} Interlayer cations in montmorillonites are either alkaline earth ions (Ca^{2+} and Mg^{2+}) or the alkali metal Na^+ (Luckham and Rossi, 1999). This allows for the classification of montmorillonites as either Ca-montmorillonite or Na-montmorillonite. Na-montmorillonite is the preferred additive in the petroleum industry due to its higher swelling capacity, ability to adsorb polymers in large amounts on its surfaces, and adequate gel-structure formation at low concentrations (Anderson *et al.*, 2010). Therefore, in the context of drilling fluids, bentonite is used to refer specifically to material which is predominantly Na-montmorillonite (Luckham and Rossi, 1999), which is the definition of bentonite used in this study henceforth.

1.1.4 Clay swelling

Bentonites, as well as other smectites, exhibit high rates of swelling (in comparison to most clays) in aqueous solution via water adsorption. This ability to swell is due to the clay's high surface area relative to the mass of the clay mineral grains (Velde, 1992). Studies have concluded that the primary mechanisms of clay swelling are crystalline and osmotic swelling (e.g. Alexiades and Jackson, 1965). Crystalline swelling occurs when layers of mono-molecular water line up, forming a quasi-crystalline structure between unit layers leading to an increase in basal spacing (also known as the d-value). This mechanism is carried out in a stepwise process, with the intercalaction of 0, 1, 2, and 3 planes of water molecules each representing a step (Mooney, Keenan and Wood, 1952). The increase in basal spacing is the function of the layer charge,

exchangeable cation size and charge, and polar surface groups of the clay mineral (van Olphen, 1964). It should also be noted that crystalline swelling does not occur homogeneously throughout all layers within a smectite sample, rather smectite layers exhibit contrasting hydration states within a sample during hydration (Ferrage *et al.*, 2005) .

Osmotic swelling occurs when the cations in the interlayer have a higher concentration than that of the cations in surrounding water, leading to water molecules being drawn into the interlayer in order to restore cation equilibrium (via the process of osmosis). Osmosis is the diffusion of a solvent through a semipermeable membrane into a region of higher solute concentration. Extent of osmotic swelling is dependent on specific surface area of clay, type of exchangeable cations, concentrations of ions and exchange capacity of the clay (Young, 1975). Osmotic swelling leads to a larger increase in the d-value than crystalline swelling, with basal spacing being roughly in the ranges of 20-130 Å and 9-22 Å respectively. Montmorillonites exhibit a basal spacing of 9.35 – 10.53 Å when dry (Teich-McGoldrick *et al.*, 2015). Na-montmorillonite exhibits significantly greater osmotic swelling than Ca-montmorillonite. This is due to clays containing sodium having stronger double-layer forces (discussed in 1.1.5) leading to greater swelling than in Ca-montmorillonite, which, conversely, exhibits limited swelling due to the strong ion-ion correlations acting within the divalent counterion systems (Segad *et al.*, 2012).

Within the petroleum industry, one of the primary drawbacks of using WBMs is the facilitation of clay swelling in clay minerals already present within the newly exposed rock formations and in the drilling mud itself. Clay swelling is problematic in drilling operations as it can lead to wellbore instability, hole closure, agglomeration of drilled cuttings, reduced hole cleaning efficiency, and reduced rate of penetration due to

balling of clay material at the drill bit (Anderson et al., 2010). Inhibition of swelling in WBMs is therefore an important consideration when determining which fluid additives to use in a wellbore. Common additives to reduce clay swelling include electrolytes, polymers, and surfactants. Electrolytes, the type of swelling inhibitors utilised in this study, reduce swelling by increasing coagulation in clay colloidal dispersions. It should be noted that some swelling within the drilling fluid is necessary to achieve the formation of a thixotropic gel, as previously mentioned.

1.1.5 Colloid stability and clay minerals

In aqueous solution, due to the high extent of osmotic swelling, Na-montmorillonite exhibits delamination of particles into individual layers or thin assemblies of a few layers, sometimes denoted “tactoids” (Lagaly and Jasmund, 1993). The incredibly small size (due to the aforementioned delamination) of the particles alongside repulsion of one another due to their electric potential, both of which are variables in DLVO theory, allows for a colloid state to be obtained at the right bentonite concentration (Odom, 1984). DLVO theory was originally proposed by Derjaguin and Landau in 1941 and Verwey and Overbeek in 1947. DLVO theory states that particle stability in colloidal solution is dependent upon an interplay of short-range van der Waals attractive forces and longer-range electrostatic repulsion forces (Evans and

Wennerström, 1999). The balance of these forces is given by a total potential energy function (also known as interaction energy). This relationship is expressed as:

$$W(h) = W_{vdW}(h) + W_{dl}(h) \qquad \textit{Eq. 1}$$

where $W(h)$ is the total potential energy function, $W_{vdW}(h)$ is van der Waals forces, and $W_{dl}(h)$ is electrical double layer forces. Van der Waals forces are attractive in colloidal solutions, whereas electrical double layer forces tend to be repulsive in scenarios dealing with the aggregation of identical particles (Trefalt and Borkovec, 2014), such as in this study. When attractive forces overcome repulsive forces, aggregation of the colloidal system occurs. Aggregation is the assemblage formation in a colloidal system leading to destabilisation. The double layer is a structure which appears on the surface of colloid particles in dispersed media. As discussed (refer to section 1.1.3), cation substitution in smectites (in the presence of aqueous electrolyte solutions) leads to a net negative charge. Due to this negative electric charge, the stern layer is formed (see Figure 2), where positive counter ions are attracted to the particle and are closely attached to it by electrostatic force (ibid). The outermost part of the double layer is termed the diffuse layer, which is a dispersion medium surrounding the particle, consisting of free ions (ibid) that are drawn to the particle by electric attraction and thermal motion. The interface which separates the diffuse layer from the mobile fluid of the colloidal solution is termed the slipping plane. The electrical potential at the slipping plane is termed zeta potential, as shown schematically in Figure 2.

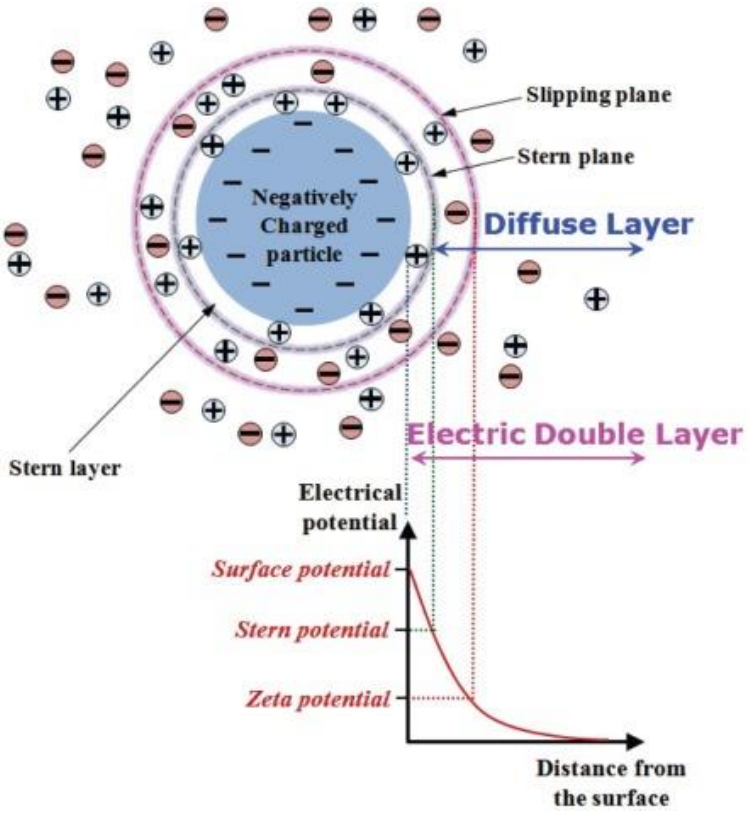

Figure 2. Electrical double layer. Taken from Park & Seo, 2011.

Experimentally determining (indirectly) zeta potential shows the magnitude of electrostatic repulsion and attraction between colloidal particles and thus is used as a parameter of colloid stability. Zeta potential can be calculated from experimental data from measurements of electrophoresis and electroacoustic phenomena. A zeta potential value that is not in the range of -30 mV to +30 mV generally has enough repulsive force to overcome van der Waals attractive forces, resulting in a stable colloidal system (Joseph and Singhvi, 2019).

1.1.6 Electrolytes in bentonite gels

The addition of cations (produced by electrolytes) to a clay colloidal dispersion reduces particle charge, thus reducing electrostatic repulsion leading to a reduction in zeta potential and subsequently resulting in a greater degree of coagulation and reduced

swelling (Swartzen-Allen and Matijevic, 1976). The effect of ion concentration on electric double layer radius can be explained mathematically via Debye length (which is itself a variable in $W_{dl}(h)$):

$$K^{-1} = \left(\frac{k_b\, T\epsilon_0\, \epsilon}{2q^2 N_A I}\right)^{1/2} \qquad \textit{Eq. 2}$$

Where K^{-1} is Debye length, q is elementary charge, N_A is Avogadro's number, I is ionic strength, T is absolute temperature, k_b is the Boltzmann constant, ϵ_0 is the permittivity of vacuum, and ϵ is the dielectric constant (Trefalt and Borkovec, 2014). Debye length can be directly related to the ionic strength of a solution as follows:

$$\frac{1}{K} = \frac{3}{ZC^{1/2}} \qquad \textit{Eq. 3}$$

Where Z is the valency of the ion and C is the ion concentration (Duman and Tunç, 2009). Ion adsorption onto clay particles occurs as a result of either electrostatic bonding or a chemical reaction involving covalent bonds (ibid). An increase in monovalent electrolyte concentration leads to a proportional decrease in zeta potential (Saka and Güler, 2006). At any given electrolyte concentration in a montmorillonite slurry, the addition of monovalent cations results in less negative zeta potential values than the addition of di- and tri-valent cations due to their greater valence, as explained by *Eq. 3* (Duman and Tunç, 2009). Therefore, altering the electrolyte type and concentration enables optimisation of a drilling fluid's electrokinetic and rheological properties. Conceptual illustration of the effect of electrolytes on the electrical double layer is shown in Figure 3.

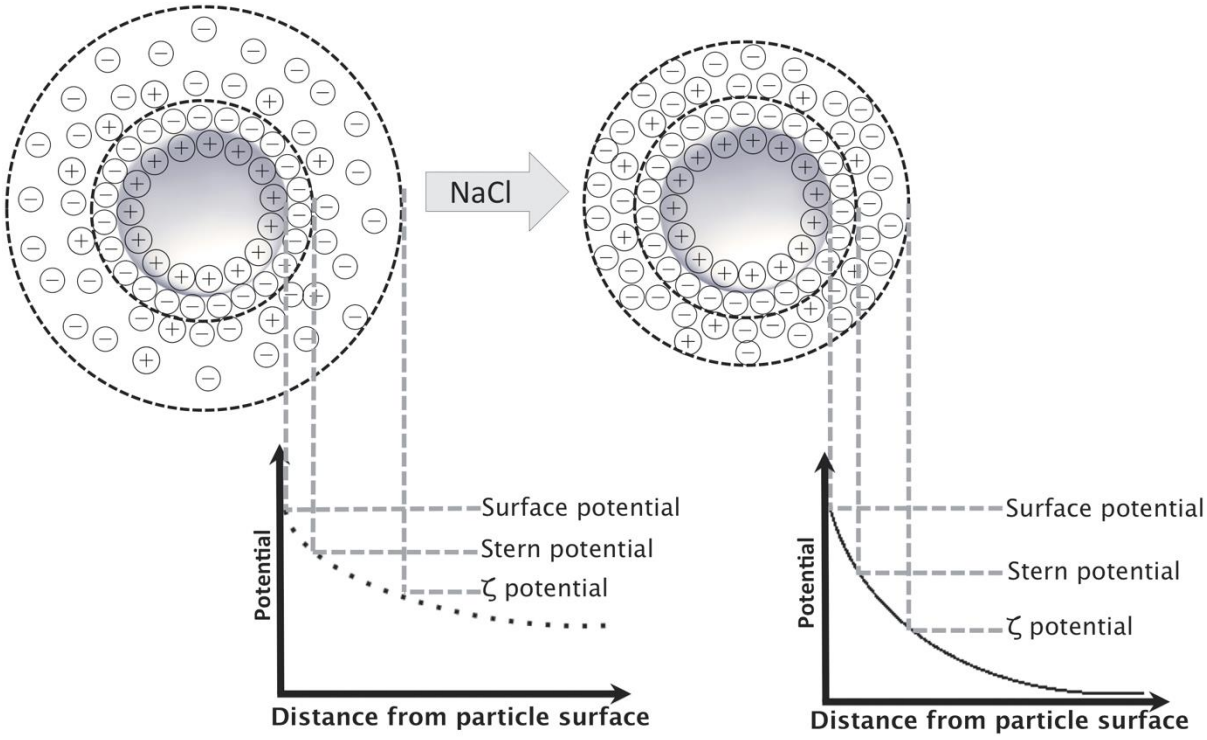

Figure 3. Electrolyte influence on zeta potential. Taken from Gossmann et al., 2015

1.2 Berea Sandstone

As previously mentioned, Berea sandstone has been adopted by the petroleum industry as a standard rock for core analysis purposes. Oil and gas developments in Berea sandstone have taken place since the 1800s (Parris and Nuttall, 2021), with thousands of wells having been drilled into and through the formation (Pepper *et al*., 1954). Due to its long history of usage in the oil and gas sector, research on Berea sandstone has been vast, with studies being carried out in fields such as wettability for enhanced oil recovery (e.g., Andrews *et al.,* 2020), effects of CO_2 injection on rock properties (e.g., Al-Yaseri *et al*., 2017), geomechanics (e.g., Baizhanov *et al*., 2019), and transport modelling (e.g., Labrecque and Blanford, 2021), to name but a few. The sandstone has also seen extensive usage as a dimension stone in the US, with quarrying having begun in the early 19th century (Hannibal, 2020).

The Berea Sandstone formation, found in the Appalachian Basin of the US, is of late Devonian age, and it is thought to be formed from alluvial deposits associated with prograding deltas during the Acadian orogeny (ibid). Berea sandstone consists of well-sorted and well-rounded sand grains, which range in size from 70-400 μm, with the bulk mineral composition being predominantly quartz, followed by smaller amounts of feldspar and clays, and then trace amounts of various other minerals (e.g., Churchel *et al*., 1991). These minerals form the framework grains, matrix and cements, which are the primary components of all sedimentary rocks. Framework grains are detrital fragments that make up the majority of a sedimentary rock. In sandstones, the framework grains commonly consist of quartz, feldspar and lithic grains. The matrix refers to fine-grained sediment that occurs between framework clasts. In Berea sandstone, the matrix is primarily composed of silt and clay sized particles. Cements are material that have been deposited in pore spaces via precipitation, or dissolution-re-precipitation, cementing together rock particles and fragments within the sandstone. The most common cements present are composed of quartz (amorphous silica and crystalline quartz), ankerite and siderite (carbonates), and clay cements (Kareem *et al.*, 2017). Clay minerals commonly present in Berea Sandstone are kaolinite, illite, smectite, and chlorite (e.g., Kareem et al., 2017). While these clay minerals are minor constituents of the bulk volume of Berea sandstone, Kareem et al., (2017) found that they were over-represented in pore spaces and at pore surfaces compared to other minerals (Figure 4), although the volumetric fraction of the different clay minerals varied considerably with permeability, demonstrating the heterogeneity present in the Berea sandstones.

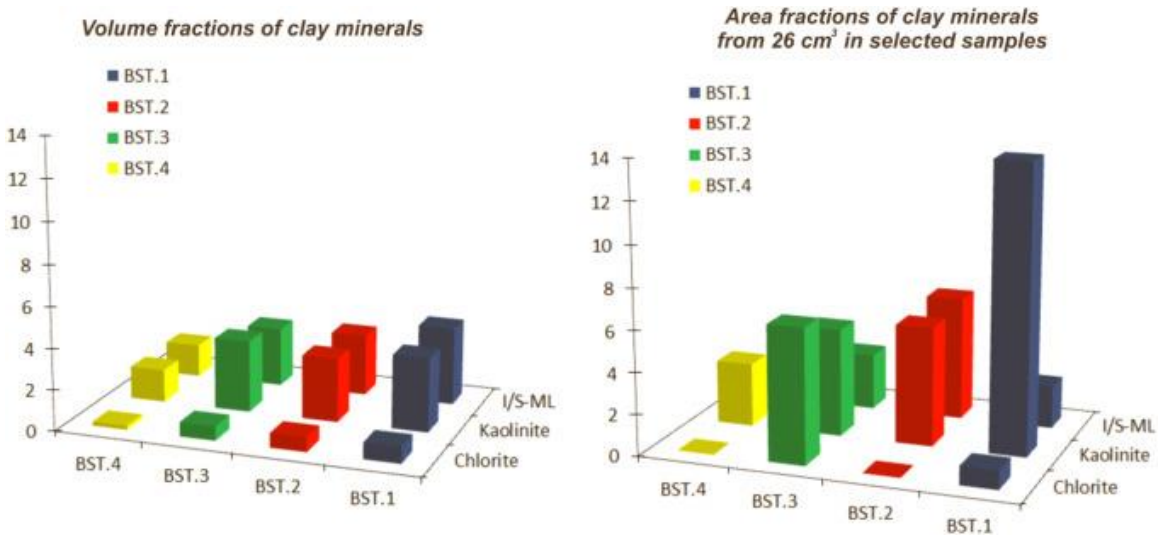

Figure 4. Bar chart illustration of the volume fractions and area fractions in % of the primary clay minerals present in Berea sandstone samples from XRD and EDX data. Taken from: Kareem et al., 2017

As clay minerals form the effective mineralogy at pore surfaces, rock-fluid interactions are likely to be dominated by reactions between these clays and gels. Clays in sandstone are either detrital or authigenic, meaning they are either particles from pre-existing rock that have deposited as sediment due to the result of erosion and weathering or are minerals formed within the depositional site as a result of geochemical processes, respectively. Both detrital and authigenic clays play an important role in determining the porosity, a major factor in reservoir quality, of sandstones. Fisher, Knipe and Worden, in 2000, showed that sandstones which contained either authigenic pore-lining clay or a large amount of detrital clay, had the smallest amount of authigenic quartz (quartz cement) in them. However, it should be noted that the effect that detrital clay minerals have on quartz cement is dependent on the amount of clay present, as, conversely, sandstones with small to medium amounts of detrital clay present, were shown to have the highest amount of authigenic quartz (ibid). The mechanism by which clay affects quartz cementation depends on the origin of the clay. Detrital clays, located at grain-contacts, at low to medium concentrations,

lead to greater quartz precipitation due to water-film diffusion pressure solution being promoted by the clay minerals (Dewers and Ortoleva, 1991). In sandstone with large amounts of detrital clay, quartz cementation is likely inhibited due to quartz grains being coated by the abundant clay, therefore not allowing for solution to take place, despite the ample presence of quartz-clay contacts (Fisher, Knipe and Worden, 2000). In the case of authigenic clay minerals, it has been observed that the clays form grain-coatings on quartz minerals which suppresses quartz cementation (Cecil and Heald, 1971), the mechanism behind this is attributed to the grain coating covering nucleation sites and therefore preventing authigenic quartz from nucleating (Pittman, 1972). As is the case with detrital clays, authigenic clay contents effect on porosity is seemingly also dependent on the amount and location of the clay. For example, both Oluwadebi, Taylor and Dowey, in 2018 and Bello *et al.*, in 2021 have shown that authigenic clay minerals can block pore throats and therefore occlude porosity. The study at hand may provide some insight into the mechanisms behind how authigenic clay is deposited in pore space (using the gel as an analogue). Alongside these larger scale mineral coverages, studies have shown that on the pore surfaces of sandstones, nanoparticles of differing materials, such as clay (e.g., Hassenkam *et al.*, 2011), organic coatings (Matthiesen *et al.*, 2014), iron oxides, quartz, and carbonate (e.g., Kareem *et al.*, 2017) are present on mineral surfaces.

1.3 Rock-fluid interactions

1.3.1 Rock-fluid interaction processes

Extensive literature exists for rock-fluid interactions, spanning an array of scientific fields such as diagenesis, petrology, contaminant transport, chemical weathering, and

rock mechanics (e.g., Steefel and Maher, 2009; Guéguen and Boutéca, 2004). Due to the wealth of research on the topic, it would be beyond the scope of this study to cover all known forms of rock-fluid interactions, but a brief overview on the subject has been attempted below. Note that, as previously stated, bentonite gels are not liquid, but rather a colloidal dispersion. They are, however, considered fluids (as are drilling muds), more specifically non-Newtonian fluids (e.g., Billingham and Ferguson, 1993), and as such, relevant to the section at hand.

The study of rock-fluid interactions began with standalone analyses of geochemical interactions under static conditions (Steefel and Maher, 2009). In the 1960s, the pioneering work of Helgeson, who developed the first geochemical reaction path models (Helgeson, 1968), allowed for analysis of multicomponent rock-fluid systems. Further advancements were made with the introduction of transport as a consideration (Lichtner, 1988), leading to the development of multi-component reactive transport models. As current reactive transport models represent our best understanding of the dynamic rock-fluid interactions taking place in the Earth's interior, they provide an excellent approach to summarise the topic at hand. Generalising modern reactive transport models, rock-fluid interactions can be considered to be roughly divided into four categories: geochemical reactions, transport, and mechanical deformation (which will be further discussed in Chapter 1.3.2). It should be noted that models vary in the processes that they consider, for example, the HPx model inputs include flow transport, biogeochemical reactions, as well as moisture, root uptake, porosity etc. (Schapel *et al.*, 2018). A coupled hydrological-mechanical-chemical (HMC) model, on the other hand, developed by Liu *et al.* (2006) allows for consideration of fracture mechanics within rock. Based on these studies, as well as others (e.g., Idiart *et al.*,

2020; Veveakis, Stefanou and Sulem, 2013), an overview of the major rock-fluid interactions can be compiled (Table 1).

Table 1. A generalised summary of rock-fluid interactions considered in reactive transport models.

Geochemical reactions	Transport	Mechanical deformation
Mineral dissolution and precipitation	Conduction	Stress and strain
Sorption	Advection	Compression and expansion
Ion exchange	Convection	Fracture formation and evolution
Acid-base reactions	Hydrodynamic dispersion	Swelling
Redox reactions	Colloid-facilitated transport	
Stable isotope fractionation	Molecular scale diffusion	

Out of the many listed forms of interaction, the ones specifically of interest in our static lab-based gel-rock system fall under the mechanical deformation category.

1.3.2 Mechanical properties

1.3.2.1 Fracture initiation, propagation, and toughness in wellbore rock under drilling conditions

Current understanding of linear elastic fracture mechanics, the sub-discipline of fracture mechanics most commonly applied for hydraulic fracture modelling (Wang *et al.,* 2014), is based on Griffith's Fracture Theory (Griffith, 1921). This theory states that failure occurs due to tensile stress that is induced at existing crack tips or joints, which are orientated at a critical angle to applied principle stresses (ibid). Fracture toughness, an addition to Griffith's theory made by Irwin in 1957, is the property of a material to resist fracture propagation. Fracture toughness, mathematically, is the critical stress intensity factor (K_c) of a sharp crack where crack propagation becomes rapid (ibid). The stress intensity factor (K) itself is defined as the magnitude of the

stress singularity, in a linear elastic material, at the tip of a mathematically sharp crack (Zehnder, 2013). K, in general terms, is expressed as:

$$K = f\left(\frac{a}{W}\right)\sigma\sqrt{\pi a} \qquad \textit{Eq. 4}$$

where $f(\frac{a}{W})$ is a geometry dependent function of the crack length a, W is the width of the specimen, and σ the applied stress (Soboyejo, 2002). This factor allows for the prediction of stress intensity near the tip of a crack caused by a residual stress or remote load. Irwin made another significant contribution to the understanding of fracture mechanincs in 1958, when it was recognised that rock failure did not only occur due to tensile failure, and Irwin subsequently classified failure patterns into three fracture modes (based on the direction of displacement of the fracture lips), where Mode I indicates the formation of a tensile fracture, Mode II is for shear fractures, and Mode III is torsion fractures. This classification is still in use today, a diagrammatical example has been provided in Figure 5.

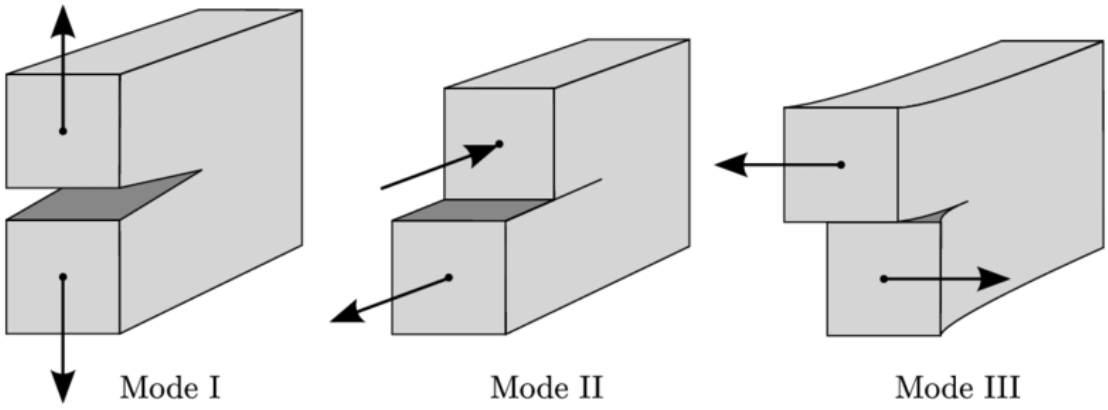

Figure 5. The three fundamental fracture modes proposed by Irwin. Taken from: Kammer, 2014

Based on understanding of fracture mechanics up to that point, Haimson and Fairhurst (1967) developed a criterion for the initiation of tensile hydraulic fracturing (hydraulic fracture initiation pressure or FIP) in an idealised wellbore (perfectly intact and cylindrical). This criterion can be expressed mathematically as follows:

$$p_i = 3\sigma_h - \sigma_H - p_p + T_0 \qquad \textit{Eq. 5}$$

Where p_i indicates fracture initiation pressure, minimum and maximum horizontal stresses are shown by σ_h and σ_H respectively, and lastly, T_0 is for the tensile strength of the rock. It should be noted however that Solberg, Lockner and Byerlee, in 1977, showed that hydraulic fracturing can in fact lead to the development of either shear or tensile fractures in the wellbore, dependent on the extent of differential stress, with shear fractures occurring in rocks with high pore pressures, such as in areas with high tectonic stresses (ibid). Whilst the study at hand has been restricted to North Sea relevance, an area which is considered to be tectonically stable (e.g., Ziegler, 1983), the permeation of gel into the rock may induce pore pressures similar to those within regions of tectonic activity. Fracture propagation pressure (FPP) is the pressure required to re-open and propagate the induced fracture at the initiation phase (Razavi *et al.*, 2017). FPP, for permeable rocks drilled with drilling fluid containing solids, is dictated by two energy dissipation mechanisms (ibid). The first of these mechanisms is related to the energy required for the creation of new surfaces in the rock, which is closely associated with the geometry of the growing fracture and rock fracture toughness (ibid). The second energy dissipation mechanism is related to the occurrence and extent of an uninvaded dry zone near the fracture-tip (ibid). Experimental investigations of this second mechanism (e.g., Morita, Black and Fuh,

1996) show that the build-up of solids near the fracture surface leads to low-permeability pressure barriers forming in the rock, leading to reduced fluid pressure being applied to the fracture tip. The amount and type of solids within this dry zone can be optimised by the addition of lost circulation materials (LCMs) to the drilling fluid (Razavi *et al.*, 2017). However, since the study at hand considers the fracturing of rock that is already gel-saturated (a poroelastic formation), the hydraulic fracturing problem is complicated by poromechanical effects of both the fracturing fluid (e.g., due to fluid invasion) and the already saturated rock, which will result in differing fracture behaviour in comparison to non-fluid permeated rock. For example, Sarris and Papanastasiou (2012) studied hydraulic fracturing within a cohesive, poroelastice, formation using finite element analysis. They found that higher pressures were required in order to fracture a poroelastic medium (containing an incompressible Newtonian viscous fluid) and that fractures formed within this medium are wider than those in a non-poroelastic formation.

1.3.2.2 Fracture initiation, propagation, and toughness in relation to other rock mechanical properties

While Section 1.3.2.1 introduced the concept of FIP, FPP, and fracture toughness in the context of hydraulic fracturing within wellbores during drilling, a more fundamental relationship between these properties and those that are more conventionally determined under laboratory conditions (e.g., stress strain curves from which mechanical properties such as ultimate strength, Young's modulus, and yield strength can be deduced) will now be explored. It should be noted that while Mode I and II fractures that occur in hydraulic fracturing are classed as tensile and shear,

respectively, both of these fracture modes can be initiated by the use of a compressive force on the rock material (Zhang *et al.*, 2022). As such, a compressive test could be considered a suitable analogue to explore these fracture modes in a laboratory experiment, such as in the case of this study. Fracture evolution under a compressive force in relation to a stress-strain curve are provided in Figure 6, with Figure 7 showing the fracture modes taking place.

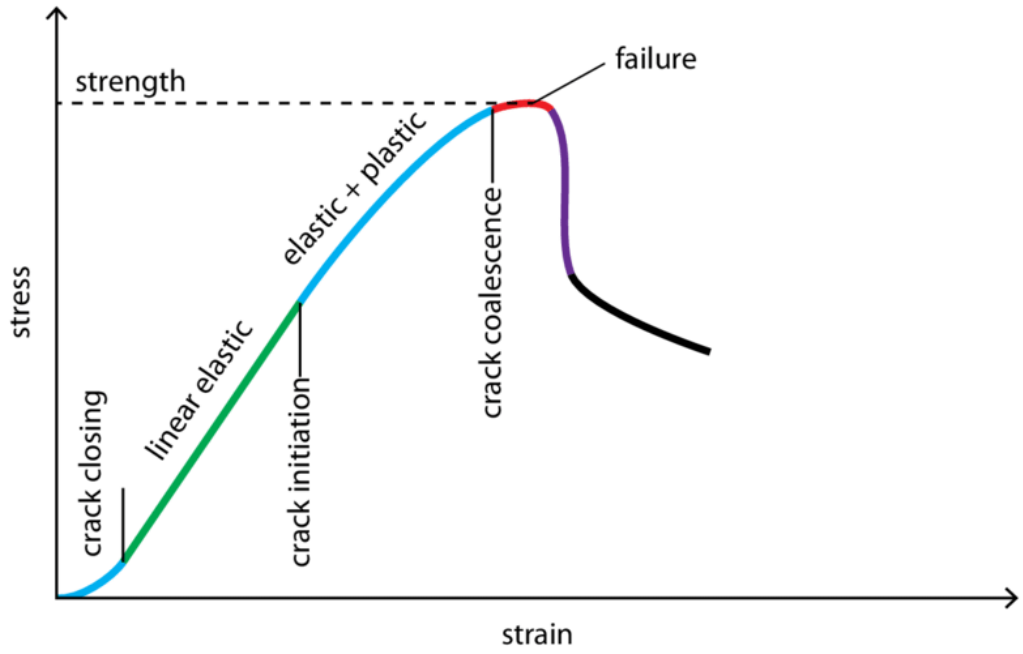

Figure 6. Typical fracture evolution corresponding to stages of a stress-strain curve under a compressive force. Source: Stöckhert, 2015

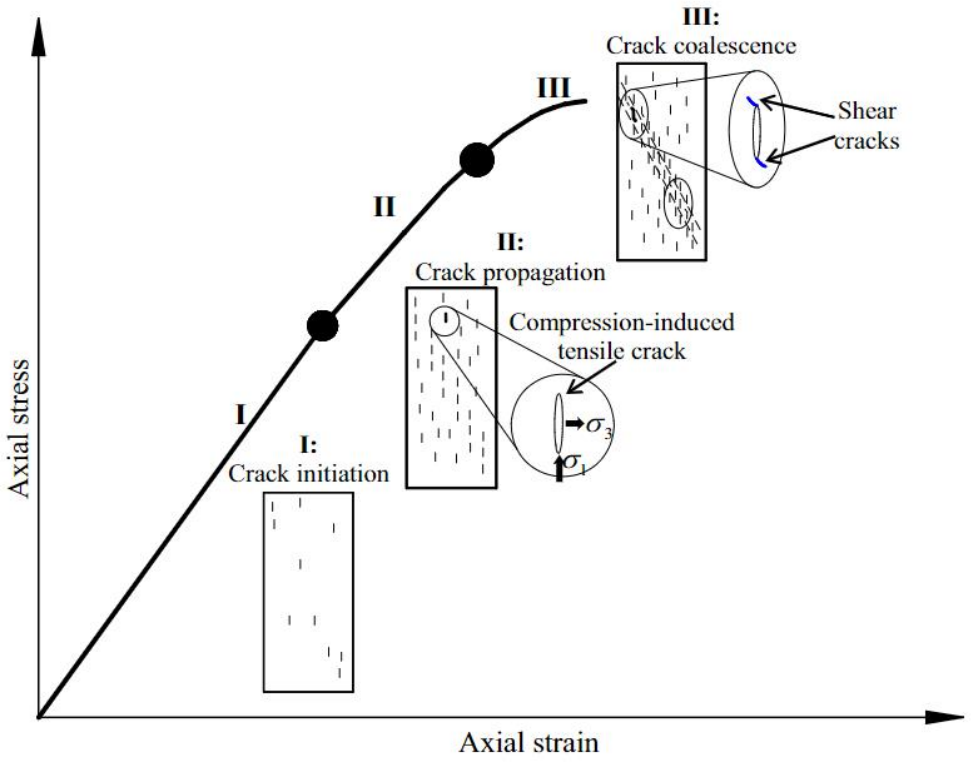

Figure 7. Typical fracture evolution under a compressive force with fracture modes. Source: Xu et al., 2018

As seen from Figure 6, fracture (or crack) initiation begins at the end of the linear or elastic region of the stress-strain curve (the slope of which gives the relative stiffness or the Young's modulus of the material). Young's modulus is mathematically defined as:

$$E = \frac{\sigma}{\varepsilon} \qquad \textit{Eq. 6}$$

where σ is the stress of the linear region and ε is the strain of the linear region. Yield strength is the end point of the elastic region, at which point the material starts to deform in a plastic manner. Once crack initiation has occurred, stable fracturing will follow until a point at which ~70-90% of the ultimate strength is reached (Hoek and Martin, 2014), with ultimate strength simply being the highest stress value a material can sustain. After this point, unstable crack growth will start to take place until the

ultimate strength is reached. Upon reaching ultimate strength, crack coalescence (the merging of fractures) will take place, which will generally result in sample failure (ibid). Note that even though the sample has been termed as 'failed', the post-peak region will define the manner in which the sample failure occurs and how long this failure takes place.

As fluid inclusion within rock alters FIP and FPP (as mentioned in Section 1.3.2.1), it also alters the more fundamental mechanical properties that these pressures are dependent upon. A large body of literature has shown that compressive strength under uniaxial loading, when a rock is water saturated, reduces by up to 90% (a review on the subject is given by Li and Wang, 2019). Similarly, Young's modulus has also been reported to decrease with water inclusion (ibid). Water has also been found to change the stress-strain behaviour of rock from a brittle to a more plastic manner (Lu *et al.*, 2021). Very little work, however, has been done on non-Newtonian fluids and their effect on rock mechanical properties bar those studies concerning the petroleum industry (e.g., drilling muds and their constituents), these as well as the effects of these fluids on other physico-chemical properties, will be discussed in more detail in the following section.

1.3.3 Literature concerning rock-fluid interactions within the petroleum industry

Specifically concerning the field of petroleum geology, for sandstones, research has been done on rock-fluid interactions in the following contexts: enhanced oil recovery (EOR) (e.g., Hamouda and Valderhaug, 2014), alteration of rock properties by whole drilling fluids (e.g., Cuiec, 1989; Sharma and Wunderlich, 1987; Yadav et al., 2016; Gamal *et al.*, 2020) and by various drilling fluid constituents (Sharma and Wunderlich,

1987; Wuyep et al., 2020; Gamal, Elkatatny and Abdulraheem, 2020), effects of crude oil and its constituents on rock properties (e.g., Clementz, 1976), and reinjection of geothermal wastewater (Safari-Zanjania, Whitea and Hanorb, 2013). Studies using drilling fluid constituents (e.g., Koteeswaran et al., 2018) and whole drilling fluids (e.g., Mody and Hale, 1993 & Lal, 1999) also exist for shales. No studies, however, have been conducted to specifically analyse interactions between bentonite gels with sandstone, or any other reservoir rock, in any capacity. Available works most relevant to the study at hand are therefore those that utilise water-based drilling fluids containing bentonite to observe rock-fluid interactions, and these are discussed more in-depth.

In 1987, Sharma and Wunderlich analysed the effect that drilling fluids and certain individual mud constituents had on wettability and permeability by evaluating capillary pressure behaviour and contact angle measurements. They observed that drilling fluids with no bentonite constituents showed larger effects on permeability and wettability than those that included bentonite. The authors speculated that drilling fluids that lacked bentonite and thus formed poor filter cakes lead to greater alteration in rock properties as other drilling fluid components came into contact with the rock to a greater extent. Yadav and others (2016) analysed the effect of four different drilling fluids on rock mechanical properties. It was found that for both water- and oil-based muds, the effect of fluids on Young's moduli and peak strength of Berea sandstone was negligible. In 2018, Koteeswaran and others assessed rock-fluid interactions between shales and bentonite gels, tetramethylammonium chloride, and polymers, using qualitative parameters (via scanning electron microscopy). They found that rock-fluid interactions between shale and bentonite slurries led to adsorption of salts (KCl and NaCl) on the shale pore surfaces. Additionally, Koteeswaran et al., (2018)

demonstrated that a solution consisting of bentonite, NaCl, and anionic polyacrylamide lead to the formation of a uniform membrane over the shale surface, resulting in water not being able to enter or leave the shale. This membrane formation, however, is limited to shales and other low permeability (tight) materials with negative surface charge (e.g. clay). Due to low permeability being the result of fine pore size, this in turn allows for selectively restricting the flow of some ions while allowing others (Osuji, Chenevert and Sharma, 2008). Gamal et al., 2020 observed the effect that a barite-weighted WBM, which contained bentonite as a viscosifier, had on Berea sandstone core mechanical properties (including unconfined compressive strength (UCS), tensile strength, Poisson's ratio, and Young's modulus) as a function of exposure time. The authors noted a reduction in the tensile and compressive strength of the rock over five days of exposure to the WBM, and an increase in dynamic elastic moduli over the same time frame. These results directly contrast those by Yadav and others in 2016. This discrepancy could be partially explained by the use of polyamine by Yadav et al., instead of KCl as a swelling inhibitor, nevertheless the results by Gamal et al., serve to highlight the long interaction time between drilling fluid constituents and Berea sandstone, adding an additional consideration to the work at hand.

1.4 Filter cake formation

During overbalanced drilling, two forms of filtration occur in an oil well: static filtration and dynamic filtration. Static filtration occurs when mud is not being circulated, and under such conditions the filter cake exhibits linear growth (ignoring initial spurt loss) (Caenn, Darley and Gray, 2016). Conversely, dynamic filtration takes place during circulation, and filter cake size is limited by erosive action of the mud stream (ibid). For

dynamic filtration, growth is rapid initially and decreases until dynamic equilibrium is reached. For both static (*Eq. 7* and *Eq. 8)* and dynamic filtration (*Eq. 9*), the rate of filter cake growth and the functions governing said growth can be expressed mathematically.

$$Q_w^2 = \frac{2kPA^2}{\mu} \times \frac{Q_w}{Q_c} t \qquad \textit{Eq. 7}$$

Equation 4 (ibid) governs filtration under static conditions, where Q_w is the volume of the filtrate, Q_c is the volume of the cake, k is permeability in Darcies, P is differential pressure in atmospheres, μ is viscosity of the filtrate in centipoises, and t is time in seconds. Equation 7 can be simplified as follows:

$$Qw = \frac{2kPA^2t}{\mu Qc} \qquad \textit{Eq. 8}$$

Dynamic filtration rate under equilibrium conditions is given by equation 9 (Outmans, 1963):

$$Q = \frac{k_1 \left(\frac{\tau}{f}\right)^{-v+1}}{\mu\delta(-v+1)} \qquad \textit{Eq. 9}$$

where Q is the filtration rate, k is permeability at 1 psi pressure, δ is the mud stream's exerted shear stress, f is the internal friction coefficient of the cake's surface layer, $(-v+1)$ is the cake compressibility function, and τ is the hydrodynamic shear stress.

Bentonite and electrolytes affect the permeability function of both static and dynamic filtering of WBMs. Particle size, shape, and the effects of flocculation and aggregation have a significant impact on cake permeability (Caenn, Darley and Gray, 2016). Gates and Bowie in 1942 and Krumbein and Monk in 1943 established a clear correlation between cake permeability and particle size. As previously discussed, bentonite in solvent forms a colloidal dispersion, due to the small particle size and insoluble nature of colloids, the permeability of the filter cake depends almost entirely on properties and proportions of the colloidal fraction (Caenn, Darley and Gray, 2016). Flocculation, much like aggregation (discussed in Section 1.1.5), is a process of a colloidal dispersion becoming more unstable. In colloid chemistry, aggregation and flocculation are used synonymously, however in drilling fluid technology, flocculation refers to loose association of clay platelets that form flocs, whereas aggregation means formation of aggregates made up of parallel platelets spaced < 20 Å apart (Mering, 1946). With an increase in the degree of flocculation and aggregation, there is an increase in interparticle attractive forces, and subsequently larger particle sizes, leading to an increase in cake permeability and porosity as the particles cannot enter the pores. It is therefore important to strike a balance between controlling clay swelling and maintaining a small enough particle size to form an impermeable filter cake.

Successful filter cake formation can be generalised to occur in three steps (illustrated in Figure 8). Initially a mud spurt takes place, this is the process of fine mud particles passing into the formation unhindered as they are too small to be trapped by the formation and an internal filter cake has yet to form. The internal filter cake formation is termed ‘the bridging’. Critical sized particles are able to stick at flow channel bottlenecks and form a bridge inside the surface pores (Caenn et al., 2016). This internal filter cake is of particular interest in the study at hand, as the bentonite gel

within the core could be viewed as such an internal material within a wellbore context. Lastly, after a bridge has formed, smaller and smaller particles are able to be trapped, leading to the formation of an external filter cake

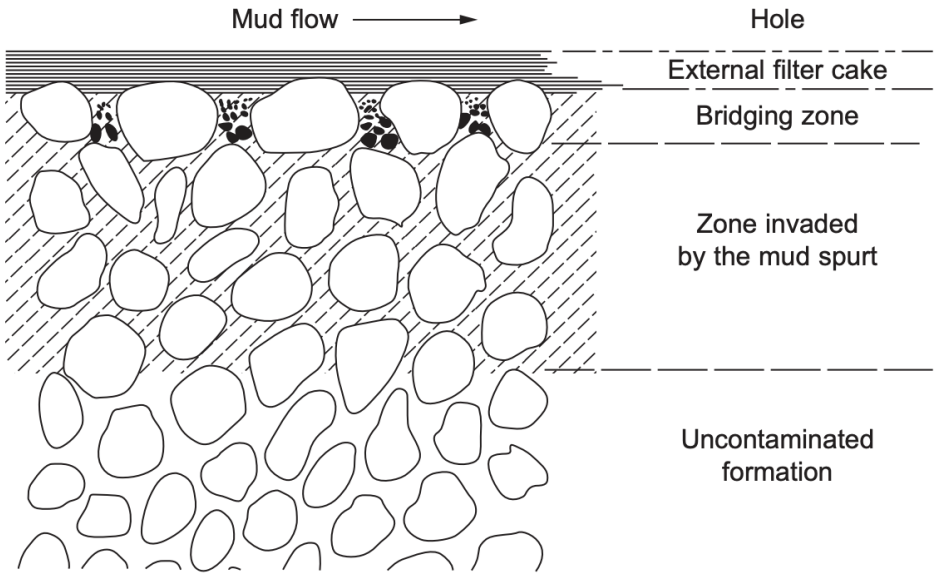

Figure 8. Filter cake formation by mud particle invasion. Taken from Caenn et al., 2016

In a laboratory setting, the successfulness of a filter cake can be determined experimentally. In 1998, Bailey et al. created a method to determine the yield stress of filter cakes by measuring shear failure via a hole-punch method. Yield stress can be related to the shear failure measurements via the following equation:

$$F_{fail} = 2\pi r h \tau_y \qquad \textit{Eq. 10}$$

Where F_{fail} is the peak force measured as the cake yields under the hole-punch, r is the radius of the punch cylinder, h is the filter cake thickness, and τ_y is the yield stress (ibid). External filter cakes were formed from bentonite dispersions of differing salt concentrations using a fluid loss cell in the study at hand. Filter cake properties were measured in this study to provide a reference point to fluids tested in literature.

1.5 Lost circulation and wellbore strengthening

The majority of drilling fluid losses in lost circulation scenarios are through hydraulic-driven fractures, the mechanics of which have been explained in the preceding chapter. Excessive hydraulic pressure is most likely to occur in formations with a narrow mud weight window. A mud weight window is simply the safe density range a drilling mud can possess. When this value is exceeded, tensile failure will occur in the wellbore, conversely if the lower limit is reached, shear failure will occur. Scenarios where a narrow mud weight window is present, are depleted zones, deep-water formations, deviated wellbores, and naturally fractured formations (Feng, Jones and Gray, 2016). The use of bentonite muds has been shown to lead to considerable amounts of lost circulation compared to other mud types (Nasiri *et al.*, 2017). The disparity between the loss of bentonite mud compared to other mud types could potentially be explained by excessive flocculation and aggregation of the clay particles (as explained in Section 1.4), however no research has been conducted to explain the causality.

Wellbore strengthening is the process of increasing FIP and FPP and subsequently increasing the mud weight window. Wellbore strengthening (WBS) is believed to work, in the case of FPP, by the build-up of solids near fracture surfaces using LCMs, leading to low permeability pressure barriers (Razavi *et al.*, 2017). WBS methods that utilise LCMs can broadly be categorised as either preventative or remedial. Preventative treatment intends to strengthen the wellbore and prevent fracture formation and

extension of pre-existing fractures prior to the lost circulation event (Feng and Gray, 2017). Remedial treatment, as the name implies, uses LCMs after substantial loss has already occurred (ibid). Extensive research has been conducted on various materials to determine their suitability for use as LCMs (e.g., Cargnel and Luzardo, 1999; Pilehvari and Nyshadham, 2002; Whitfill and Hemphill, 2003), including bentonite (e.g., Englehardt, Wilson and Woody, 2001; Miranda et al., 2017). In 2017, Miranda and others demonstrated pelletized bentonite as a highly successful LCM to remediate severe circulation loss under laboratory conditions. As an LCM, bentonite is pressed into pellets as the addition of powdered bentonite has been shown to hydrate prematurely, i.e., prior to reaching the desired depth (Englehardt, Wilson and Woody, 2001). However, no studies have evaluated the effect that invaded bentonite (whether the invasion be via lost circulation or the addition of LCMs) has on FIP and FPP of the rock

1.6 Aim of the study

The objective of the research is to gain an understanding of the effect that a clay gel permeating the pore space has on sandstone rock fracture properties. The study at hand aims to conduct qualitative and semi-quantitative analysis via imaging and elemental analysis of pore spaces to assess rock-fluid interactions between Berea sandstone and bentonite gels, and then attempt to attribute changes in fracture behaviour to these pore-scale analyses. Fracture toughness of the rock (pre- and post-flooding) will be determined to see changes in material toughness as a result of rock-fluid interactions.

The specific objectives of the study are as follows:

- To prepare a stable bentonite gel that may be used to permeate the Berea sandstone cores.
- To design a novel apparatus to push the bentonite gel into the sandstone matrix.
- To understand the potential mechanism behind the way that the permeated clay gel can lead to a reduction in fracture initiation and propagation pressure.
- To understand the impact of the salinity strength and subsequent composition of the gel on the resultant clay gel permeated sandstone mechanical properties.
- To provide insight into the mechanisms behind how authigenic clay is deposited in pore space (using the gel permeation as an analogue).

This study will observe whether the effect on mechanical properties of permeating bentonite gel into rock is a function of changes in pore pressure, porosity, permeability, interaction effects, or a combination of these factors. If interaction effects are present (e.g., chemical interactions), the study will analyse them and attempt to quantify how salt and clay constituents affect interactions in pore spaces.

The results of this study will provide insight into rock-fluid interaction mechanisms, allow for optimisation of a variety of industry processes, as well as provide a potential analogue for clay migration during diagenesis. Potential industry applications of the study include optimization of drilling fluid bentonite and NaCl content for: wellbore strengthening for enhanced oil recovery applications, improving material strength for civil engineering uses, and reconsolidation of weak slope systems.

2. Materials and methodology

2.1 Materials

Four sets of Berea sandstone core samples with 4 different permeability ranges: <75 mD, 75–175 mD. 175–300 mD, and >500 mD were acquired form Cleveland Quarries, Ohio, U.S. For every permeability range, 20 core samples were obtained, with each core sample measuring 6.35 mm in thickness and 63.5 mm in diameter. A generalised chemical composition for Berea sandstone was provided by the supplier (table 2).

Table 2. Berea sandstone composition. Source: Cleveland Quarries

Compound	Chemical formula	% Composition
Silica	SiO2	93.13%
Alumina	AI2O3	3.86%
Ferric Oxide	Fe2O3	0.11%
Ferrous Oxide	FeO	0.54%
Magnesium Oxide	MgO	0.25%
Calcium Oxide	CaO	0.10%

The bentonite used for gel preparation was a natural sodium bentonite with the brand name Berkbent GS, provided by TOLSA Group (representative chemical and mineralogical composition provided in Table 3. And Table 4. Respectively). The electrolyte additive used was NaCl (≥99%), provided by Sigma-Aldrich.

Table 3. Chemical analysis of Berkbent GS, values provided are for a representative sample of the material. Source: TOLSA Group

Chemical composition	Typical Chemical analysis (%)
SiO_2	61.16
Al_2O_3	19.29
MgO	3.05
Fe_2O_3	4.47
Na_2O	2.91
CaO	1.40
K_2O	<0.44
TiO_2	<0.33
Mn_2O_3	<0.05
Loss on ignition	6.02

Table 4. Mineralogical analysis of Berkbent GS, values provided are for a representative sample of the material. Source: TOLSA Group

Mineral group	Typical Mineralogy (%)
Montmorillonite	96
Feldspars	1
Gypsum	2
Quartz	1

2.2 Gel sample preparation

Four types of gel were prepared with four different NaCl concentrations (1.46% (wt/vol), 1.75% (wt/vol), 2.05% (wt/vol), and 2.34% (wt/vol)). The bentonite concentration was kept at a constant 20% (wt/vol) for each gel sample, and the rest of the gel composition was made up of deionized water. The chosen, final, ionic and bentonite concentrations were determined experimentally by preparing gels of different NaCl concentrations until a satisfactory range of relative viscosities was achieved. A range of 0.1M to 2M NaCl solutions was initially tested, corresponding to a wt/vol range of 0.58% to 11.68%. This concentration range was narrowed down until a range of gels were made that were qualitatively (visually) assessed to have a high enough fluidity to be permeated into a core sample without fracturing the sandstone, but not have a viscosity so low that the gel to behaves like a liquid.

The samples were originally prepared in centrifuge tubes and left to gelate over a roughly 24-hour period at room temperature. Despite testing a variety of different salt concentrations, this approach did not yield much success in creating a homogeneous gel (Figure 9).

Figure 9. Attempted Bentonite clay gelation, without agitation, in different strength NaCl solutions.

This was due to the lack of agitation during the gel preparation, which turned out to be a necessary part of the process, as high shear is required to assure that all bentonite particles are wetted, so that no clumping is able to occur (Federation of Piling Specialists, 2006). Mechanical blending using a NutriBullet blender (600 W) for 20 seconds was then introduced to the gel preparation process with positive results in achieving a gel structure (Figure 10).

Figure 10. Gels prepared using a blender to induce agitation.

Once the desired range of salt concentrations were determined, larger batches of the selected gels were prepared for quantitative viscosity measurements and permeation.

2.3 Rheology and fluid loss tests

Viscosity and gel strength tests were undertaken using a Fann Model 35 viscometer. Gel strength was measured after a 10 second and 10 minute wait time following the

American Petroleum Institute (API) standard (API RP 13B-1, 2009). Apparent viscosity (η), plastic viscosity (μ_p), and yield point (σy) were calculated following the same standard (ibid), wherein apparent viscosity is defined as:

$$\eta = \frac{\tau}{\dot{\gamma}} \qquad \textit{Eq. 11}$$

where τ is shear stress and $\dot{\gamma}$ is the shear rate. Next, plastic viscosity is defined as:

$$\mu_p = \theta_{600} - \theta_{300} \qquad \textit{Eq. 12}$$

where θ_{600} corresponds to the 600-rpm shear stress and θ_{300} is the 300-rpm shear stress. Lastly, yield point:

$$\sigma y = \theta_{300} - \mu_p \qquad \textit{Eq. 13}$$

Where θ_{300} is the 300-rpm shear stress and μ_p is the plastic viscosity.

An OFITE high temperature high pressure (HTHP) double capped filter press (175 mL), fitted with 175-300 mD cores instead of filter papers, was used to determine rheological data such as filtrate volume, filter cake thickness, and filtrate flow rate of the gels. From this data, permeability of the filter cakes formed by gels was also able to be calculated (*Eq. 15*) using a modified Darcy's equation (*Eq. 14*).

$$q = \frac{KA\Delta P}{\mu h} \qquad \textit{Eq. 14}$$

Where q is the filtrate flow rate (cm^3/sec), K is the permeability (darcies), A the cross section area in cm^2, ΔP being the pressure differential (atmospheres), μ denoting viscosity (cP), and h is the thickness of the filter cake in cm (MI Swaco, 2001).

Rearrangement of this equation to give K is:

$$K = \frac{h\mu q}{\Delta P A} \qquad \textit{Eq. 15}$$

which provides the permeability of the filter cake.

2.4 Gel permeation cell

The prepared gels were pushed into the core samples using a novel apparatus (the working iteration of which is shown in Figure 11, and a schematic is provided in Figure 12) designed for the study at hand.

Figure 11. Cylindrical press apparatus used to permeate the gel into sandstone cores.

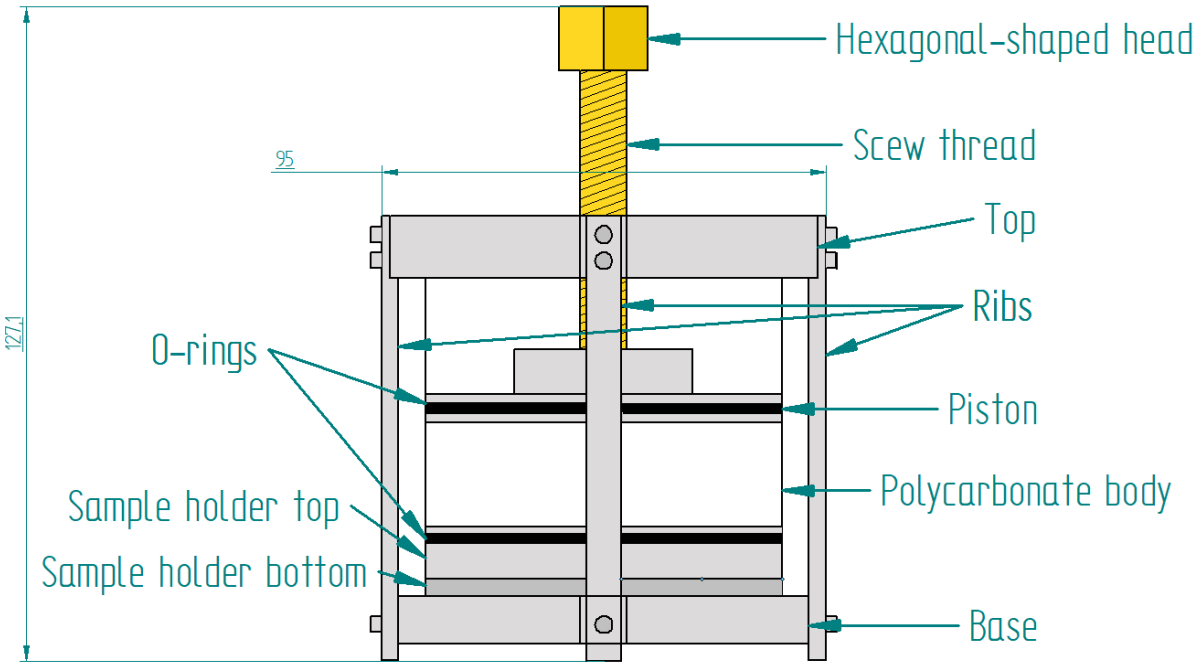

Figure 12. A labelled schematic of the final, working, iteration of the apparatus. Height and diameter measurements are in millimetres.

The cell consists of a stainless-steel chassis which surrounds a cylindrical polycarbonate body, it measures 127.1 mm in height and 95 mm in diameter.

2.4.1 Gel permeation experiments

The apparatus uses torque to generate compressive force, applying pressure to the gel and forcing it into the core. Torque, and subsequently fluid pressure, was increased and measured inside the apparatus via a mechanical dial torque wrench. Torque was incrementally applied until the press had made contact with the top of the sample container (as demonstrated in in Figure 13), at which point the permeation process was considered finished. Upon completion, the filter cake which had formed during the permeation process (an example in Figure 14) was removed. This was done in order to analyse the effect that only the gel, which had permeated the core, had on rock mechanical properties.

Figure 13. Press making contact with the sample holder.

Figure 14. Example of a filter cake formed during permeation of a bentonite gel with the use of the novel apparatus.

An arbitrarily selected one-minute period was given between each application of torque in order to reduce the pressure difference between the container and the exterior by allowing time for fluid to escape through the core. This was done to reduce the likelihood of hydraulically fracturing the samples due to internal pressure. Torque was increased with each successive application, up to a maximum of 5 N m^{-1}, between each increase of 1 N m^{-1} in torque, the core sample was checked for fracturing. If fracturing had occurred, the torque value was noted and the said value was not allowed to be reached again in the repeat of the trial.

Three batches of gel permeated cores were prepared for three sets of analyses. Each batch was intended to have four cores in every permeability range, with each of the four cores being impregnated with one of the four different bentonite gels, providing a sample of each permeability range saturated in each gel. The first batch (I), after permeation, was wrapped in Parafilm and kept at standard temperature and pressure (STP), resulting in the gel drying. The second (II) and third batch (III), also sealed in parafilm, were stored at a temperature of 4°C. However, due to the limited number of samples, issues of fracturing during permeation (discussed further in chapter X), and difficulties sourcing more cores from the provider in time, Batches I and II were incomplete (Tables 5 and 6), whilst Batch III had a full set of cores.

Table 5. Batch I inventory and dates of permeation. X denotes a missing sample in the batch.

Permeability (mD)	Gel			
	2.34% (wt/vol) NaCl gel	2.05% (wt/vol) NaCl gel	1.75% (wt/vol) NaCl gel	1.46% (wt/vol) NaCl gel
>500	28/09/2021	X	X	X
175-300	X	06/10/2021	12/10/2021	X
75-175	01/10/2021	10/10/2021	13/10/2021	X
<75	01/10/2021	10/10/2021	13/10/2021	X

Table 6. Batch II inventory and dates of permeation. X denotes a missing sample in the batch.

Permeability (mD)	Gel			
	2.34% (wt/vol) NaCl gel	2.05% (wt/vol) NaCl gel	1.75% (wt/vol) NaCl gel	1.46% (wt/vol) NaCl gel
>500	X	X	X	X
175-300	23/10/2021	24/10/2021	25/10/2021	X
75-175	23/10/2021	25/10/2021	25/10/2021	22/10/2021
<75	24/10/2021	25/10/2021	25/10/2021	20/10/2021

Batch I (Table 5) was made for indentation analysis of sandstone cores containing gel that had dried out (to observe how aging alters mechanical properties). Similarly, the second batch (Table 6) was also prepared for mechanical analysis but containing a wet gel that had not been allowed to dry out. It should be noted that a control batch (or Batch 0), in which cores were not permeated with gel, was also included in the indentation experiments (consisting of three <75 mD cores, two 75-175 mD cores, and three 175-300 mD cores). The last batch (III) was intended for SEM analysis but was never used (discussed further in Section 3.2.1).

2.4.2 Development of the cell

The original and subsequent designs of the cell were developed by the author, Prof. Chris Greenwell, and Mr Stephen Lishman, with the design process being done in Autodesk Inventor Professional 2021. The physical production and modification of the cell was done at the Physics Department workshop, University of Durham. Altogether, the apparatus underwent four iterations (Figure 15) in its development before a final, working, design (mark IV) was settled upon.

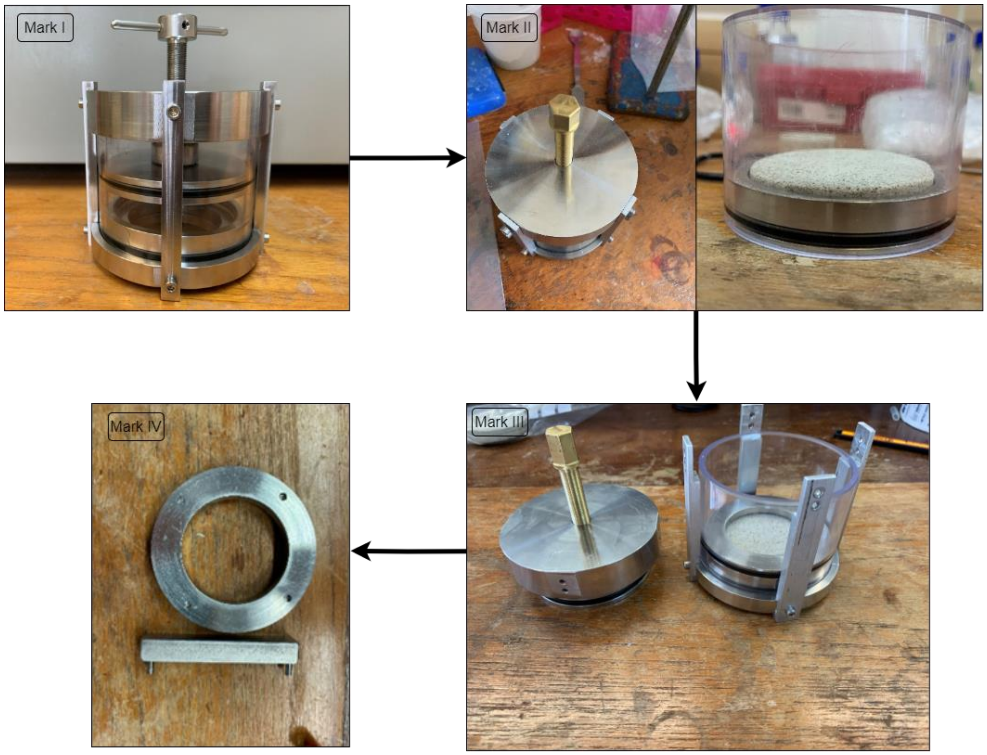

Figure 15. Changes in the design of the novel press apparatus throughout its development cycle.

The initial prototype, Mark I, a schematic of which is shown in Figure 16, was rejected and redesigned due to the inability to measure the force being applied to the gel

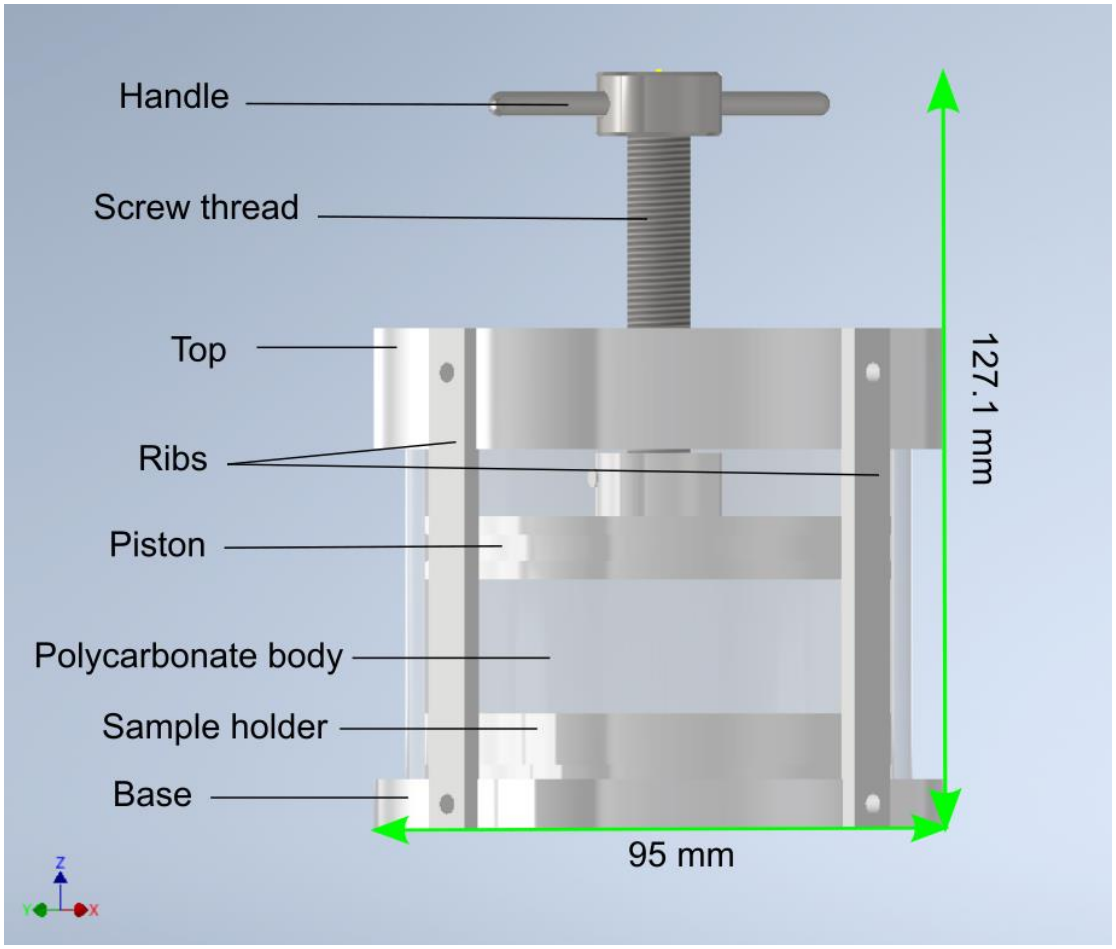

Figure 16. A labelled Autodesk model of the mark I apparatus.

Mark II replaced the handle with a hexagonal-shaped head, which was able to be tightened with a socket wrench, allowing for the measurement of torque as well as greater force application. After testing with core and gel samples, the second rendition of the press was found to experience leaks due to an inadequate seal between the core and side of the sample holder. An attempt was made to resolve this by applying heat-shrink tubing around the core samples (as shown in Figure 17). After the tubing was shrunk using a heat gun, it was hoped that it would provide a seal around the sample, preventing gel from entering the side of the sample, as well as create a tighter gasket between the core and sample holder.

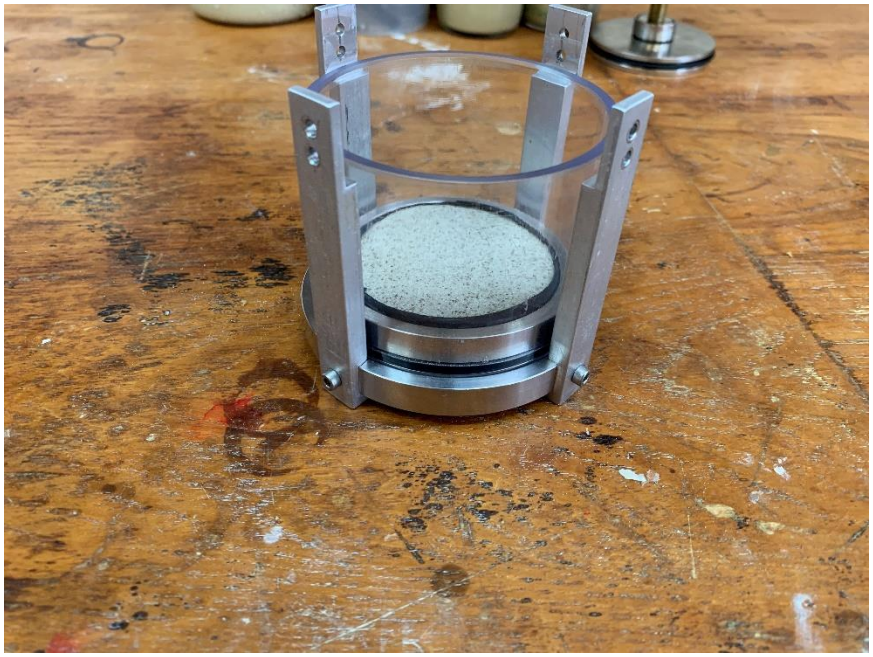

Figure 17. Heat-shrink tubing applied to a core sample. Source: author

Unfortunately, the application of this tubing did not fully prevent leakage and the press was sent back for redevelopment. A sample holder top and a detachable bottom, through which the core is now inserted, replaced the original sample holder within the apparatus (schematic shown in Figure 18) to create a strong gasket seal between the core and the instrument. Both the top and the bottom contain O-rings, which are compressed when the bottom is tightened on, creating a stronger seal between the sample holders and the core.

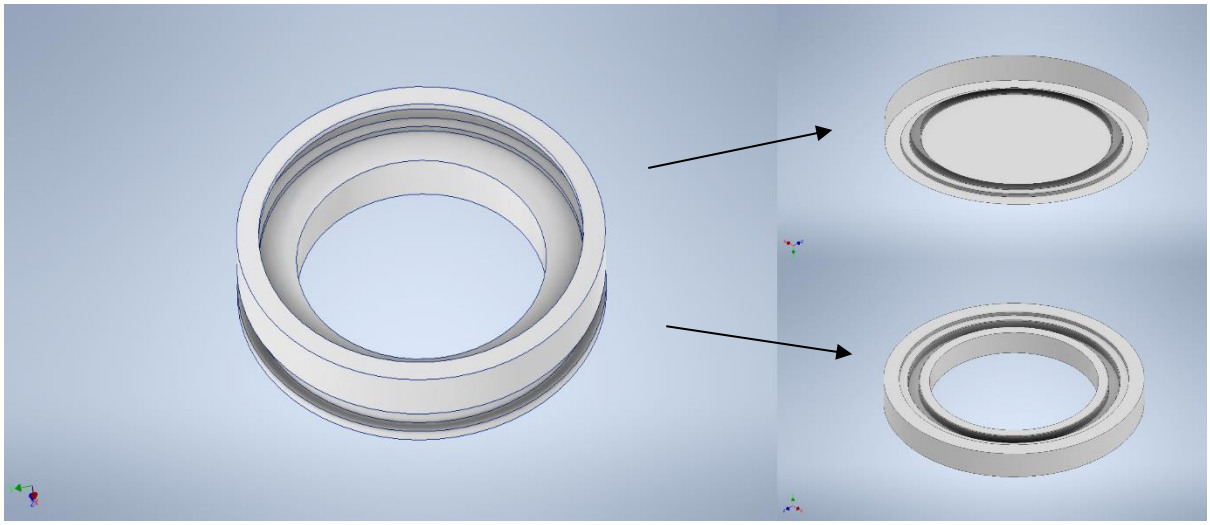

Figure 18. Schematics for the original sample holder (left), the new sample holder top, and the new sample holder bottom.

Mark III also experienced leakage however, albeit much more minor than in Mark II, leading to another change in the design. In the final version of the apparatus, small insertions were added to the bottom of the sample holder to better fasten it to the device (as shown in Mark IV within Figure 15). This final addition stopped gel from escaping the apparatus by providing enough force to compress the bottom O-ring.

2.5 X-ray diffraction

XRD is an analysis method in which an X-ray beam of a known wavelength is directed towards a crystalline mineral and the resultant angular position of diffracted beams is recorded (Allaby, 2013). At certain incident angles and wavelengths (satisfaction of the Bragg's law), when the primary X-ray beam comes into contact with the material, it will result in the beam being diffracted by reflections off successive lattice planes at an equal angle to the incident beam, resulting in intense reflected X-rays. Bragg's law is expressed as:

$$2d\ sin\theta = n\lambda \qquad \textit{Eq. 16}$$

Where d is the interplanar spacing (d-spacing) of the crystal, θ is the angle of incidence, n is the order of reflection, and λ is the wavelength of the incident X-rays. The diffractometer measures the target material intensity at a range of 2θ degrees. On the diffractogram, where a relative peak in X-ray intensity occurs, Bragg's law has been satisfied. Determining the interplanar spacing (d) allows for identification of minerals by calculating the d-spacing from the diffractogram peaks and comparing them with known reference values, therefore allowing the determination and characterization of minerals and other crystalline materials. While XRD experiments were planned to determine the mineralogical compositions (as well as provide an indication of elemental composition) of both the Berea sandstone and bentonite clay powder samples, these experiments were never able to be carried out due to COVID-19 and subsequent time constraints. XRD data was intended to be acquired for several reasons. First, by correlating XRD data with mechanical property measurements, insight could be gained into how changes in mineralogy can relate to changes in the mechanical behaviour of the sandstone. Secondly, as geomaterials are inherently heterogeneous and variable in their composition, XRD could be used to assess compositional differences from sample to sample and thus provide quality control for carrying out repeats and aid in reproducibility of the experiments.

2.6 Imaging

2.6.1 X-ray computer tomography

X-ray computer tomography (CT) has been chosen as one of the analysis techniques to observe rock-fluid interactions in this study. CT is a non-destructive analysis method allowing for visualisation of the internal structure of objects (Mees *et al.*, 2003). CT

images are generated by creating radiographs of X-ray attenuation values obtained during scanning (operating principle shown in Figure 19) and applying an image reconstruction technique to the radiographs (ibid). Attenuation is the reduction in the intensity of an X-ray beam as it passes through matter. Attenuation values are determined by the thickness, density (Compton effect), and the effective atomic number (photoelectric absorption) of the material that the X-ray is passing through (Ponomarev, Mamadaliev and Semenova, 2016).

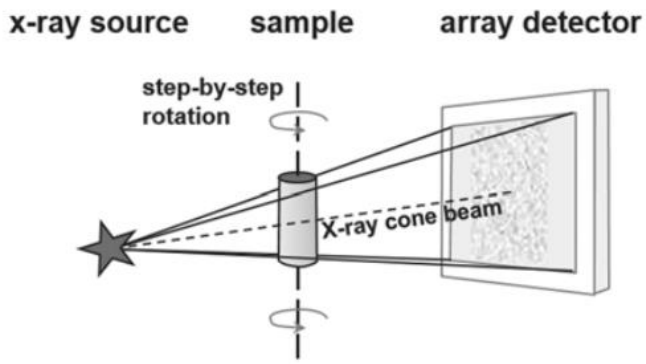

Figure 19. CT imaging principle. Taken from *Wennberg and Rennan, 2018*

Obtaining contiguous radiographs during scanning allows for 3D visualisation and quantification of 3D volumes of the sample. CT allows for a method to determine rock properties such as porosity (e.g., Taud et al., 2005), permeability (e.g., Mostaghimi et al., 2013), morphology (e.g., Wang et al., 2014) and reactive surface area and mineral phases (Lai, Moulton and Krevor, 2015). In this study, CT was used to determine porosity, reactive surface area, and mineral phases. Conventionally, CT analysis techniques are often correlated and evaluated against more traditional methods, such as scanning electron microscopy (SEM) (Kareem *et al.*, 2017).

For CT scanning in the study at hand, a Zeiss Versa 520 was used at the Maxwell Centre, Cambridge University. The true spatial resolution of the apparatus was 0.7 µm and it had a minimum achievable voxel size of 70 nm. The scan time for each sample was four hours. Samples were placed on a platform of phenol formaldehyde resin (floral foam) for the imaging process. The cores were then scanned with an air filter with a 0.4x optical lens, at a tube voltage range of 80 kV, and with an output of 7 W. The CT scans were carried out by Miss Tara Love.

2.6.2 Scanning electron microscopy

Scanning electron microscopy is the second imaging analysis technique used in this study. SEM is a form of microscopy that utilises a beam of high-energy electrons to produce signals at the surface of specimens. Instrumentation present in the microscope (Figure 20) can be narrowed down to five key components: a source of electrons; lenses for focusing the electrons into a beam; facilities for sweeping the beam in a raster; arrangement for detecting electrons; and an image display system (Reed, 2005).

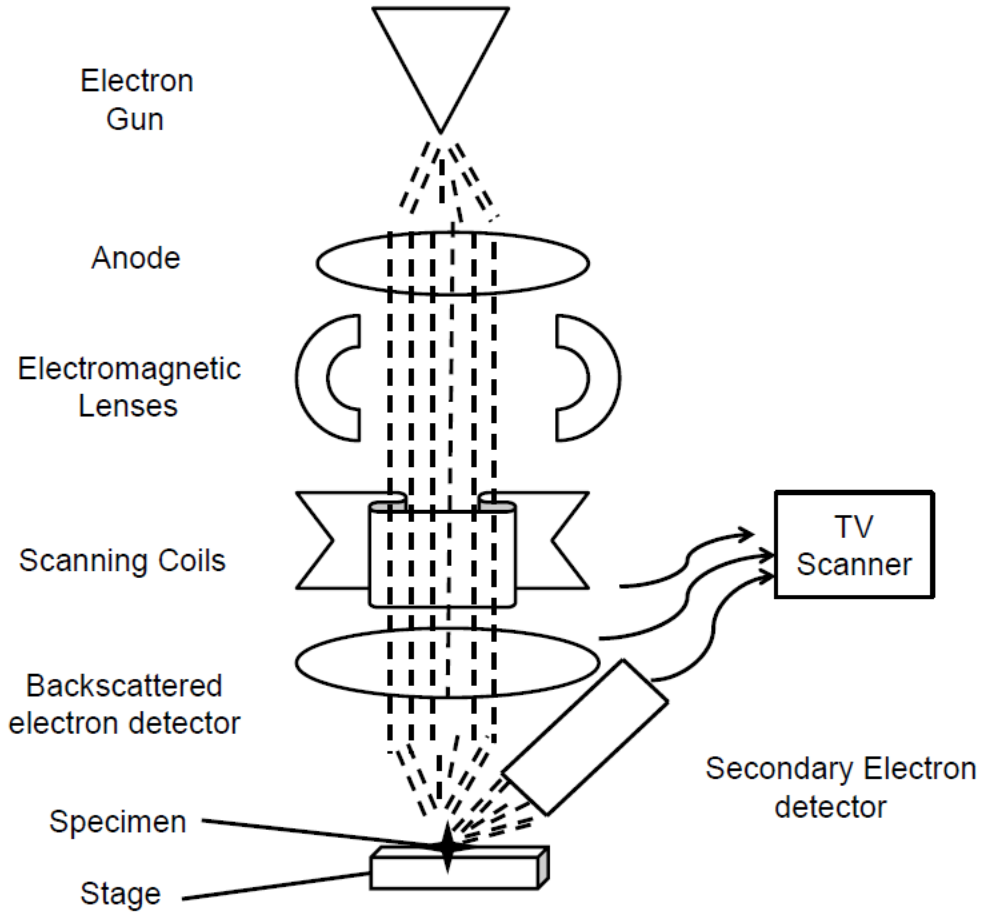

Figure 20. Schematic diagram of the major components of SEM. Taken from: Tare et al., 2009.

Common signals produced from electron-surface interactions include: secondary electrons (SE), backscatter electrons (BSE), characteristic X-rays, auger electrons, cathode luminescence, transmitted electrons, and specimen currents (Zhou *et al.*, 2006). These interactions can be classed as elastic or inelastic. Inelastic scattering occurs as a result of interactions between the incident electrons and atoms of the sample which leads to the transferal of energy to the sample atom. Elastic scattering occurs due to the deflection of the incident electron. Secondary (inelastic) and backscatter (elastic) electrons are the commonly used electrons for sample imaging. Secondary electrons are loosely bound electrons with an energy value of 3-5 eV, emitted by the primary beam striking the sample surface leading to the ionization of the specimen atom (ibid). These electrons mark the position of the beam and provide

information on sample topography as only surface electrons within a depth range of 5-50 nm are able to escape the sample and become secondary electrons (Chen, Xu and Chen, 2015). Backscatter electrons are those which escape (bounce back) from the surface with an energy >50 eV, scattered through an angle >90° and have undergone a single or multiple scattering events (Zhou *et al.*, 2006). Alongside providing topographic information, backscattered electrons also provide insight into the elemental composition of the sample. As an elements atomic number increases, the size of the nucleus also becomes greater, as a result of this more electrons are backscattered and subsequently the backscatter signal is higher. The backscatter signal can therefore be used to provide atomic number contrast in the image.

Electron microscopy in this study was used to attempt to determine the presence, extent, and effect of rock-fluid interactions at pore surfaces by image analysis, as well as the use of energy-dispersive X-ray spectroscopy for mineralogical identification (further explained in the following section). Conventional SEM image analysis was undertaken to determine morphology, mineral phases, and mineral texture before and after colloidal dispersion saturation respectively.

Environmental scanning electron microscopy (ESEM) operates on the same principles and produces the same interactions as a conventional SEM with one major exception. In ESEM, a gaseous environment is maintained around the sample as opposed to a conventional SEM in which a vacuum is used. This allows for imaging of hydrated samples as the significant gas pressure around the sample allows for the samples to be kept fully hydrated during imaging (Donald, 2003). Additionally, materials that act as insulators do not require coating with a metallic layer prior to imaging in ESEM. This is due to positive ions being produced in the ionizing collision that then drift down towards the sample and compensate charge build-up at the surface of the insulating

material (ibid). ESEM was considered for use after conventional SEM analysis of gel-permeated cores had failed due to difficulties in sample preparation (as outlined in Section 3.2.2), however, due to time constraints, the use of an ESEM was unable to be attempted. The utilisation of an ESEM would have allowed for imaging of wet gel permeated core samples, eliminating the need for drying. Bentonite gels, containing NaCl, have been shown to be viscoelastic (e.g., Benna-Zayani, 2009), however once dried, these gels will become brittle. When a dried gel-permeated core sample was cut in half and the cut surface was analysed under conventional SEM, little no gel structure was observed on the cut surface, it is speculated that this may be due to the cutting process having destroyed the brittle and dry gel structure (see Section 3.2.2). A wet gel may potentially survive the cutting process due to its viscoelastic mechanical properties (i.e., its ability to deform and absorb energy). Under this assumption, an ESEM would have allowed for the following analyses: observation of the structure of the clay minerals that have been formed as the gel has been pushed through the core sample, gel flow structures (e.g., does it follow certain paths), the coating of mineral grains (e.g., whether preferential coating of certain minerals takes place), and the distribution of the gel within the pore space. These petrographic observations could then have been linked to the mechanical strength of the rock-gel system.

2.6.3 Energy-dispersive X-ray spectroscopy

Energy-dispersive X-ray spectroscopy (EDS) is an elemental analysis technique utilised in this study that effectively simultaneously records X-rays of all energies to produce an output of a plot of intensity against X-ray photon energy. SEMs are commonly equipped with an EDS that utilises the X-rays produced in an SEM. When

the beam electrons from the SEM interact with inner shell electrons of the sample atoms under certain conditions, an inner shell electron can be ejected, resulting in the atom being in an energized state (Severin, 2004). A lower energy state is re-achieved when one of the outer shell electrons fill the vacant space in the lower energy shell, during which a photon with the energy equal to the difference of the two energy shells is potentially produced (ibid) (Figure 21). When such an X-ray photon is absorbed by the semiconductor in an EDS, Auger electrons and photo-electrons are generated, which in turn, dissipate their energy partly by raising atomic electrons from valence to conduction band, creating a brief pulse of current (Reed, 2005). The energy of these currents corresponds to specific elements, as the electron shell energy levels differ for each element, and are measured by the semiconductor (commonly made of Si(Li)).

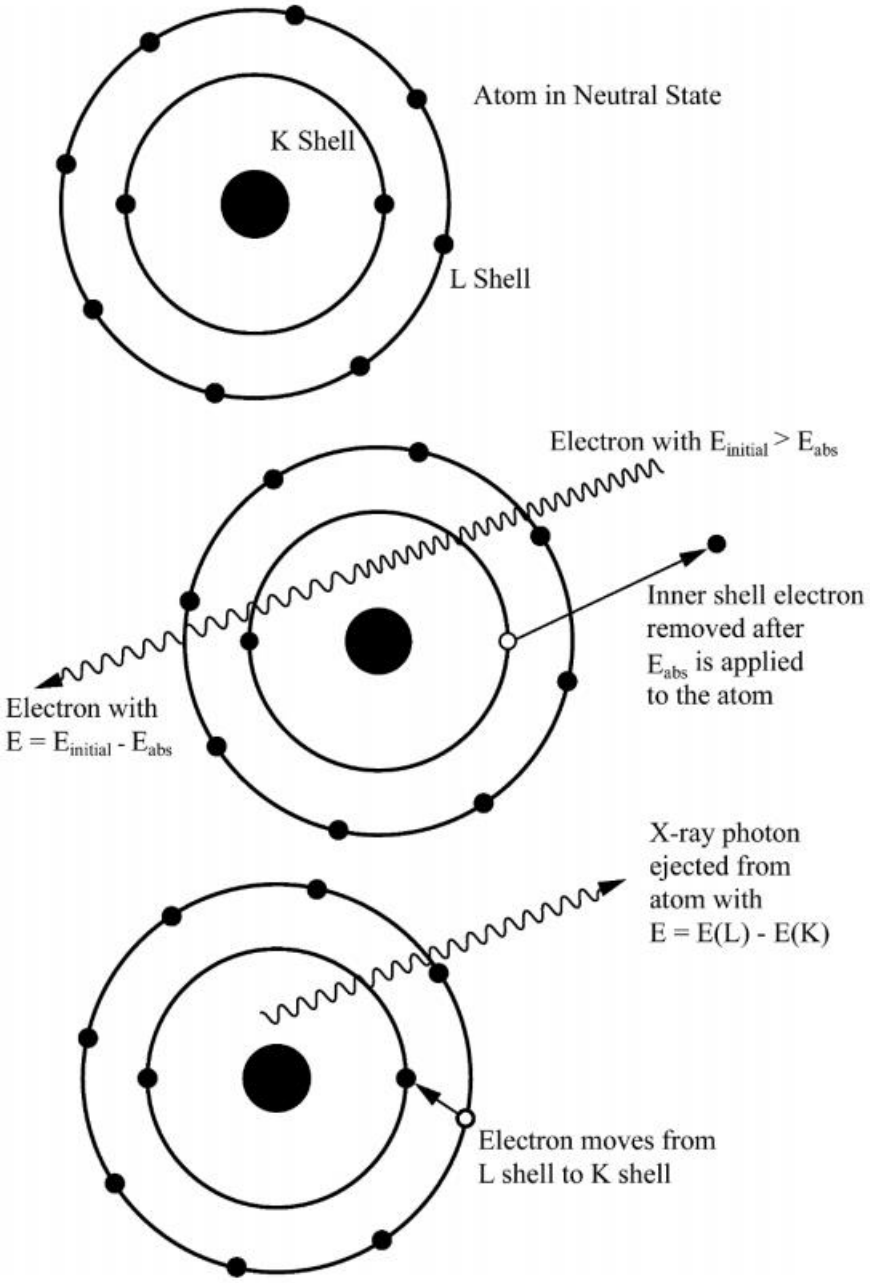

Figure 21. Illustration of the X-ray generation after electron excitation. Taken from: Severin, 2004.

2.6.4 SEM sample preparation and methodology

From pre-impregnated core samples, one polished thin section, 50 µm in thickness was prepared for each permeability range. A carbon coating of 25 nm was applied to the thin sections using a Cresington 108 carbon/A. SE, BSE and EDS analyses were then conducted using a Hitachi SU-70 field emission gun (FEG) SEM, which was

equipped with an INCA Energy 700 EDS system. The SEM was operated at a 15 kV acceleration voltage and a 15 mm free working distance. Oxford Instruments AZtec software was used for large area mapping (1 x 1 mm for each thin section), montage generation, and subsequently mineral phase analysis and identification using the generated montages. Additionally, a representative sample of each NaCl gel as well as the bentonite source material were prepared for SEM imaging. The gels were dried and placed on a carbon adhesive disc prior to analysis. Several sample preparation methodologies were attempted for the gel-permeated samples, however, these were unsuccessful (discussed further in section 3.2.2).

2.7 Image processing and analysis

Optical pore space analysis was conducted on SEM images utilizing a method of thresholding pore space from digital photomicrographs based on global thresholding using Avizo software (version 2019.1) by Thermofisher Scientific. CT results were also processed and analysed using Avizo.

2.7.1 CT processing and noise reduction

The CT dataset consisted of a single 3D image from a scan of three 175-300 mD cores (a non-permeated core, a dried gel-permeated core, and a wet gel-permeated core) that were stacked on top of one another. The dataset was split into three separate image stacks (stored as TXM files), one for each core, with each stack being processed and analysed separately in Avizo.

Upon importing the image stacks to Avizo, it was observed that artifactual concentric rings had been superimposed onto the tomographic images (as shown in Figure 22).

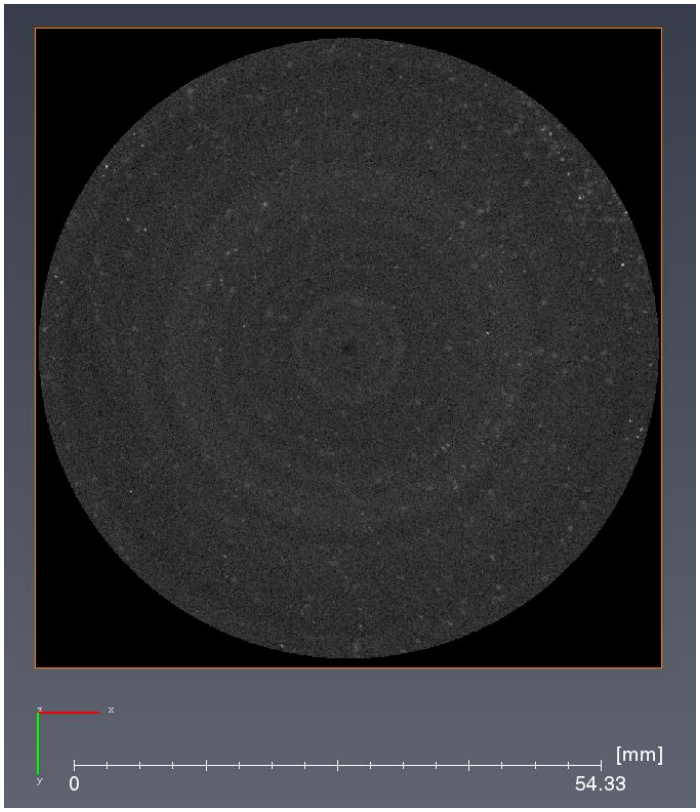

Figure 22. A 2D slice within the image stack for the non-permeated sandstone core showing ring artifacts.

The rings appear due to defect detector elements that continuously either over- or underestimate CT attenuation values (Kyriakou, Prell and Kalender, 2009). To correct for this artifact within the scanned images, the *Ring Artifact Removal* module (a module being a standard, pre-programmed, algorithm within Avizo) was applied to each image stack. The algorithm works by comparing mean voxel values of each ring and the mean voxel values of the whole sample, and then adjusting the ring voxel values accordingly. Once these artifacts had been corrected, a *median filter* module was then applied to the image stacks in order to reduce salt and pepper noise, with the *median filter*, in simplified terms, functioning by attenuating high frequencies and noise whilst letting low frequencies pass through the filter.

Once a stack had undergone artifact removal and filtering, it was then split into three even sections (through the Z axis) by the use of *Extract Subvolume* modules (Figure 23).

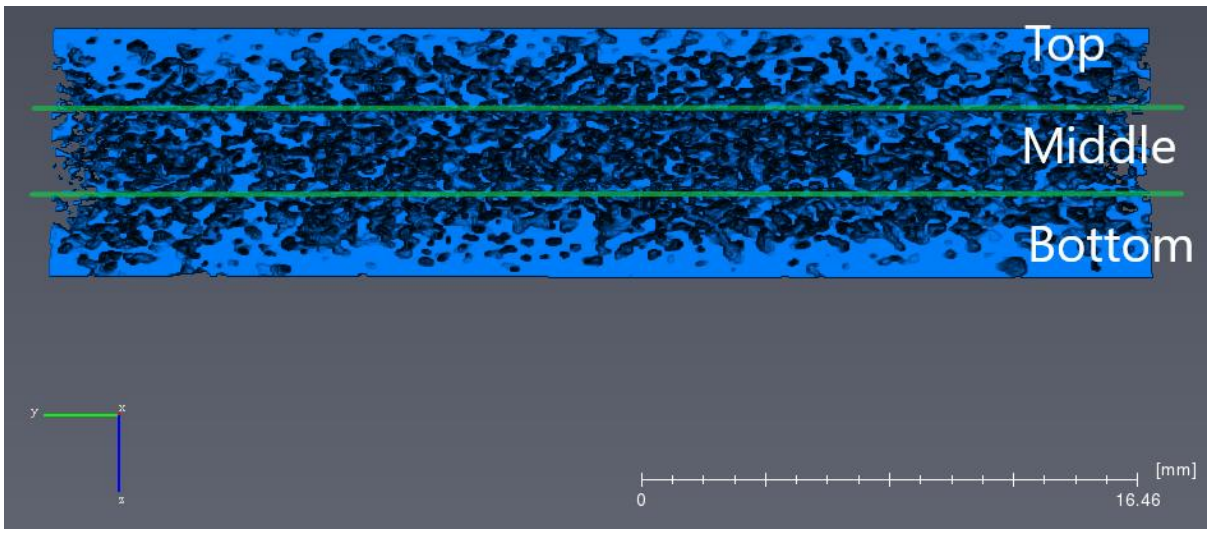

Figure 23. Division of the non-permeated 175-300 mD sandstone core through the Z axis into three sections, with the top surface of the top section being where the gel would be permeated from in Batch I and Batch II samples.

Analyses described in the following chapter were applied separately to the top, middle, and bottom section of the cores in order to assess how the rock properties vary perpendicular to the surface from which the gel was permeated from.

2.7.2 Porosity, pore connectivity, and pore volume analysis

The images stacks were manually segmented using the global thresholding approach within the segmentation editor in Avizo (interactive thresholding). Global thresholding is a method where a single grey scale value is selected in order to separate regions of interest based on user analysis of the image and its histogram (Iassonov, Gebrenegus and Tuller, 2009). In the case of this study, the regions of interest are the pore space and the solid rock material within each core sample. The grey scale values used to separate these two regions (an example is shown in Figure 24) were first

determined for the unsaturated sandstone core (for the top, middle, and bottom sections), as a reference values for the porosity of the core samples had been provided by the supplier, which in the case of 175-300 mD sandstones was 19-20%. Using the reference porosity, grey scale values that provided a matching porosity for each section of the core sample were determined. For gel-saturated samples, the same histogram values as the control sample (normalised, as the raw values varied between samples) were used to determine the porosity, pore connectivity, and pore volume values.

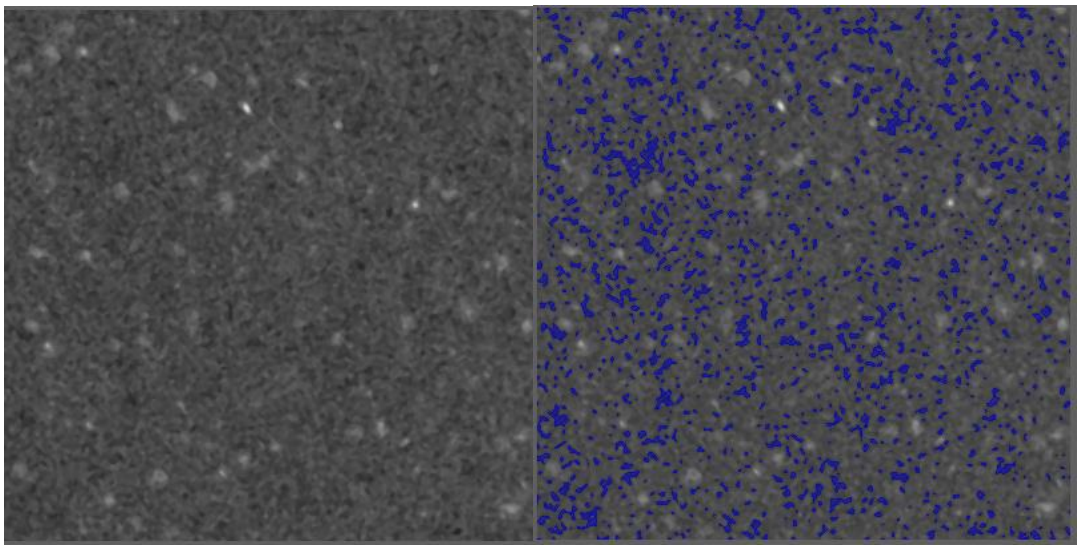

Figure 24. A slice of the 175-300 mD (control batch) core through the XY axis. Right: no masked voxels selected. Left: masked voxels selected corresponding to assumed porosity.

To determine connected pore space, first, a *Labelling* module was applied to the segmented image stacks. This module assigns a spatial value to each pixel that was classed as pore space during segmentation. This spatial dataset then had an *Axis connectivity* module attached to it, which allows for the calculation of only the connected porosity of the sample. Pore volume was calculated using the *label analysis* module, which computes a group of measures for each cell (cells in this case being pores) including volume, area and diameter.

An overview of all the modules applied to each of the analysed samples in Avizo is given below (Figure 25).

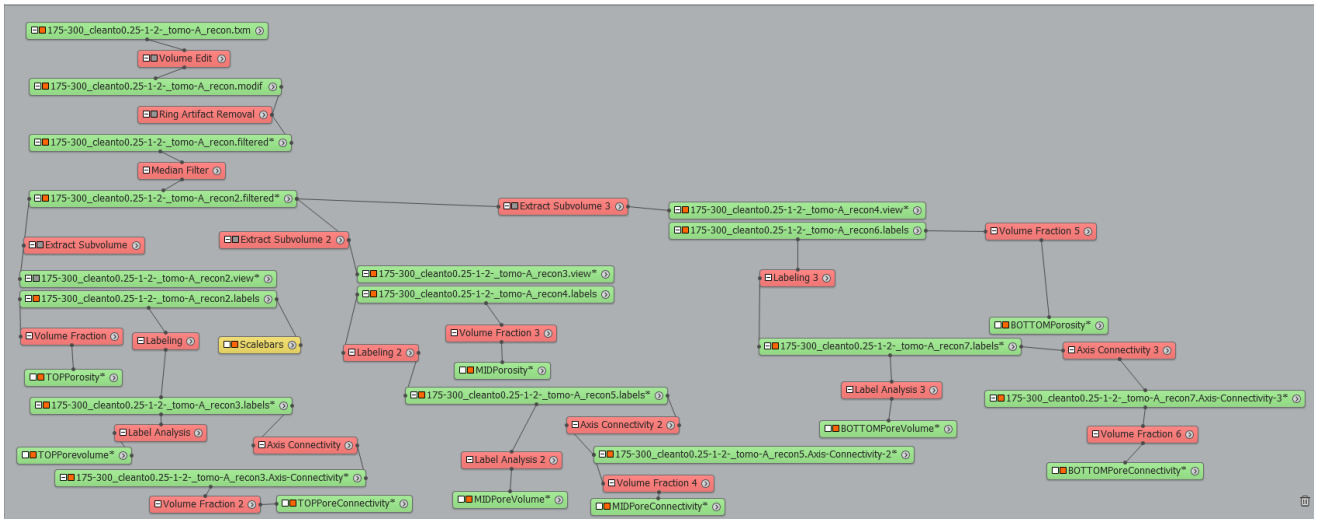

Figure 25. Visualisation and analysis workflow within Avizo for a non-permeated 175-300 mD Berea sandstone core.

2.8 Indentation testing

Indentation was the chosen method of mechanical testing for non-permeated and gel-permeated cores in this study. The reason indentation was selected over more conventional testing methods (e.g., uniaxial compressive test, triaxial compressive test, Brazilian test, etc.) was due such conventional testing being expensive and time-consuming. These tests require significantly larger core samples than those precured in this study, which not only would have increased the cost of acquiring the cores, but also would have required a bigger and much more advanced permeation apparatus to fully saturate the cores with gel.

Indentation testing is used for characterisation of material behaviour under load. The basic premise of indentation is to press a stiff indenter against a material that is

relatively softer (in the case of rock, conventionally the indenter is pressed perpendicularly against the surface). The generalised indentation process for rock can be seen as occurring in several distinct stages. Firstly, compression of the rock under loading occurs, this is then followed by a brittle fracture accompanied by the formation of loose fragments, with the last stage being ductile yielding of the rock with broken material being displaced towards the free surface (Murthy, 2021). Key variables in indentation testing are the diameter and geometry of the indenter, strain rate, rock microstructure and properties, and presence of planes of weakness (ibid).

Indentation tests can be broadly subdivided into sharp indenter and flat indenter procedures (Ciavarella, 1999). Sharp indenters include wedge, pyramidal, and conical tips. Flat indenters have spherical, cylindrical and blunt indenter tips. Both types present advantages and drawbacks. For example, sharp indentation, at the vertex of the indenter, has a limited amount of plasticity which results in the formation of a residual stress field, which in turn promotes crack initiation. Flat indenters, on the other hand, leads to a distinct non-singular stress field (ibid), as is the case in this study.

A flat indenter under quasi-static loading conditions was used to determine a load-displacement curve for control and saturated samples at the Material Science department, Cambridge University. A Tinius Olsen model 25ST (maximum pressure of 25 kN) universal testing machine (UTM) was fitted with a 2 mm flattop cylinder indenter insert that was made of tungsten carbide. Force was applied at a fixed rate of penetration of 0.05 mm/s and the samples were not subjugated to any confining pressure. The endpoint of each indentation experiment was taken to be either the point at which the sample fully fractured (in which case it would be manually stopped) or until the indenter reached the bottom of the sample holder. The indentation experiments were carried out by Miss Tara Love.

2.9 Indentation data processing and analysis

2.9.1 Software used

Datasets were statistically analysed using Excel version 2203. P values were determined using the t-Test: Paired Two Sample for Means function (Alpha: 0.05) within the Excel Analysis Toolpak. Standard deviations for the control samples (which had repeats) were also determined within Excel, using the STDEV.S function. Graph generation was done in RStudio version 1.4.116, utilising the packages ggplot2, Grid, RcolorBrewer, and Gridextra, as well as the RStudio default library. Pasco Capstone (version 2.4.1) was used in deriving measurements of mechanical properties of the sandstone cores from their stress-strain curves.

2.9.2 Unit conversion

As force and displacement are extrinsic properties, that is to say their values are dependent on the amount of material present, it is necessary to convert them into quantities that reflect the properties of the material regardless of dimensions. Therefore, force and displacement are converted into stress (σ) and strain (ε) respectively:

$$\sigma = \frac{F}{A} \qquad \textit{Eq. 17}$$

$$\varepsilon = \frac{\Delta d}{L} \qquad \textit{Eq. 18}$$

where F is force, A is area of the indenter surface in contact with the sample (3.1416 mm^2), Δd is the displacement of the indenter, and L is length of the sample (6.35 mm).

2.9.3 Young's modulus

Young's modulus was calculated from stress strain curves by computing the slope of the primary linear (elastic) region, i.e., m in y = mx + b, (e.g., Figure 26) in each sample. The calculation of m was done using the 'Slope Tool' function in Pasco Capstone.

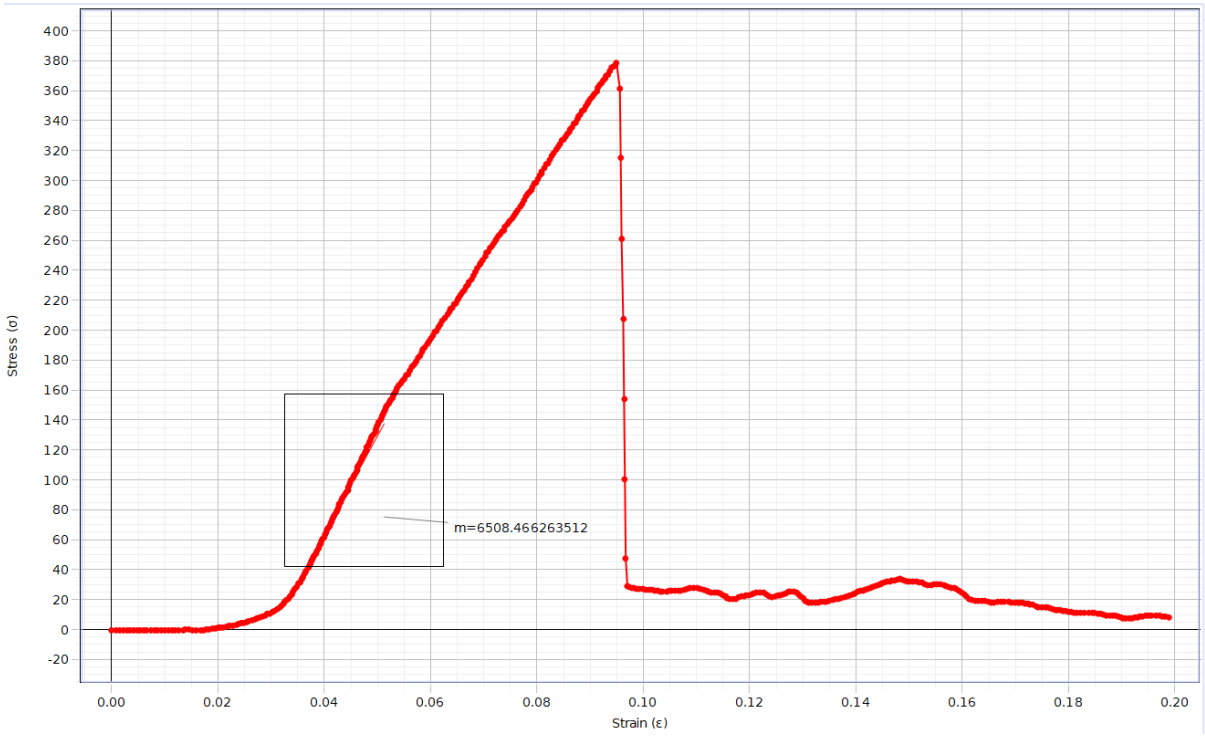

Figure 26. An example of a slope value for the elastic region of a stress-strain curve using the 'Slope Tool', calculated in Pasco Capstone.

2.9.4 Modulus of toughness and fracture energy

Material toughness modulus (U_T) was determined by integrating the stress strain curve prior to the point of fracture:

$$U_T = \int_0^{\varepsilon_f} \sigma d\varepsilon \qquad \textit{Eq. 19}$$

Where ε is strain, ε_f fracture strain, and σ is the stress (Soboyejo, 2002). Fracture energy or post-crack absorption energy was determined in a similar manner with the integration of the post-fracture stress-strain curve. Integration of the stress strain curves was done for each sample using the 'Area Under the Curve' function within Pasco Capstone (example provided in Figure 27).

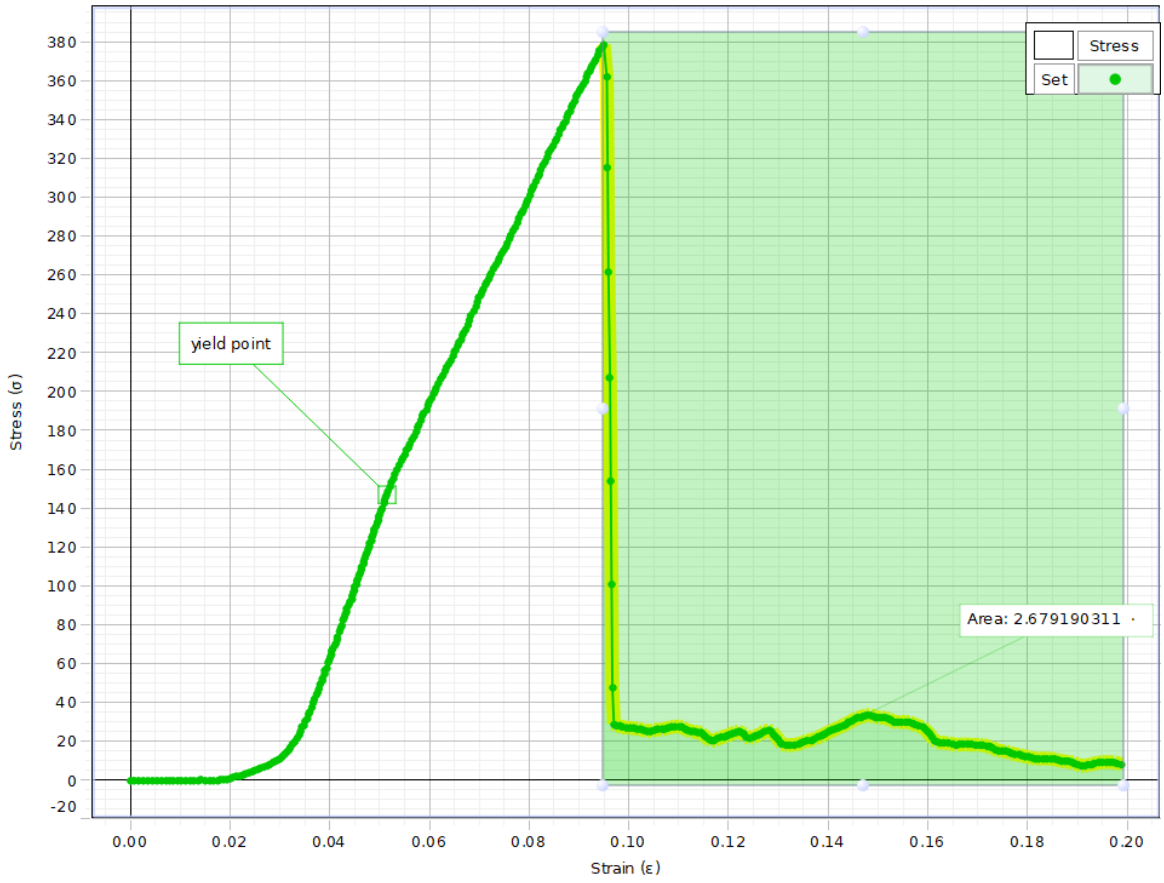

Figure 27. An example of a fracture energy area value using the 'Area Under the Curve' function, calculated using Pasco Capstone.

2.9.5 Yield strength, ultimate strength, and maximum displacement

Yield strength, ultimate strength, and maximum displacement were determined qualitatively from stress-strain and force-displacement curves. Yield strength was measured from stress-strain curves by determining the end-point of the primary elastic region based on user analysis. Ultimate strength was the highest recorded stress value of the stress-strain curve, and maximum displacement was, as the name implies, the highest displacement value observed during indentation.

3. Results

3.1 Rheology

3.1.1 Viscometer results

The results for 10-second and 10-minute gel strengths are provided in Figure 28, and yield point, apparent- and plastic viscosity are shown in Figure 29. The 10-second gel strength, 10-minute gel strength, apparent viscosity, and yield point seem to exhibit a negative exponential relationship with salt concentration, while plastic viscosity is seemingly random. Due to the extremely high gel strength, plastic viscosity, and yield point exhibited by the 1.16% (wt/vol) NaCl gel relative to other gels, it was decided for it to be removed from further experiments as it was assumed to be too viscous for permeation into core samples. Repeats were not carried out for the viscometer experiments and thus no error bars were able to be applied to Figures 28 and 29. However, Rye (2017) carried out a statistical analysis of rheological measurements, of water-based drilling fluids by Fann 35 viscometers. The author concluded the Fann 35 to be both precise and accurate. Using the Fann instrument, 300 rpm readings were taken for five sample sets (ranging between 4 and 8 samples) of different

compositions, at 25°C, on fluids aged for 24 hours (similar to the conditions in the study at hand). Standard deviation ranged from 1 to 14.9 lb/100 ft^2, and the average variation from the mean was between 0.5 and 2.3%.

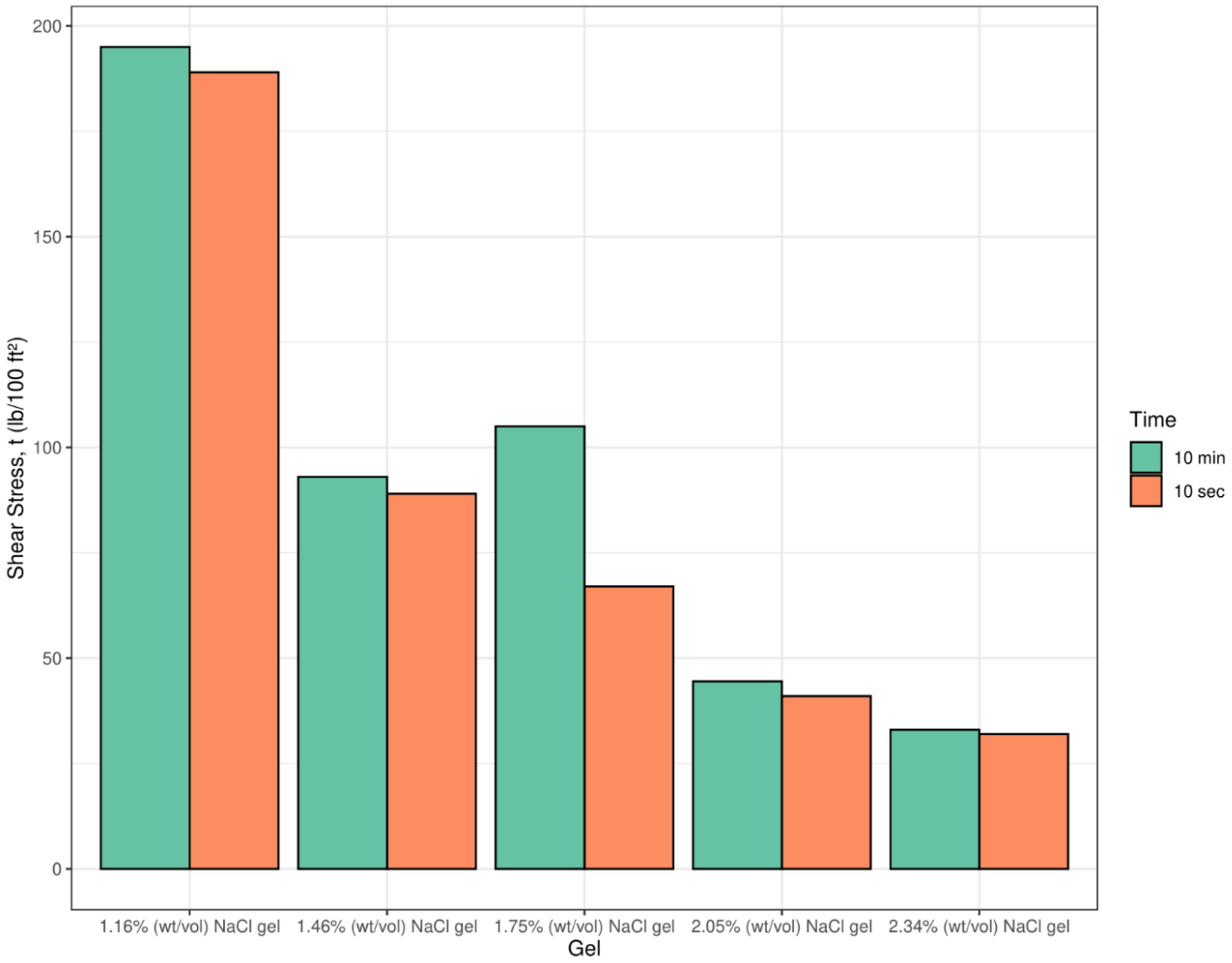

Figure 28. The gel strength of a 10-second and 10-minute gel for bentonite gels of various NaCl concentrations.

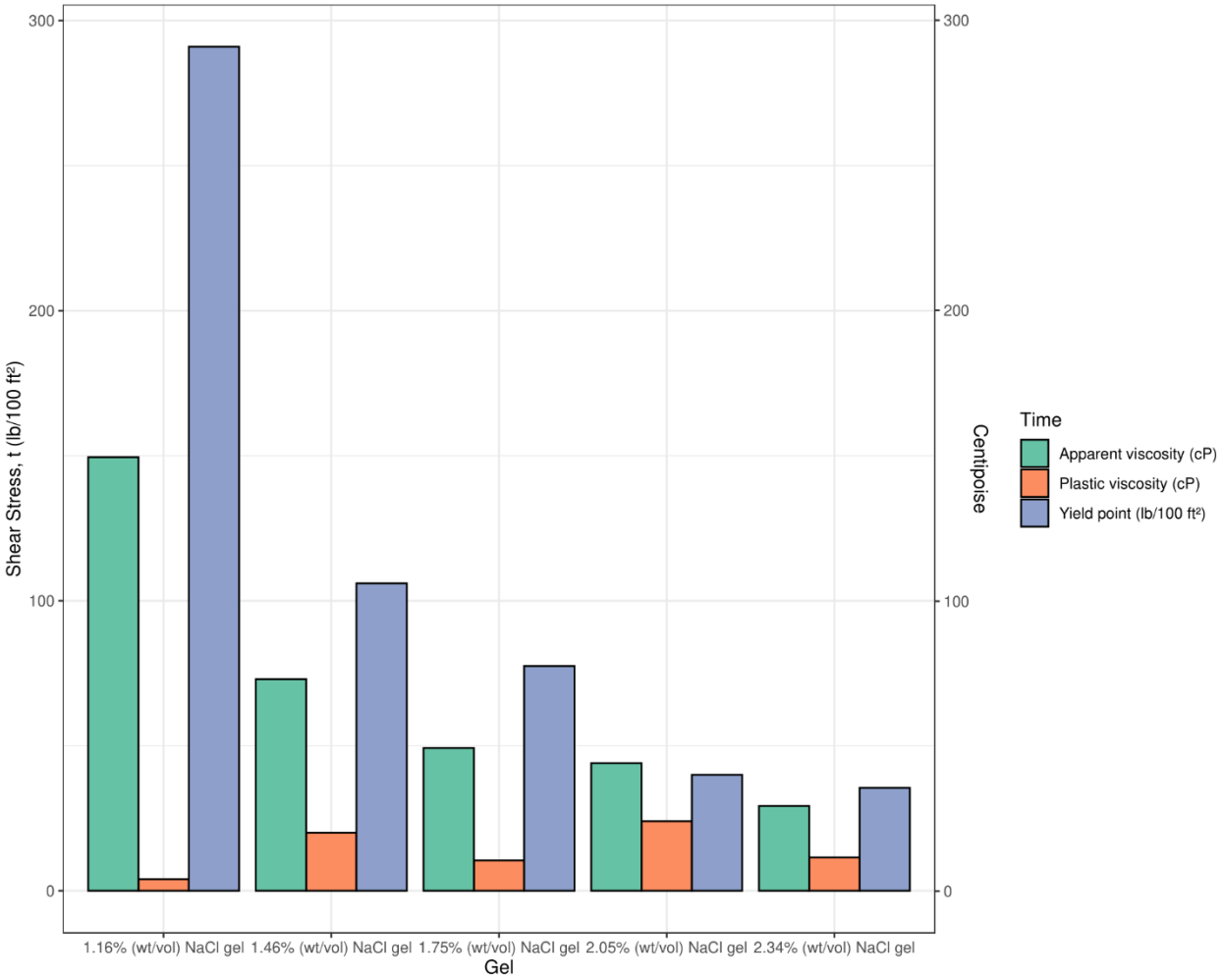

Figure 29. Apparent viscosity, plastic viscosity, and yield point in bentonite gels of various NaCl concentration.

3.1.2 Filter press results

Filter press measurements are shown in table 7, the data from which the filter cake permeabilities in table 8 were able to be calculated.

Table 7. Experimental parameters and results for filter press testing of bentonite gels of varying NaCl concentrations

Sample	Gel volume (ml)	Pressure (psi)	Time (min)	Filter cake thickness (cm)	Filtrate volume (ml)	Filtrate flow rate (cm^3/sec)	Gel apparent viscosity (cP)
2.34% (wt/vol) NaCl	50	200	5	0.7	4.5	0.015	29.25
2.05% (wt/vol) NaCl	50	200	5	0.9	3.4	0.011	44

1.75% (wt/vol) NaCl	50	200	5	1	2.7	0.0083	49.25
1.46% (wt/vol) NaCl	50	200	5	1.3	2	0.0066	149.5

Table 8. Filter cake permeabilities for bentonite gels of varying NaCl concentrations, calculated from the filter press results as outlined in section 2.3.

Gel sample	Filter cake permeability (mD)
2.34% (wt/vol) NaCl	0.71
2.05% (wt/vol) NaCl	1.01
1.75% (wt/vol) NaCl	0.95
1.46% (wt/vol) NaCl	2.98

3.2 SEM results

3.2.1 Problems during SEM analysis of non-permeated samples

The four thin sections prepared from non-permeated Berea sandstone cores, one for each permeability range, contained a large amount of Al_2O_3 fragments in the pore space between mineral grains (e.g., Figure 30). These shards were introduced into the thin section as a result of either poor sample preparation, most likely during the cutting or polishing process, or inadequate cleaning of the samples prior to SEM analysis.

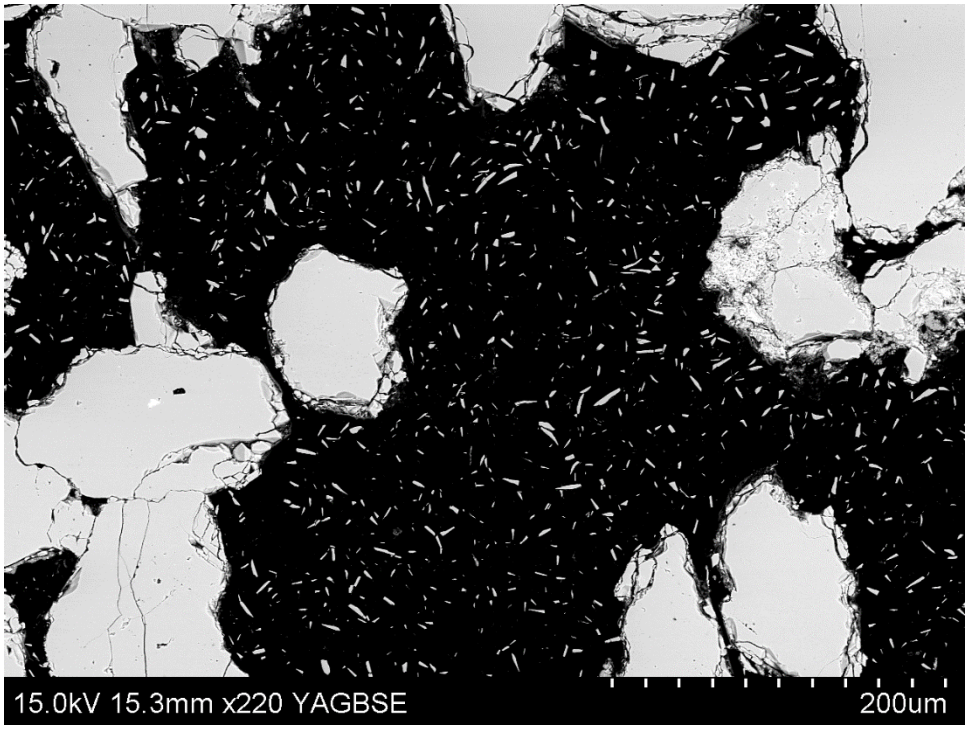

Figure 30. Al_2O_3 shards occupying the pore space in a polished thin section of the >500 mD permeability Berea sandstone.

The presence of the shards severely impacted mineralogy and porosity analysis of the SEM micrographs. As the mineral area fraction measurements were normalised to a percentage scale, the large quantity of Al_2O_3 offset these measurements, thus giving faulty mineral fractions. As such, only the samples with the lowest number of shards present (<75 mD and 175-300 mD sandstones) in their large area maps underwent mineral area fraction analysis. It was anticipated that upon the completion of a successful set of gel-permeated samples for SEM analysis, another batch of better prepared non-permeated core samples would be made as well, this however never came to fruition due to reasons discussed in Section 3.2.2. Porosity analysis using global thresholding was also complicated due to the high attenuation value of the fragments (meaning porosity values would be lower than in reality), and as such, measurements were once again only made for the large area maps with the lowest number of shards present.

3.2.2 Problems with SEM sample preparation of gel-permeated samples

In order to observe the clay gel within our rock under conventional SEM, several sample preparation methodologies were tried. Initially, a gel permeated sample was attempted to be analysed without any sample preparation bar drying (which is necessary for conventional SEM). The core was cut perpendicular to its breadth (Figure 31) and the cut surface was analysed under SEM.

Figure 31. Cut face of a sandstone core sample permeated with gel and subsequently dried. Black marking denotes the surface from which the gel was permeated from.

This first method, however, was not able to retain the gel particularly well. Only the area close to the surface from which the gel was permeated from (presumably where the gel is most concentrated), displayed any significant amounts of the gel material (Figure 32 and 33). It was assumed that either the cutting process had removed much of the gel from the analysed surface, or the gel had not properly permeated through the core, and thus different sample preparation methods were attempted next.

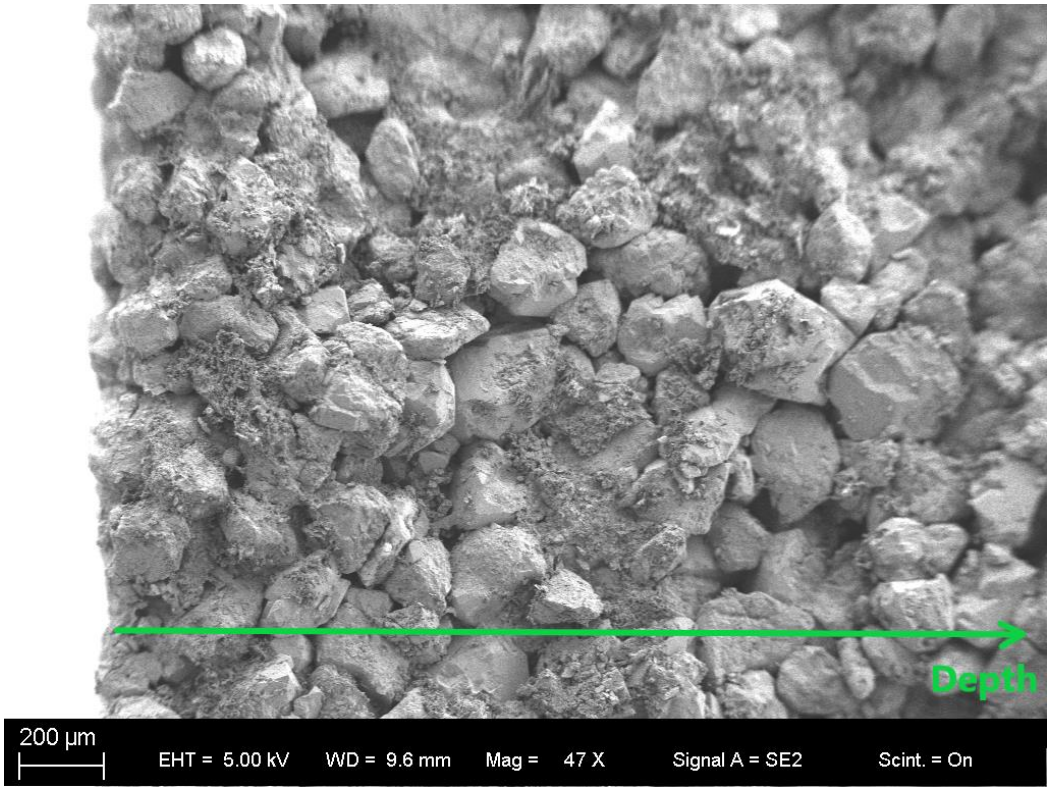

Figure 32. A SE image of the 'no preparation' gel permeated sandstone's cut surface, with the left-hand edge of the image being where the gel was permeated from. From the permeated surface, a decreasing amount of gel material is (qualitatively) observed with increasing depth.

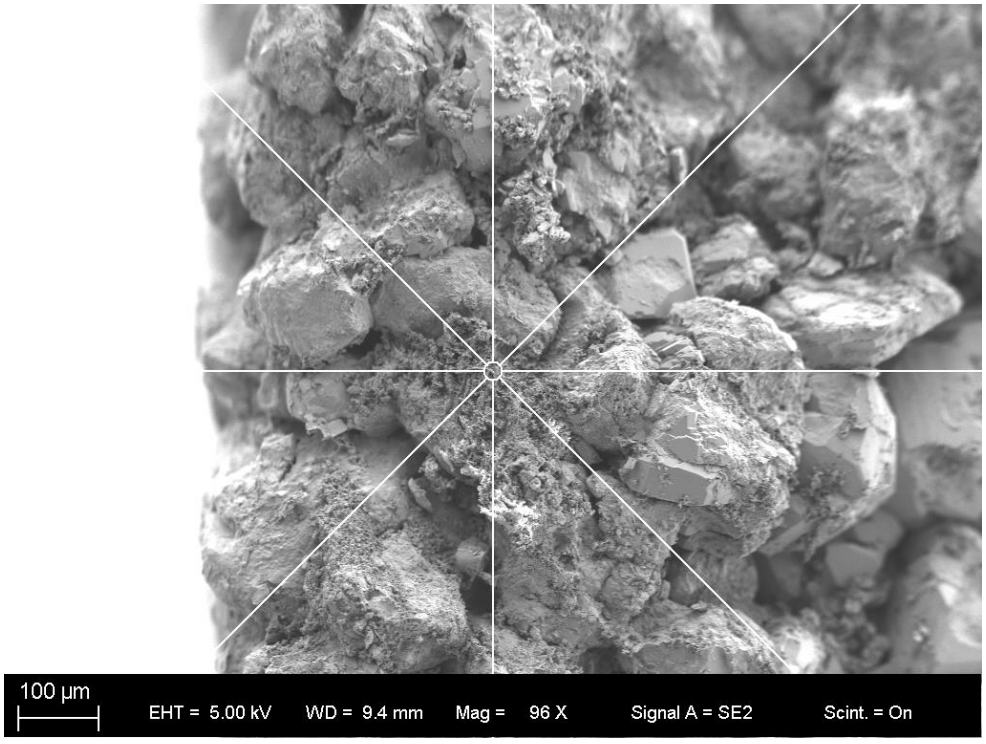

Figure 33. A further zoomed-in SE image of the left-hand section of Figure 32, showing the gel coating grains and filling pore space within the sandstone sample.

Next, the sandstones were impregnated with polymer in hopes that it would retain the gel, as polymer impregnation has been shown to stabilise the microstructure of fragile specimens, allowing them to better withstand the stresses of grinding and polishing without inducing alterations (Kjellsen *et al.*, 2003). These impregnated samples were then prepared as thin sections. Both standard and polished thin sections were prepared, with both wet and dry cutting, grinding, and polishing methods. Unfortunately, the gel was still unable to be retained in these samples for SEM analysis with no gel being observed in the thin sections. Next, resin impregnated samples were mounted and polished (the polished face, once again, being the cut face, perpendicular to where the gel was permeated from) to observe a depth profile. In the mounted samples, the gel was found to have seemingly dissolved in the preparation process (e.g., Figure 34, 35, and 36), showing that the gel had likely permeated through the core but not survived the sample preparation process.

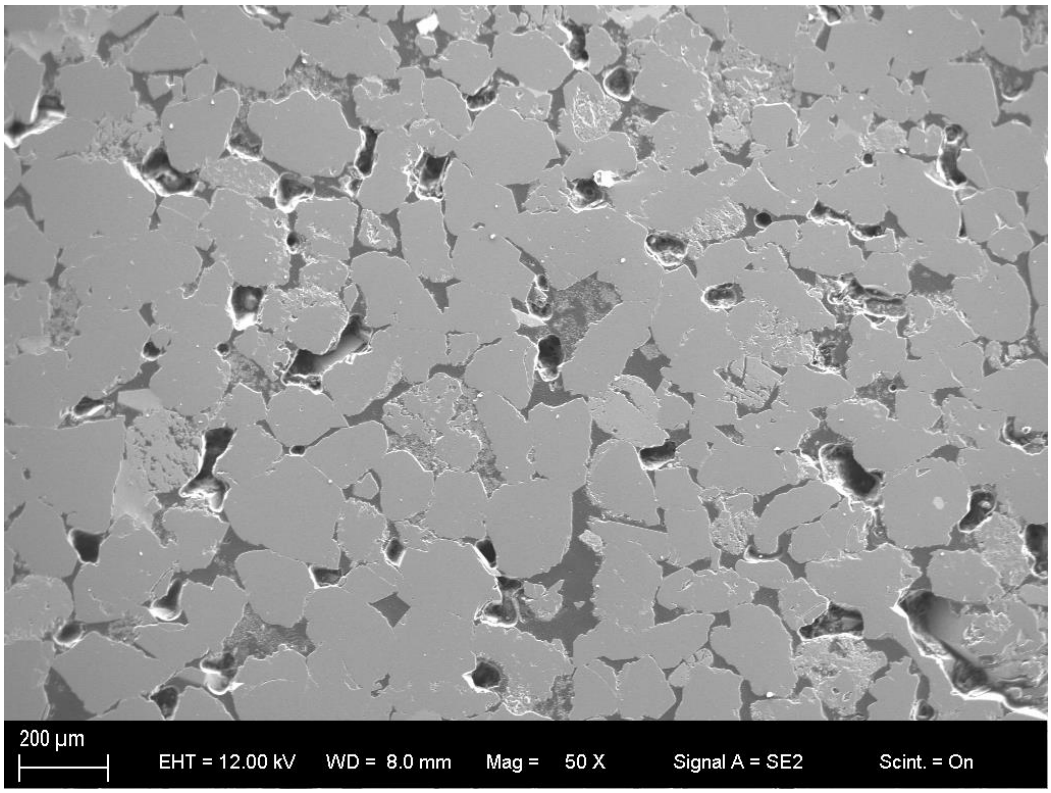

Figure 34. A SE image of a thin section of a gel-permeated sandstone sample showing craters from where the gel has dissolved

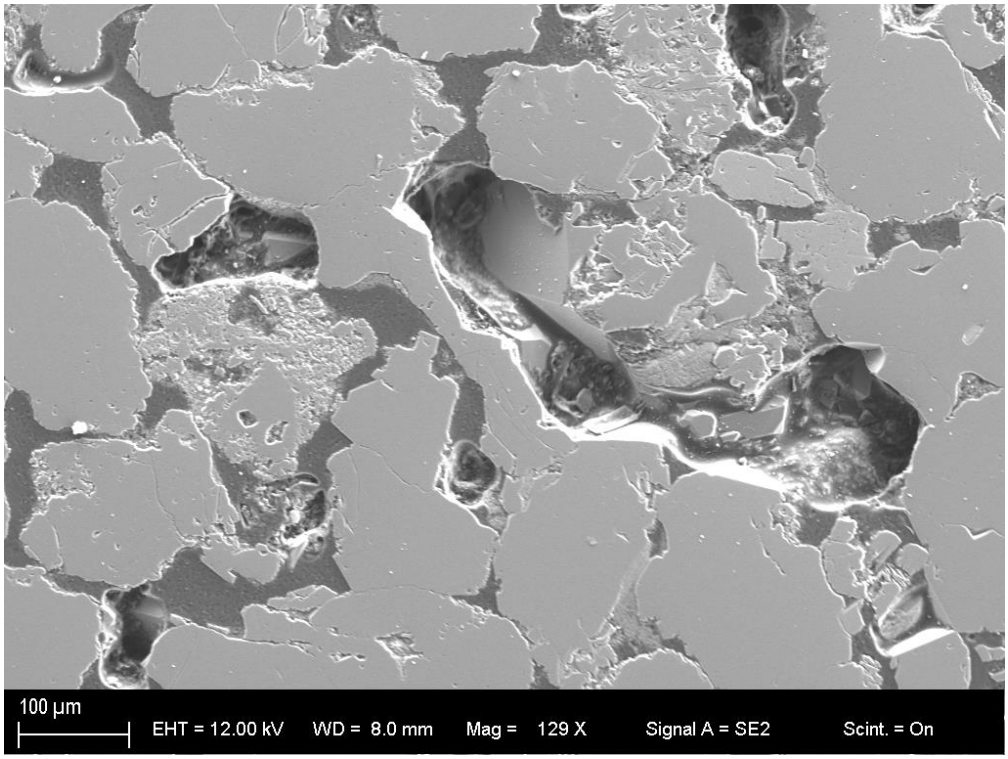

Figure 35. A further zoomed-in SE image of the bottom right-hand section of Figure 29, showing the craters in greater detail.

Another qualitative observation based on the micrographs of both the sample with minimal preparation (e.g., Figure 32), as well as those impregnated with epoxy (e.g., Figure 36), is grain compression near the permeation surface. Compression could have a significant impact on the mechanical properties of the rock and ought to be quantified in future studies.

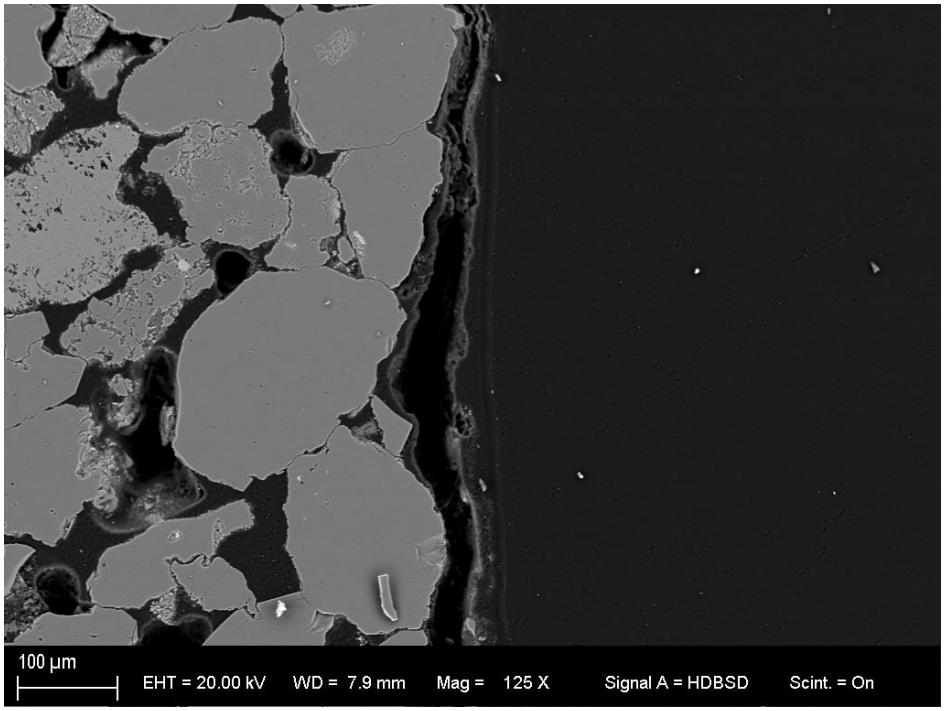

Figure 36. A BS image of a thin section of a gel permeated sandstone's cut surface, with the right-hand edge of the image being where the gel was permeated from.

Due to time constraints, further attempts at SEM analysis of the gel-permeated core samples were foregone within this study.

Dried gels were also analysed under SEM to observe what the cast morphology of the gels looks like. This was done in an attempt to correlate this morphology to that of the gels present in permeated sandstone samples, which had the gel-permeated sample preparation been successful, would have allowed for easier identification of the gel material present in the pore space and enabled the inference of more meaningful information from the permeated samples. Examples of SEM images for the 1.46% (wt/vol) NaCl, 1.75% (wt/vol) NaCl, 2.05% (wt/vol) NaCl, and 2.34% (wt/vol) NaCl gels are provided in Figure 37.

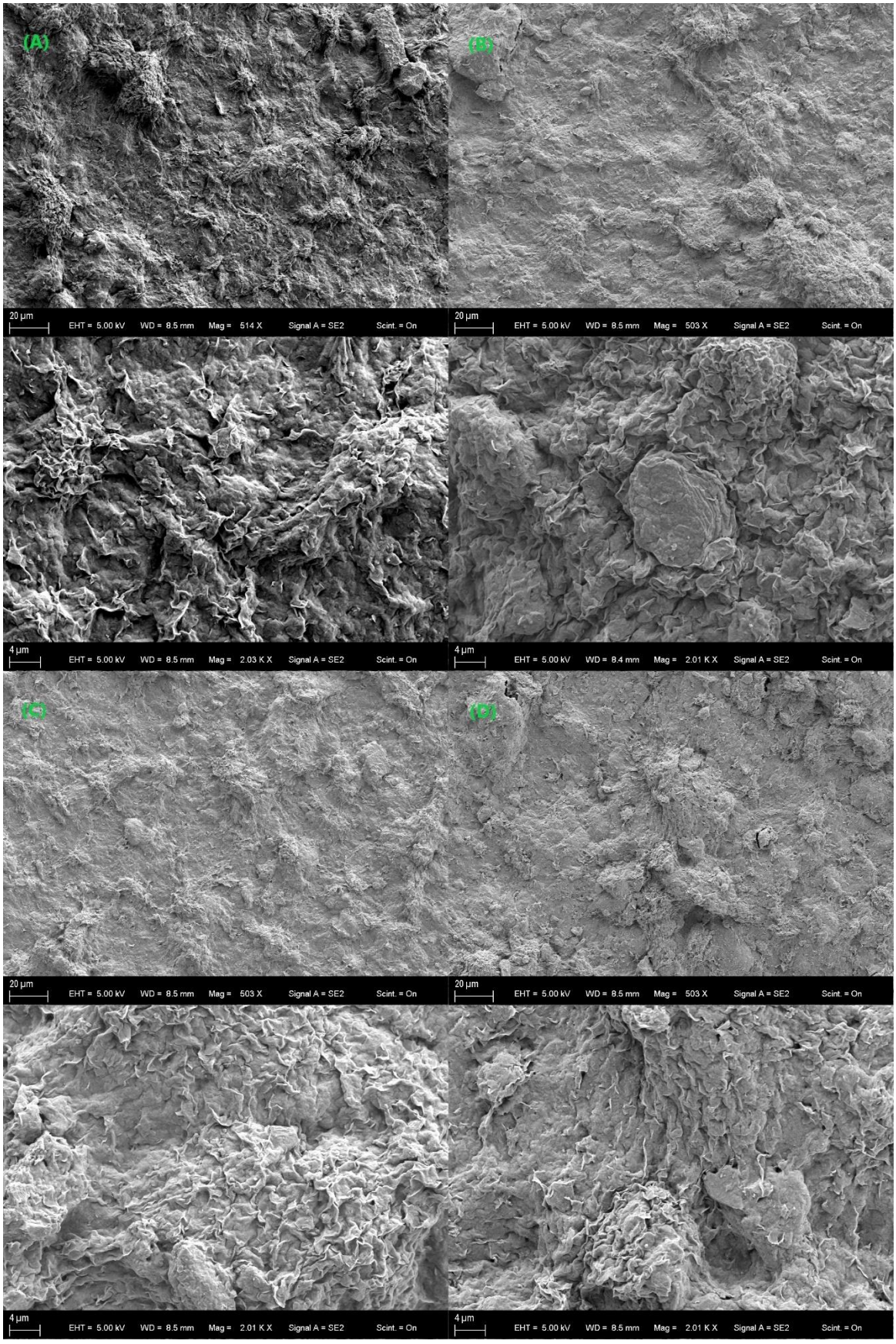

Figure 37. SE images of dried gel samples at 20 µm and 4 µm scales. A: 1.46% (wt/vol) NaCl gel. B: 1.75% (wt/vol) NaCl gel. C:2.05% (wt/vol) NaCl gel. D: 2.34% (wt/vol) NaCl gel.

3.2.3 Mineralogy and porosity results for non-permeated samples

Mineral phases identified from samples of all four permeability ranges using EDX are given in Table 9, with the mineral area fractions of the <75 mD and 175-300 mD samples shown in Table 10, and the porosity measurements in Table 11. The montaged map data from which the mineral area fractions are derived from are presented in Figure 38.

Table 9. Description of the identified mineral phases using SEM/EDX. *What was identified as corundum are the Al_2O_3 shards from sample preparation.

Group name	Major mineral	Minor mineral
Quartz	Quartz	
Feldspar	Orthoclase	Albite
Clay	Illite, kaolinite	chlorite
Other	Ankerite	Siderite, rutile, corundum*, calcite

Table 10. Mineral area fractions from SEM/EDX analysis. *Values have been rescaled using min-max normalisation to show mineral area fractions excluding the measured pore space fraction.

Sample	Mineral group	Area fraction*
<75 mD	Quartz	82.8
	Feldspar	0.4
	Clay	15.9
	Other	0.9

175-300 mD	Quartz	90.9
	Feldspar	0.1
	Clay	4.9
	Other	4.0

Table 11. Porosity measurements based on the large area fractions for non-permeated <75 mD and 175-300 mD samples

Sample	Porosity (%)
<75 mD	15.41
175-300 mD	23.12

The BSE large area maps for the <75 mD and 175-300 mD Berea sandstones (Figure 38) allow for some qualitative petrographic observations. For both permeabilities, grains range from sub-angular to sub-rounded, indicating moderate transport prior to deposition. The framework grains of both permeability ranges are primarily composed of quartz, with very minor amounts of feldspar also being present in the samples. Intergranular quartz cementation is also present, based on the lack of distinguishable grain boundaries between some of the lithic quartz grains, this can be observed from both BSE maps (denoted in the figure). Non-quartz cements can also be observed from the presence of minerals with a different BSE intensity that are binding some of the lithic quartz grains. From the overall mineralogical composition of the samples, these cements can be inferred to be primarily composed of illite, kaolinite, as well as minor inclusions of siderite and chlorite cement (Table 9 and 10). Some of the non-quartz cement on the large area maps can likely be identified as illite/kaolinite due to a similar or slightly lower BSE intensity (lower atomic mass density) compared to quartz, as well as the booklet-like morphology (denoted in the figure). Higher BSE

intensity (relative to quartz) pore-filling material can also be observed on the large area maps, due to the booklet-like morphology being present again, this can be assumed to be chlorite (denoted in the figure).

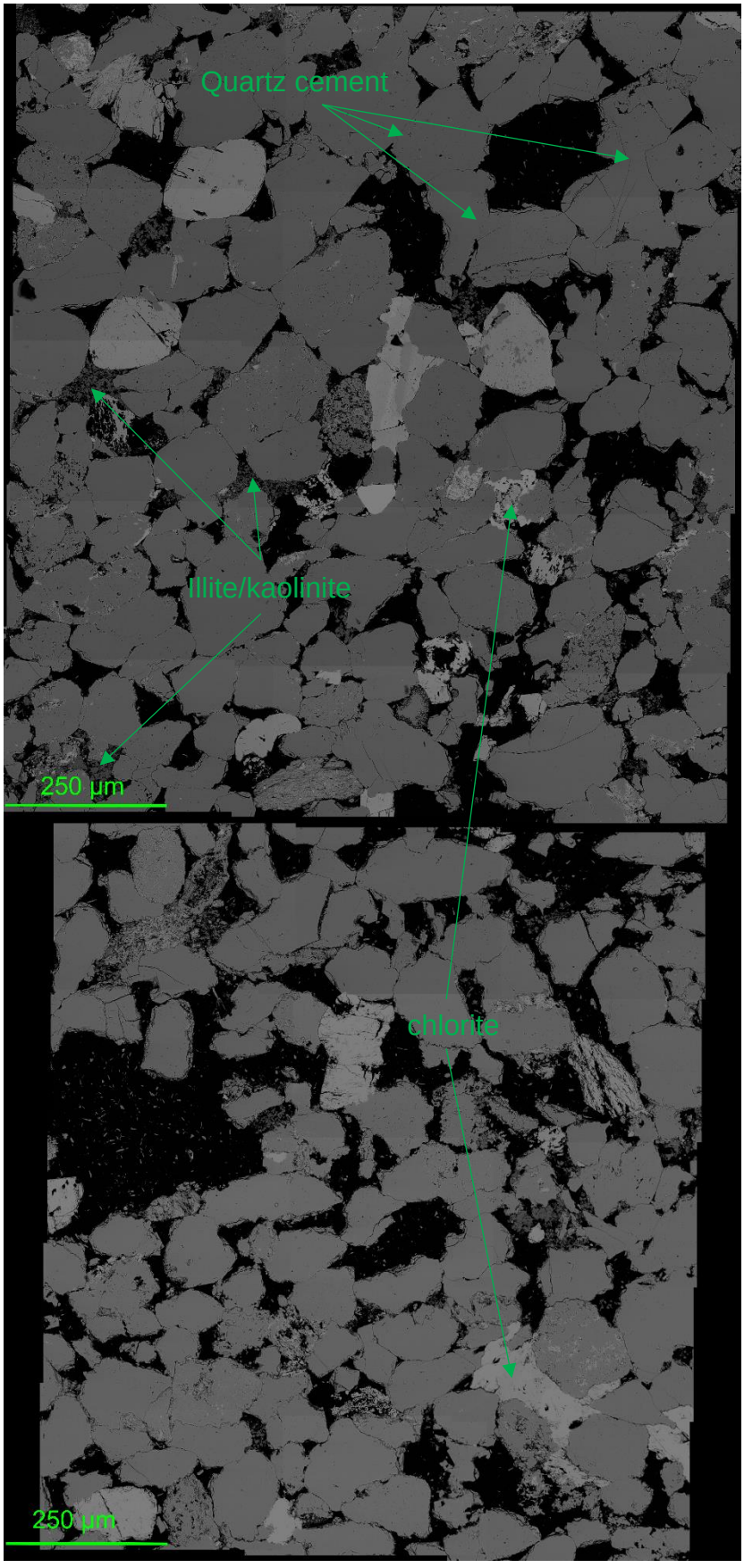

Figure 38. Montaged large area maps for non-permeated Berea sandstone thin sections. Top: <75 mD sample, bottom: 175-300 mD sample.

3.3 CT results

3.3.1 Problems with CT analysis

Several problems were encountered with the CT data. First, the bentonite gel was not able to be visualised within the CT images due to its low attenuation coefficient. As such, permeation depth, gel flow paths, and gel microstructures within the core were unable to analysed. The second issue that became apparent during data analysis is that the scans had a very low resolution. This created difficulties during segmentation as distinguishing pore space from the rock material (as well as the ability to distinguish between minerals), based on geometry via user observation using interactive thresholding, was made virtually impossible. This was due to the lack of prominent peaks in the grey-level histograms of the orthogonal slices of the core samples, resulting in difficulties in separating objects of interest (i.e., the pore space and the rock). Use of the auto-thresholding module, provided in Avizo, was also attempted to segment the pore space. In this module, a variety of algorithms are available (e.g., Otsu method), however, the different algorithms resulted in even more unrealistic results than the interactive thresholding. The last and the most severe issue encountered, was an artefact that resulted in uneven grey distribution throughout the sample, with top and bottom slices (through the XZ direction) and the area near the edge of the core (through the XY direction) having a lower attenuation value than the centre. This severely impacted the porosity analysis, as the altered the attenuation values of the top, bottom, and outer sections, created artificial pore space readings that were significantly greater than what could realistically be present in these regions. The artefact was initially observed when a single global threshold value was applied

to the control sample, which resulted in vastly different results for the top, middle and bottom sections (results in Table 12).

Table 12. Porosity, pore connectivity and mean pore volume values for control samples using a single global threshold value for the top, middle, and bottom.

Sample	Porosity (%)	Pore connectivity (%)	Mean pore volume (mm^3)
Control Core			
Top	16.22%	13.28%	0.05
Mid	23.25%	22.20%	0.12
Bottom	62.73%	62.71%	3.77

Several attempts were made to resolve the artefact. First, a *Beam hardening correction* module was applied to the data in Avizo, as the observed artefact was in essence the reverse of beam hardening phenomena. This, however, did not yield the desired result. Next, the application of different threshold values to each section of the core, as outlined in Section 2.7.2, was conducted. Unfortunately, it turned out that this deviation in attenuation values was not constant from sample to sample, and therefore unable to be fixed by applying the reference porosity-correlated threshold values of the control sample to scans of gel permeated cores. Due to time-constraints, further attempts at fixing the artefact had to be foregone and thus, the erroneous dataset had to be excluded from the discussion of the work at hand.

3.3.2 Porosity, pore connectivity, and mean pore volume results

The results of the porosity, pore connectivity, and mean pore volume analysis done in Avizo, are presented in Table 13. Visualisation of the porosity and pore connectivity in the control and gel permeated samples are shown in Figure 40.

Table 13. Porosity, pore connectivity and mean pore volume values for control, Batch I, and Batch II cores.

Sample	Porosity (%)	Pore connectivity (%)	Mean pore volume (mm^3)
Control Core			
Top	19.18%	17.62%	0.079
Middle	19.56%	17.9%	0.08
Bottom	19.98%	18.31%	0.075
Batch I Core			
Top	34.29%	33.49%	0.042
Middle	26.26%	25.93%	0.049
Bottom	7.73%	6.01%	0.005
Batch II core			
Top	55.86%	55.75%	1.86
Middle	63.96%	63.95%	9.17
Bottom	29.76%	29.2%	0.26

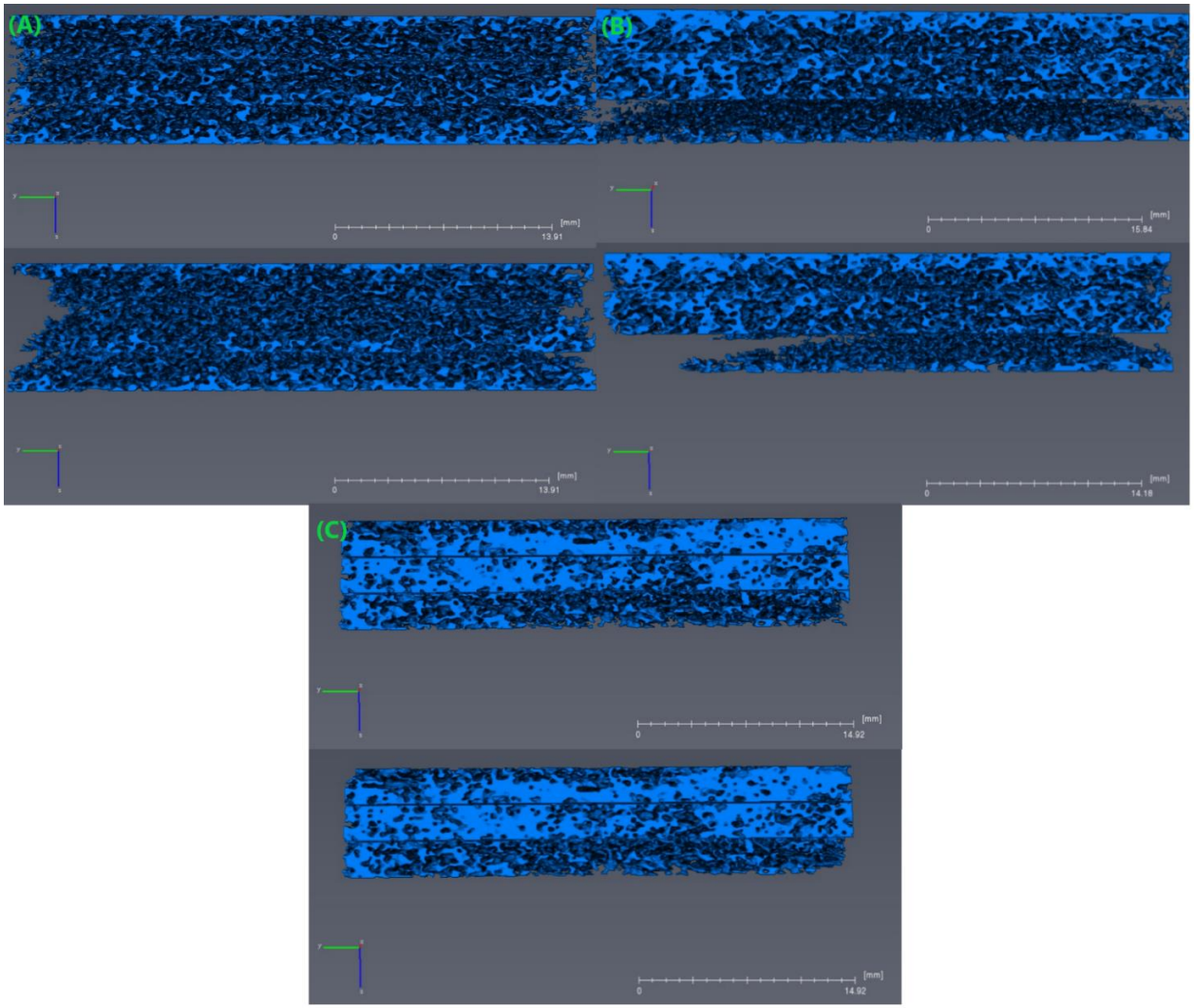

Figure 39. A. Top: porosity of non-permeated 175-300 mD core. Bottom: pore connectivity of non-permeated 175-300 mD core. B. Top: porosity of Batch I 175-300 mD core. Bottom: pore connectivity of Batch I 175-300 mD core. C. Top: porosity of Batch II 175-300 mD core. Bottom: pore connectivity of Batch II 175-300 mD core

3.4 Indentation results

3.4.1 Problems with indentation testing

Comparison of gel impregnated and non-impregnated samples of the same permeability operates under the assumption that both groups of cores possess the same baseline mechanical properties prior to permeation. In reality, Berea sandstone shows significant heterogeneity in mineral composition and structure, from sample to sample, even within the same permeability range (e.g., Kareem *et al.*, 2017). Structural variations between samples which significantly affect mechanical properties include microcracks, grain boundaries, lamination, and pores (Mokhtari and Tutuncu, 2016). As these natural variations were not determined prior to indentation, an assumption of homogeneity must be made to conduct comparison between samples.

A second shortcoming of the experimental method was that no imaging (e.g., digital or synchrotron) took place during or after indentation. Imaging is often conducted in unison with indentation testing to visually observe the mechanism of fracture initiation and propagation within the rock. Aside from qualitative information, indentation accompanied imaging also allow for the determination of crack length and shape, useful parameters that can be used to derive additional mechanical properties for the material (e.g., fracture toughness (Anstis *et al.*, 1981; Smith and Scattergood, 1992)). Due to the lack of imaging during or post indentation, interpretation of fracture mechanisms is done solely on the basis of force-displacement/stress-strain curves.

3.4.2 Introduction and context for the indentation results

This section comprises of the results for indentation testing of gel permeated Berea sandstone samples. As the rock mechanics analysis is entirely based on the force and

displacement data generated during indentation, the Section will begin by presenting the force-displacement curves for all samples (Figure 41, 42, and 43). Analysis of various material properties (ultimate strength, yield strength, Young's modulus, modulus of toughness, and fracture energy) as well as maximum displacement distance (an extensive physical property), derived from the force displacement curves, will then be introduced. The results for each of these properties will be presented in the same manner. First, the means and ranges of the respective property for each batch are stated. This is followed by determining statistical significance (via a paired two tailed T-test) between the mean values of the property between the batches as well as determining an average % change in the said property between the batches. After this, both inter-batch and intra-batch analysis of subgroups will take place, with the analysis consisting once again of means, ranges, statistical significance, and average % changes. Subgroups in this case consist of gel groups (consisting of the same concentration gel for each permeability) and permeability groups (consisting of gels of different concentration within the same permeability range). There are several things to note here. First, in determination of the mean and range of a physical property for each batch and subgroup, samples of a given permeability and/or gel concentration in one batch or subgroup without a matching sample in the batches or subgroups it is being compared to (henceforth referred to as 'odd' datapoints), are excluded. Likewise, when determining average percentage differences and statistical significance between batches or subgroups, odd datapoints were once again omitted. These odd datapoints (e.g., the three samples from Batch II without matching gel-permeability samples in Batch I), however, are still displayed on figures when data is presented. Next, average % change (which is the only % analysis conducted and may henceforth be simply referred to as % change) is determined by taking the average of

individual pairwise % changes between matching samples in batches or subgroups of interest. In the case of comparison between whole batches, an average % change would be determined by taking the average of individual % changes between samples of matching permeability and gel concentration between two batches. On the other hand, comparison between permeability groups within a batch would mean the average % change between the permeability groups is determined by taking the average of % changes between samples of matching gel concentration between the two permeability ranges. In the case of calculating % changes within or between groups containing control samples (Batch 0), of which repeats exist, the mean of the control samples of a given permeability were used in the % calculations. Lastly, it should be noted that in the case of subgroup analyses, due to the very small sample size of the subgroups (either $n=2$ or $n=3$), lack of repeats, and the aforementioned heterogeneity of Berea sandstone, nothing conclusive can be inferred between their relative differences. Therefore, numerical analysis between subgroups has only been conducted in cases where based on qualitative user determination, a potential emerging trend is identified. Subgroup analysis will not be included in the discussion section for the aforementioned reasons and should be considered as an example of the type of analysis that ought to be conducted with a meaningful number of repeats in the future.

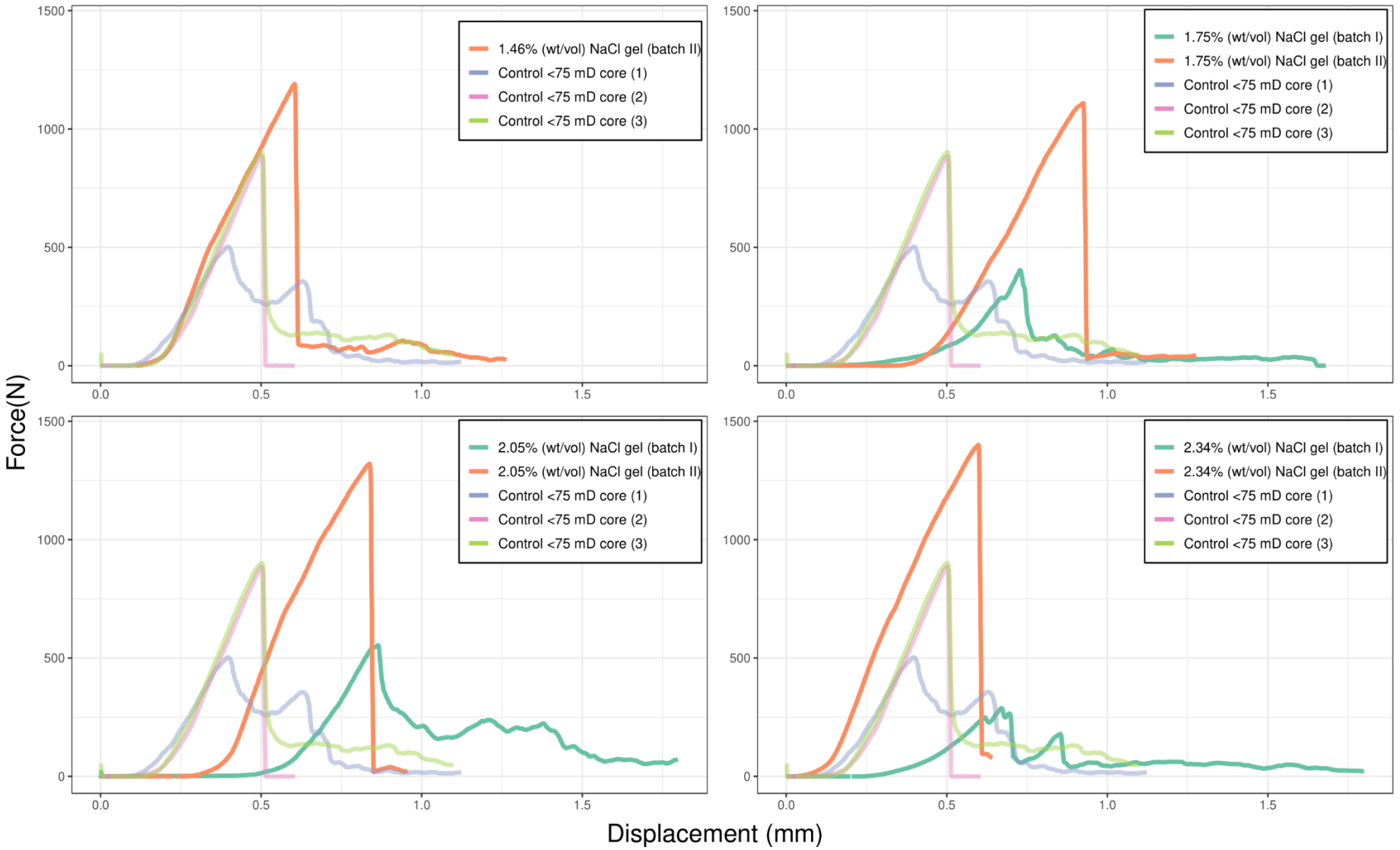

Figure 40. Force-displacement curves for <75 mD Berea sandstone cores, including control and bentonite gel permeated samples.

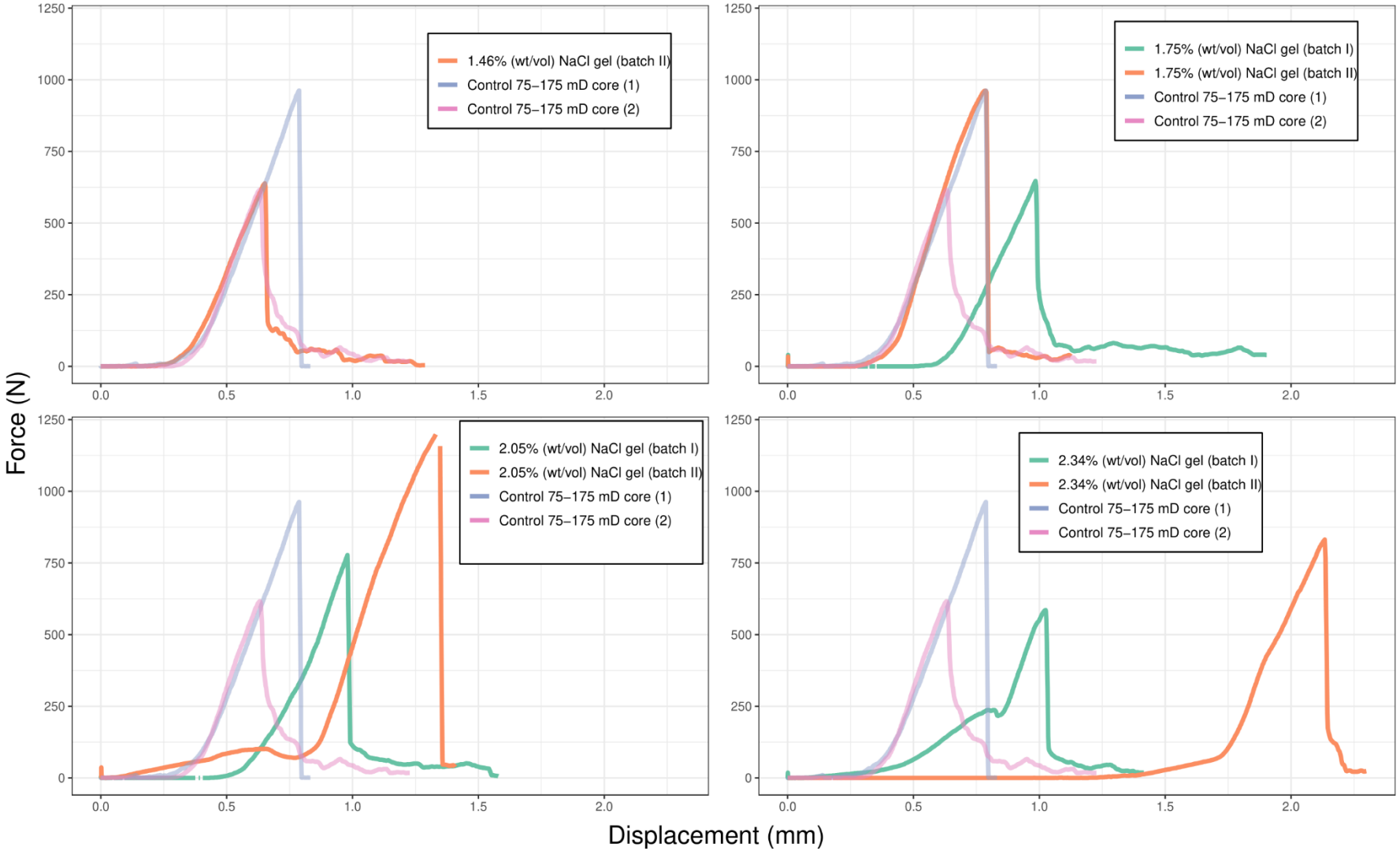

Figure 41. Force-displacement curves for 75-175 mD Berea sandstone cores, including control and bentonite gel permeated samples. Note that for 2.05% (wt/vol) NaCl gel (Batch II), an erroneous datapoint (displaying a near zero force value) was removed

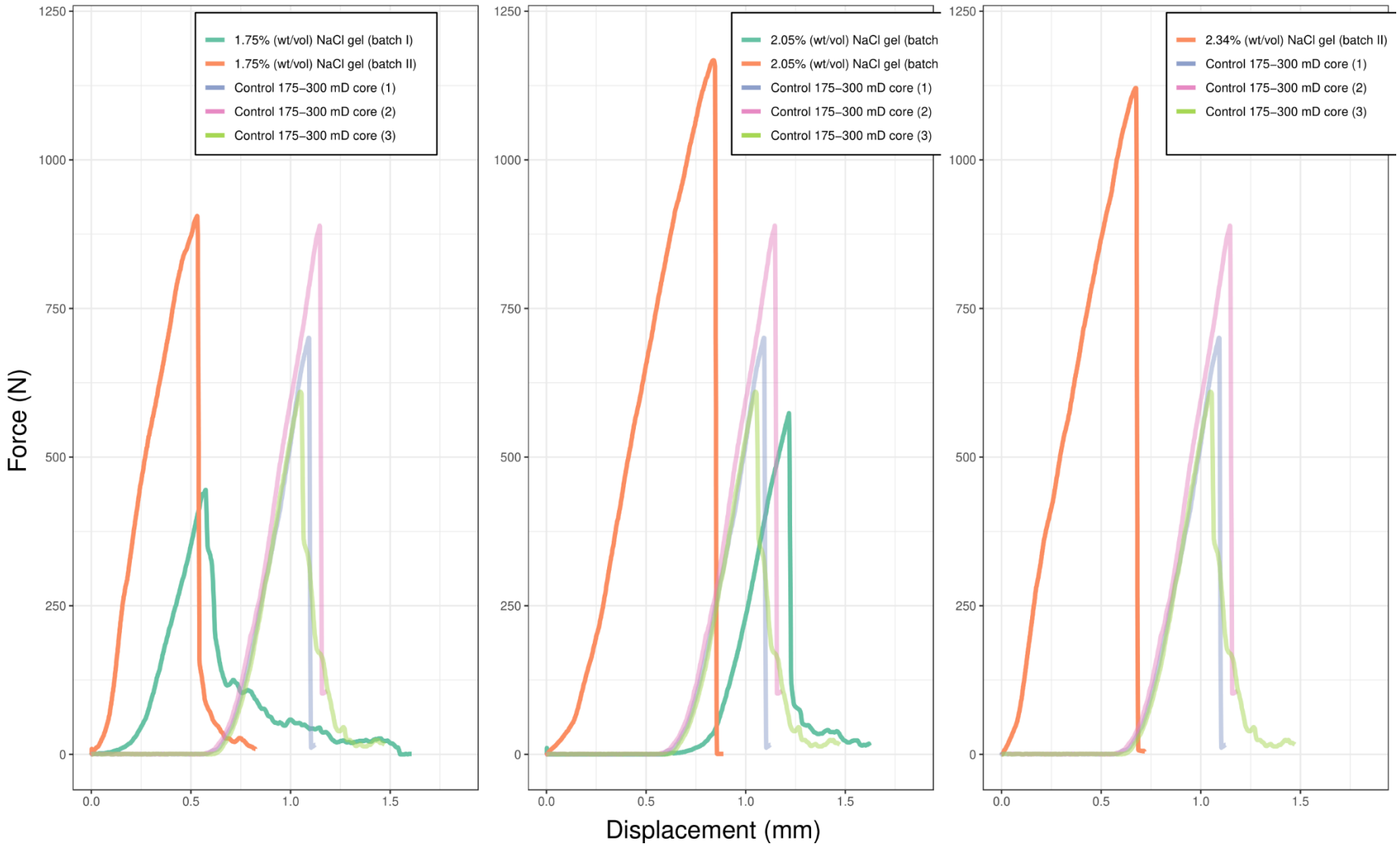

Figure 42. Force-displacement curves for 175-300 mD Berea sandstone cores, including control and bentonite gel permeated samples.

3.4.3 Mechanical and extrinsic physical properties of the indented sandstones

A set of initial qualitative observations can be carried out based on Figure 41 to 43. All batch II samples displayed a higher peak force value than in Batch I samples, and the majority of Batch I samples (with the exception of the 2.34% NaCl (wt/vol) gels in 75-175 mD cores) had a greater displacement distance. A large degree of variability can also be observed between the peak force of control samples of the same permeability range, demonstrating the significant heterogeneity present in the sandstones. There is also variance in the strain response (i.e., the shape of the lines on the figures) of the core samples (discussed in greater depth in section 4.3.3), including both within batches (including the control batch) and between them. Control samples exhibit the least plastic behaviour (little to no change in angle pre-post peak), and Batch I and II samples range from displaying almost no plastic deformation to significant plastic deformation. Differences in strain can also be observed in the post peak force region in regard to its angle, with the majority of Batch II and control samples having brittle post peak behaviour (i.e., the post-peak angle is close to 90°), and Batch I samples showing post-peak softening (<90°).

Ultimate strength

Ultimate strength results are presented in Figure 44. The average strength of Batch I samples was 170.17 MPa (range, 91.71 – 247.42 MPa), Batch II samples had a strength of 354.54 MPa (range, 264.76 – 445.63 MPa), and control samples averaged at 241.47 MPa (range, 160.16 – 306.42). Inter-batch comparison revealed a statistically significant difference between the means in strength in Batch I and Batch II (p=0.0006, n=16), with the mean percentage increase from Batch I to II being

131.50%. A statistically significant difference in the means was also observed between the control batch and Batch II (p=0.006, n=16). Similarly, ultimate strength was found to increase from the control batch to Batch II, with an average % increase of 40.23%. Comparing the strength of the control cores to the dry gel batch showed that the batches were significantly different (p=0.038, n=16), and that the non-permeated cores had a 30.37% higher ultimate strength relative to cores containing dry gel.

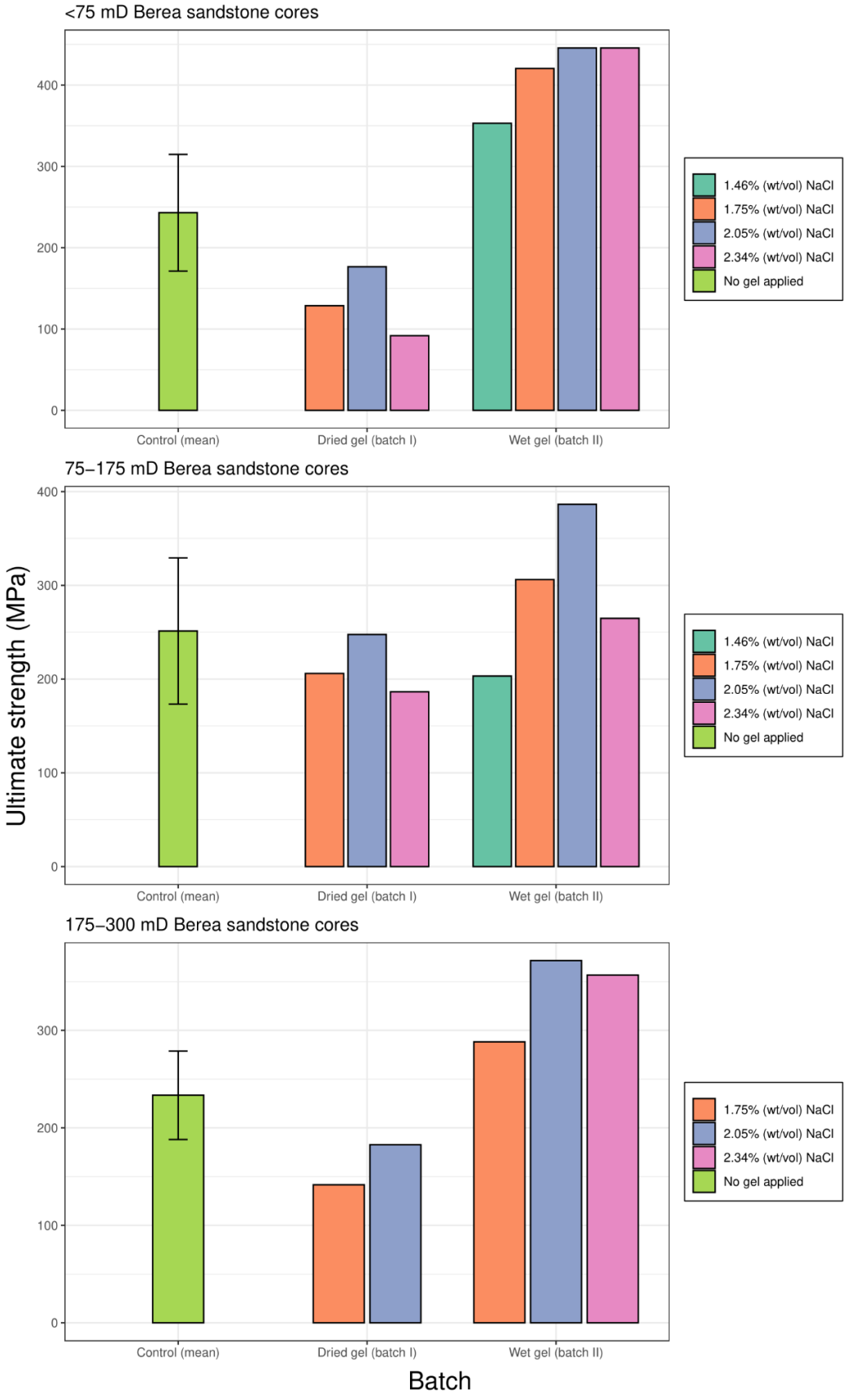

Figure 43. Ultimate strength results for indented core samples. Error bars on control samples denote standard deviation (based on three samples for <75 mD cores, two samples for 75-175 mD cores, and three samples for 175-300 mD cores).

Intra- and inter-batch analysis of peak force between gel and permeability groups is summarised in Figure 45.

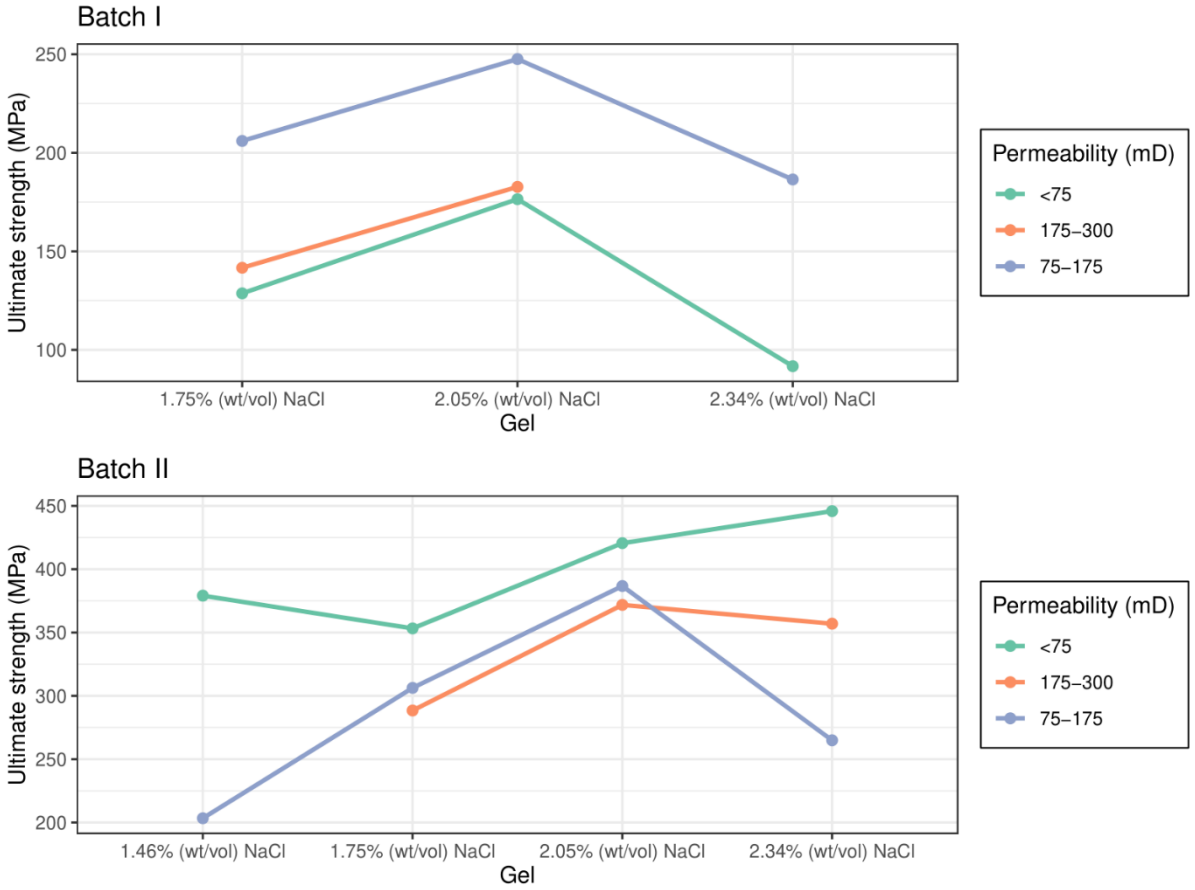

Figure 44. Ultimate strength values of gel permeated samples in relation to the NaCl concentration of the gel and the initial permeability of the cores.

From the first graph (Batch I) within Figure 45, it can be observed that there is on average, a ~43 MPa increase, or a 28.77% average % increase, in ultimate strength from 1.75% (wt/vol) NaCl gel to 2.05% (wt/vol) gel in all permeability ranges with a statistically significant difference of the mean strengths between the gel groups (p=0.0025, n=6). This is followed by a relatively steeper drop of ~73 MPa, or a 36.35% average % decrease, from 2.05% to 2.34% gel in <75 and 75-175 mD cores, with the means between the two groups once again being statistically significant (p=0.1, n=4). In Batch II, the only visually observable trend was an increase in ultimate strength from

1.75% to 2.05% gel across permeability ranges, with an average % increase of 24.74%, which is of a similar magnitude to the increase in strength from 1.75% to 2.05% gels in Batch I. Comparison between all other gel groups in Batch II, however, displayed no observable trends. Comparison of ultimate strength between the permeability groups in Batch I showed that the 75-175 mD group showed a significantly higher average peak force value (213.35 MPa) than that of <75 mD cores (132.30 MPa), with an average % increase of 67.89% from <75 mD to 75-175 mD.

Comparison of the gel groups between batches shows that, on average, there is a 99% increase in ultimate strength from 1.75% (wt/vol) NaCl gels from Batch I to Batch II, a 94% increase in 2.05% gels and a 155% increase in ultimate strength in 2.34% gels from Batch I to II. Ultimate strength between permeability groups between the different batches shows a 232.81% average increase in strength from Batch I <75 mD cores to Batch II <75 mD cores, an average increase of 48.89% from Batch I to Batch II 75-175 mD cores, and a 103.4% mean increase from Batch I to Batch II 175-300 mD cores. This reaffirms the observation of increasing ultimate strength from Batch I to II, however, no systematic change in peak force between gel and permeability groups between the Batches is observed.

Displacement distance

Displacement distances of the cores are shown in Figure 46. Analysis of the maximum displacement distance of each batch gives an average distance of 1.78 mm (range, 1.42 – 2.61 mm) for Batch I, 1.18 mm (range, 0.64 – 2.35 mm) for Batch II, and 1.08 mm (0.61 – 1.48 mm) for the control group. An average % decrease of 29.02% was observed in the maximum displacement distance from Batch I to Batch II samples,

however, the means of the displacement values between the two groups showed an insignificant difference (p=0.063, n=16). Another, albeit much more, insignificant difference in means was observed between the control batch and Batch II (p=0.64, n=16). The mean % change from the control batch to Batch II showed an 11.9% increase in displacement distance. Lastly, a large mean percentage increase of 72.69% was observed from control to Batch I cores, with a significant difference in the means of the displacement values (p=0.013, n=16).

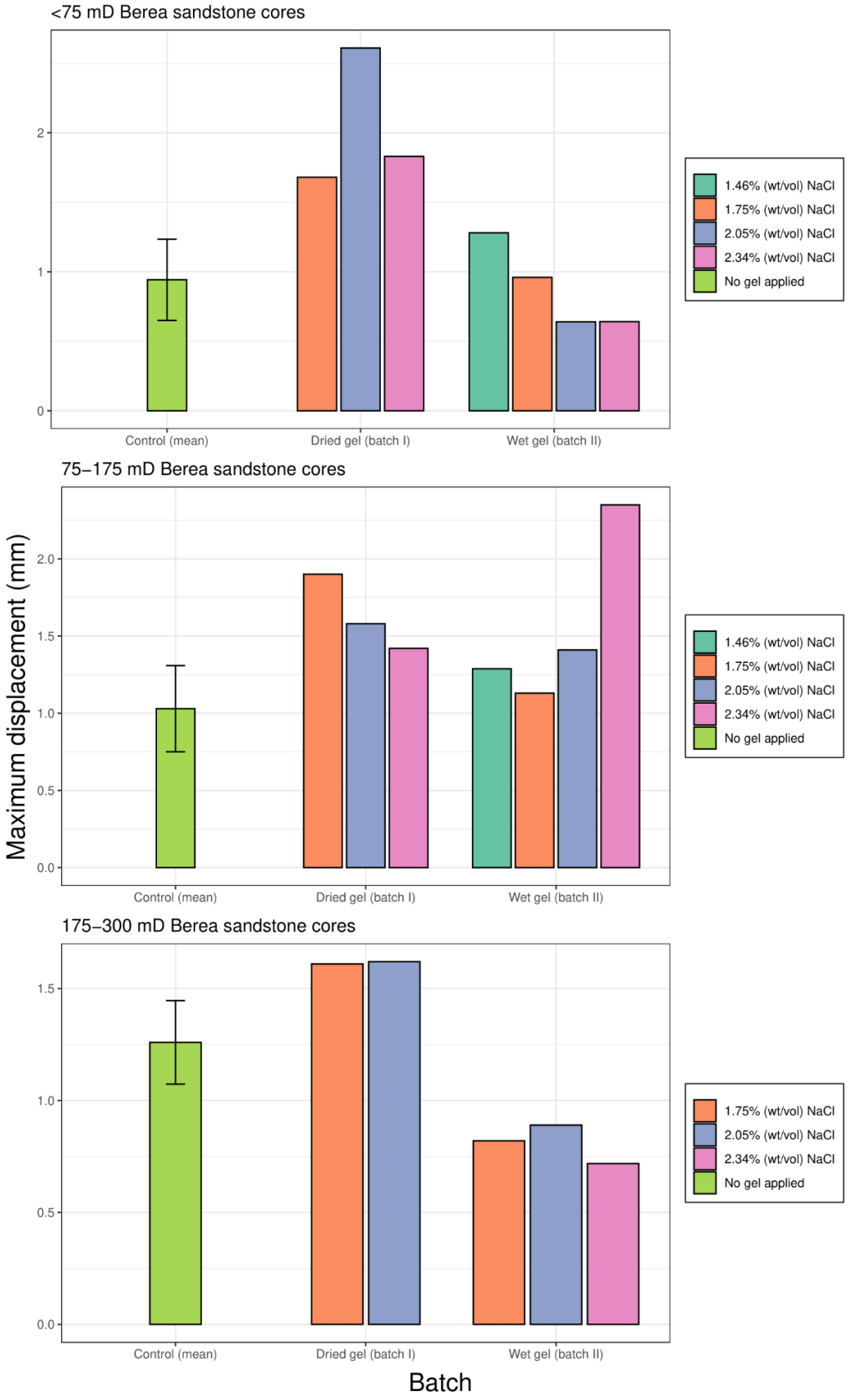

Figure 45. Maximum displacement results for indented core samples. Error bars on control samples denote standard deviation (based on three samples for <75 mD cores, two samples for 75-175 mD cores, and three samples for 175-300 mD cores).

Intra-batch displacement analysis (Figure 47) was performed in the same manner as for the peak force. However, no distinguishable trends between the gel and permeability groups in their respective batches were observed.

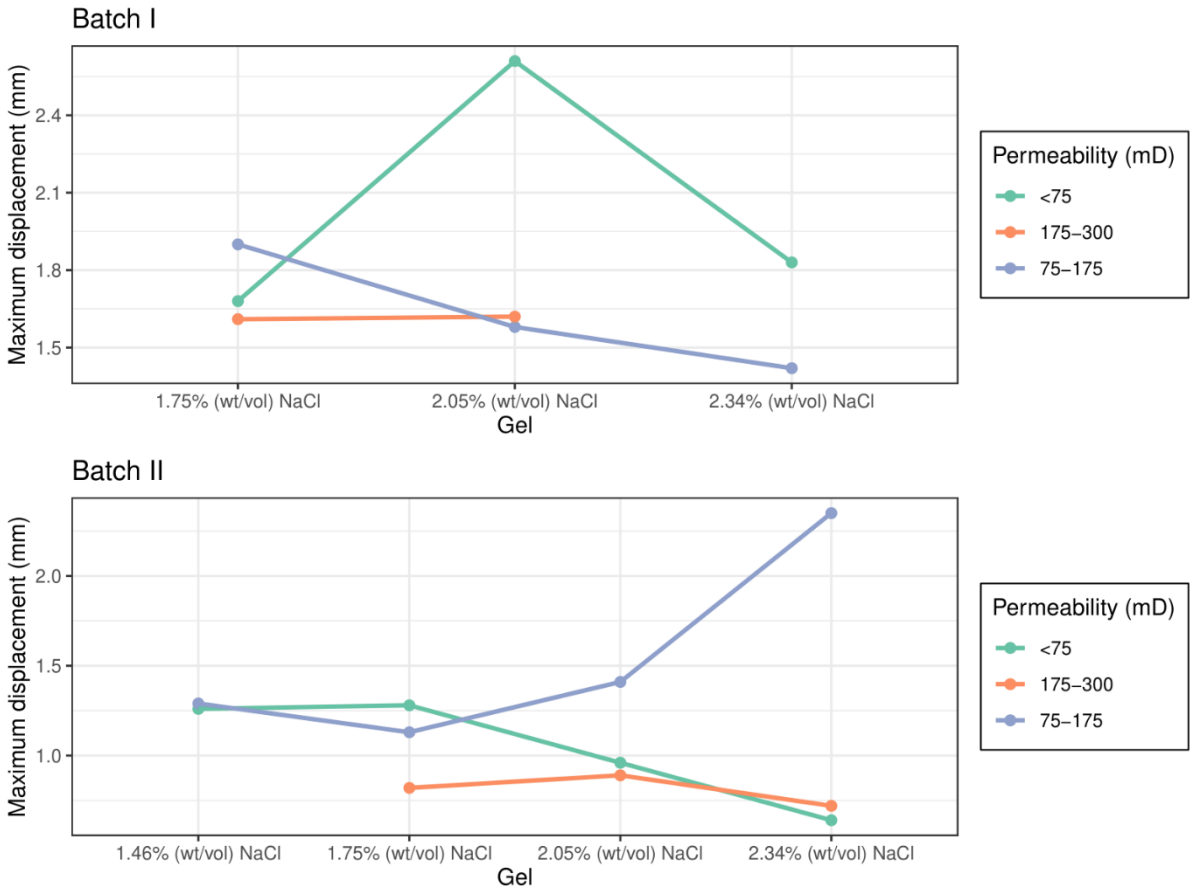

Figure 46. Maximum displacement distance values of gel permeated samples in relation to the NaCl concentration of the gel and the initial permeability of the cores.

Looking at average % change in displacement distance between gel groups in the two batches, an average % decrease of 37.87% in displacement length in 1.75% gels from Batch I to II, an average % decrease of 39.84% in 2.05% gels, and an average % increase of 0.46% for 2.34% gels from Batch I to II was reported. Comparing displacement distance between the permeability groups in the two batches reported differences in displacement distance correspond to an average % decrease of 50.79% from the <75 mD group in Batch I to II, a 4.75% increase between 75-175 mD groups

and another average decrease of 47.03% from the 175-300 mD group in Batch I to Batch II. From these average percentage change values of matching gel and permeability groups between samples, no trends are able to be readily identified.

Yield strength

Yield strength (Figure 48) analysis reports an average yield strength of 105.58 MPa (range, 67.11 – 164.76 MPa) for Batch I samples, a yield strength of 199 MPa (range, 84.08 – 292.23 MPa) for Batch II, and lastly a mean yield strength of 232.17 MPa (range, 140.3 – 288.05 MPa) for the control samples. Comparison between batches shows a statistically significant difference between Batch I and II yield strength values (p=0.0108, n=16), with an average % increase of 108.93% in yield strength from Batch I to II. Between the control samples and Batch II, no significant difference in their yield strength (p=0.32, n=16) was observed, and a small average % decrease of 14.95% from control to Batch II samples was reported. The most significant difference between yield force values was found to be between the control batch and Batch I (p=0.00067, n=16), with a large mean % decrease of 54.55% in yield strength from control to Batch I.

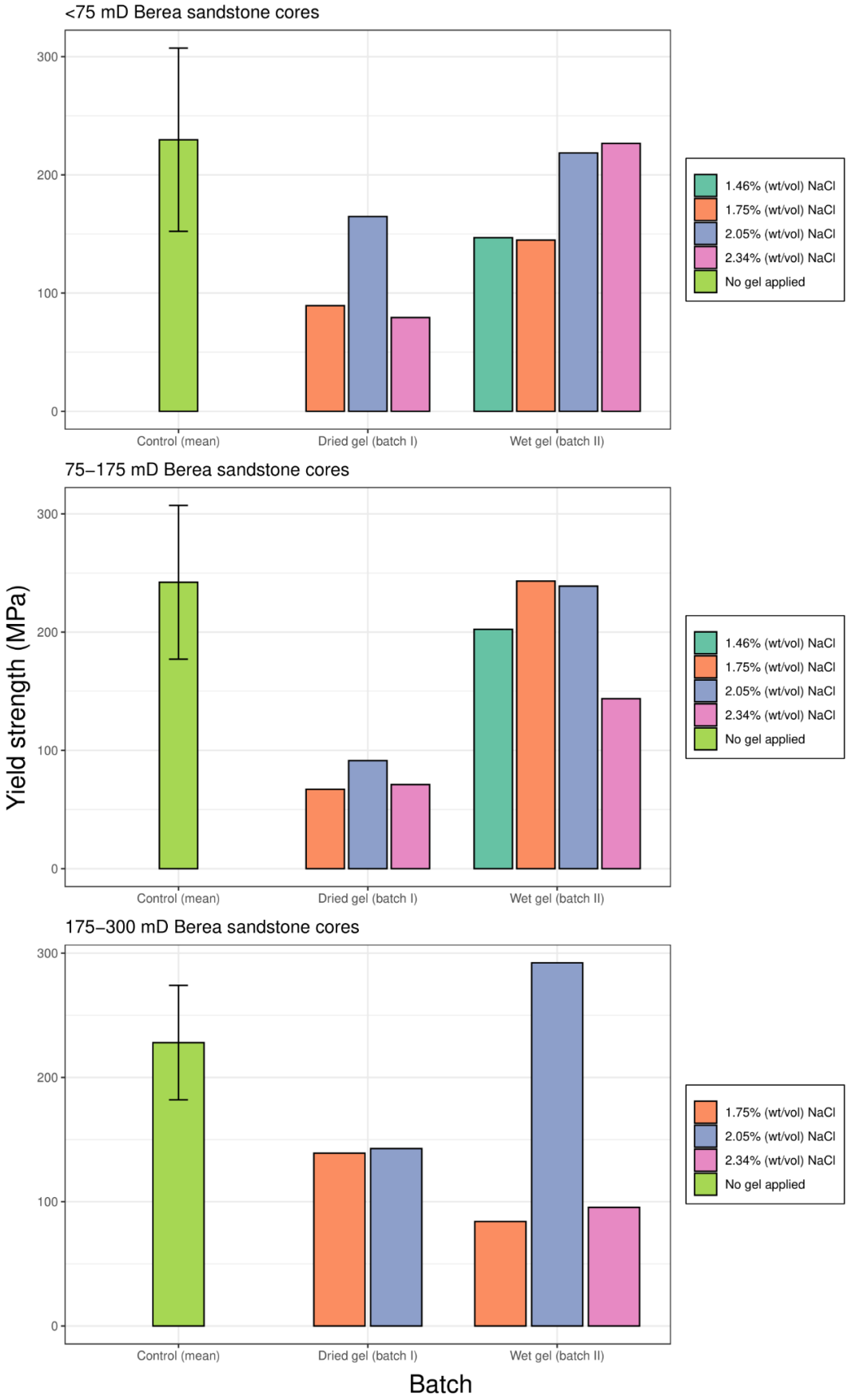

Figure 47. Yield strength results for the indented core samples. Error bars on control samples denote standard deviation (based on three samples for <75 mD cores, two samples for 75-175 mD cores, and three samples for 175-300 mD cores).

Permeability and gel group analysis of the yield strength values is presented below (Figure 49).

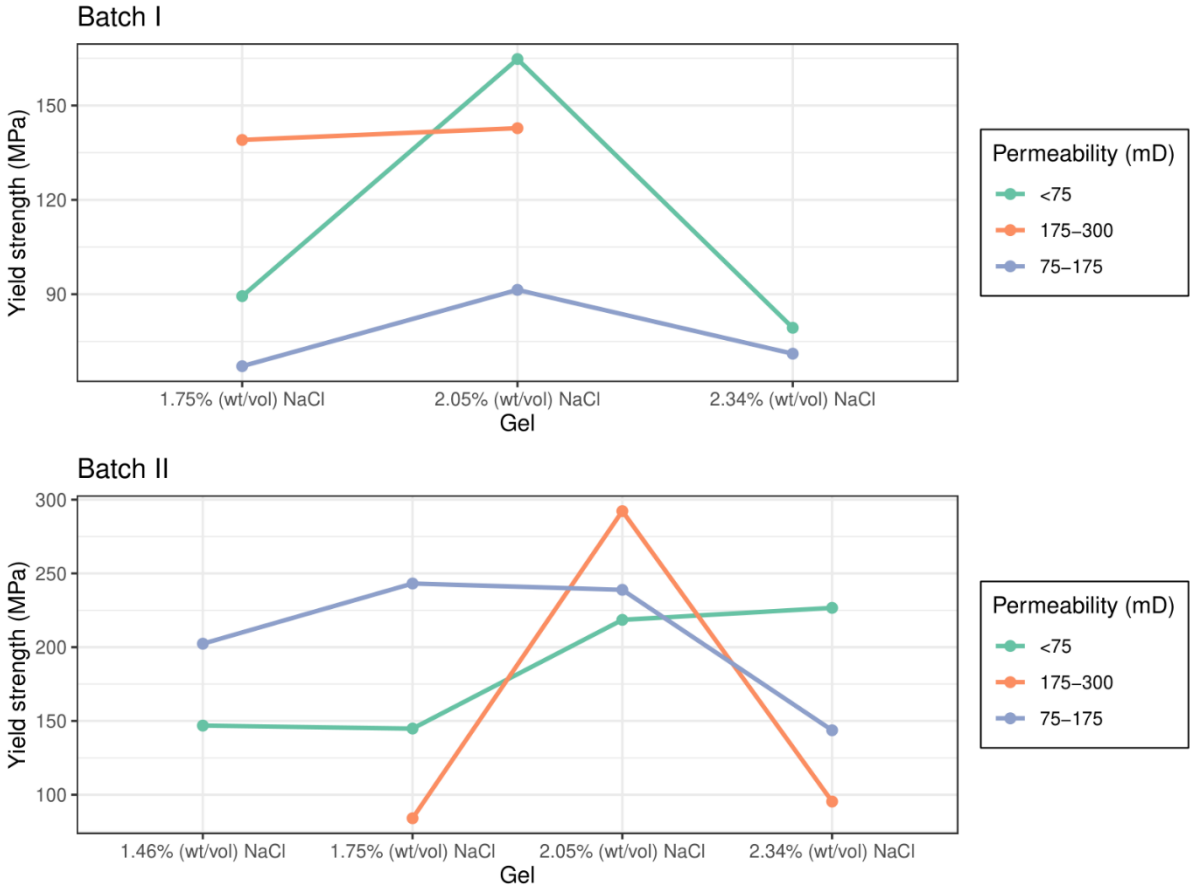

Figure 48. Yield strength values of gel permeated samples in relation to the NaCl concentration of the gel and the initial permeability of the cores.

In Batch I, it can be observed that there is an increase, albeit to varying degrees, in yield strength from all 1.75% (wt/vol) NaCl gels (mean yield force of 98.51 MPa) to 2.05% gels (132.97 MPa) with an average % increase of 41.06%. This is then followed by a trend of decrease in yield strength from 2.05% gels to 2.34% gels (75.2 MPa) with an average % decrease of 37.03%. This trend of increase in Batch I from 1.75% gels to 2.05% gels, followed by a decrease from 2.05% to 2.34% is reminiscent of changes in ultimate strength of the same samples. However, when comparing between permeabilities, the inverse trend of ultimate strength is observed, with the

<75 mD group showing a larger yield strength in all samples when compared to the 75-175 mD group, with the average % change from <75 mD to 75-175 mD being -26.6%. No trends could be identified between gel or permeability groups within Batch II.

Comparison of matching gel and permeability groups between batches shows an overall increase in yield strength from Batch I to II, but no trends were identified between average % changes between the individual groups.

Young's modulus

Young's modulus results are presented in Figure 50. Batch I had an average E of 2.98 GPa (range, 1.22 – 3.85 GPa), Batch II showed an average E value of 5.56 GPa (range, 3.84 – 7.30 GPa), and lastly the control batch displayed an average E of 4.54 GPa (range, 3.61 – 6.55 GPa). Comparing the batches reveals that Young's modulus differs significantly between Batch I and Batch II (p=0.0015, n=16), and a large average % increase of 114.1% in E from Batch I to Batch II is observed. Between the control group and Batch I, a significant variation in the means is once again observed (p=0.0032, n=16), with E showing a mean % decrease of 34.43% from control to Batch I. Means of the control and Batch II differ significantly (p=0.0087, n=16). From control to Batch II, the average % increase was 23.76%.

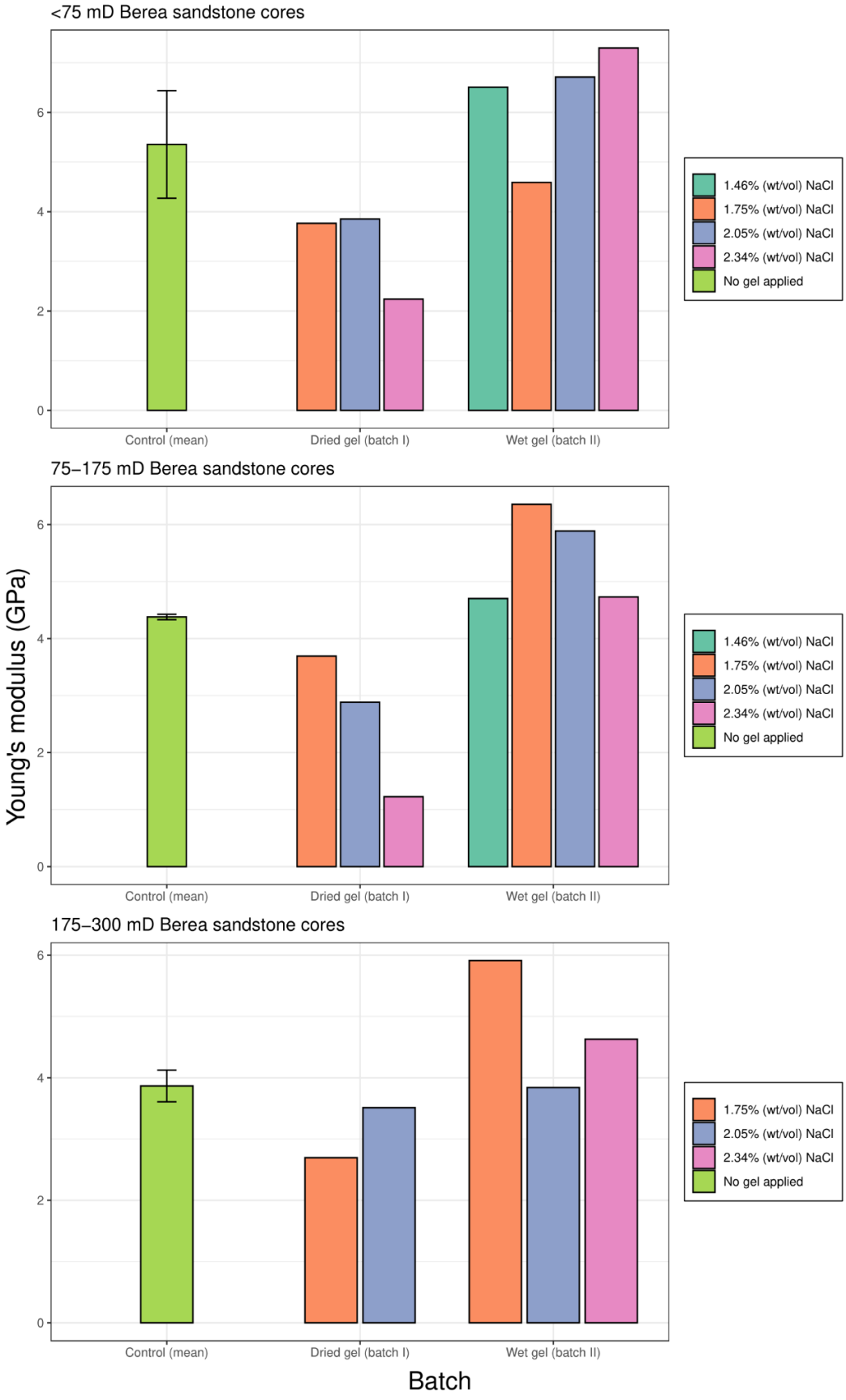

Figure 49. Young's modulus results for the indented core samples. Error bars on control samples denote standard deviation (based on three samples for <75 mD cores, two samples for 75-175 mD cores, and three samples for 175-300 mD cores).

Inter- and intra-batch comparisons are presented in Figure 51.

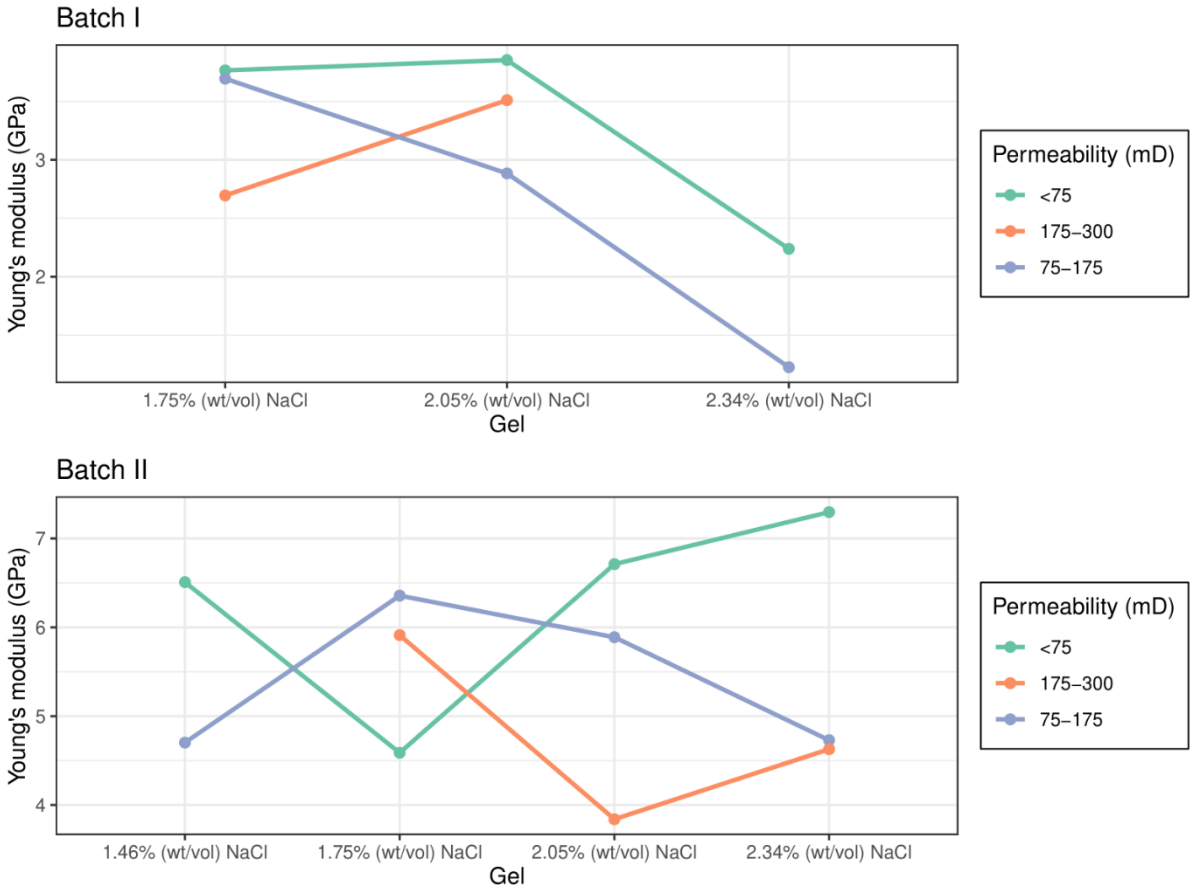

Figure 50. Young's modulus values of gel permeated samples in relation to the NaCl concentration of the gel and the initial permeability of the cores.

Some trends have been able to be identified for Young's modulus during intra-batch comparison of gels and permeabilites. First, there is a decrease in E from 2.05% gels to 2.34% gels in Batch I, with an average % decrease of 49.69% in Young's modulus. Secondly, it was observed that when comparing permeabilities in Batch I, all <75 mD permeability datapoints were greater than those of 75-175 mD, with an average % decrease of 24.083% in Young's modulus from the <75 mD to 75-175 mD permeability group. Comparison of matching permeability and gel groups between the batches once again shows an overall increase in Young's modulus from Batch I to Batch II with

a seemingly random spread of percentage increases between the matching permeabilities and gels from the first to the second batch.

Modulus of toughness

Modulus of toughness results for individual samples are show in Figure 52. For Batch I, the mean modulus of toughness value was 4.45 N/mm^2 (range, 1.53 – 6.67 N/mm^2), in the case of Batch II, the mean was 15 N/mm^2 (range, 9.5 – 22.02 N/mm^2). Lastly, the control batch displayed a toughness modulus mean of 6.45 N/mm^2 (range, 3.18 – 9.75 N/mm^2). Determining whether there was a statistically significant difference between the means of toughness moduli values between the batches shows a significant change between Batch I and II (p=0.00065, n=16), a statistically insignificant difference between Batch 0 and I (p=0.10, n=16), and another significant difference between the control and Batch II means (p=0.0054, n=16). Comparing the mean % change in modulus of toughness between batches gives a 328.63% increase from Batch I to II, a 32.16% decrease from Batch 0 to Batch I, and another large mean percentage increase of 137.16% from control to Batch II.

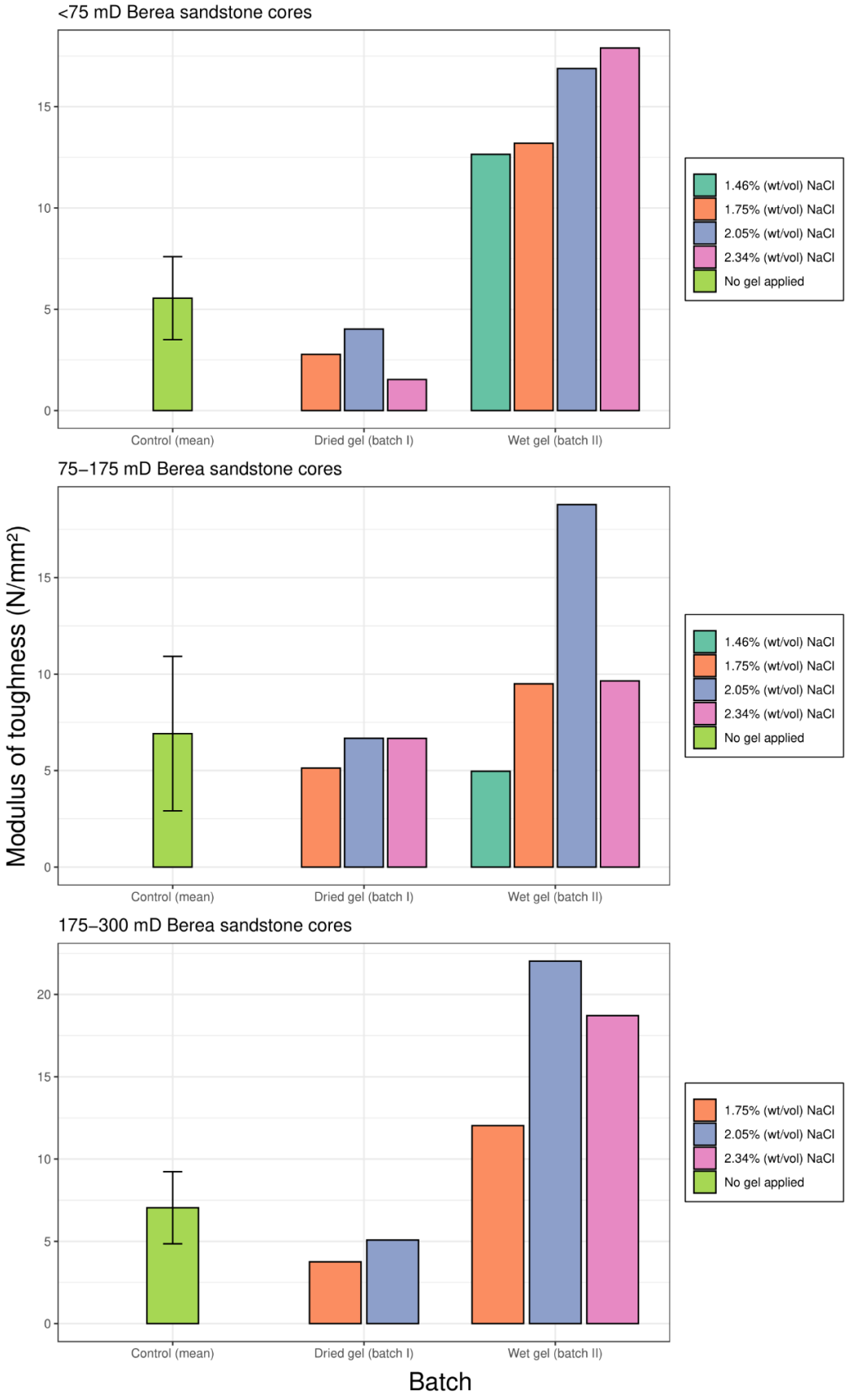

Figure 51. Modulus of toughness results for the indented core samples. Error bars on control samples denote standard deviation (based on three samples for <75 mD cores, two samples for 75-175 mD cores, and three samples for 175-300 mD cores).

Analysis of toughness moduli between permeability and gel groups is shown in Figure 53.

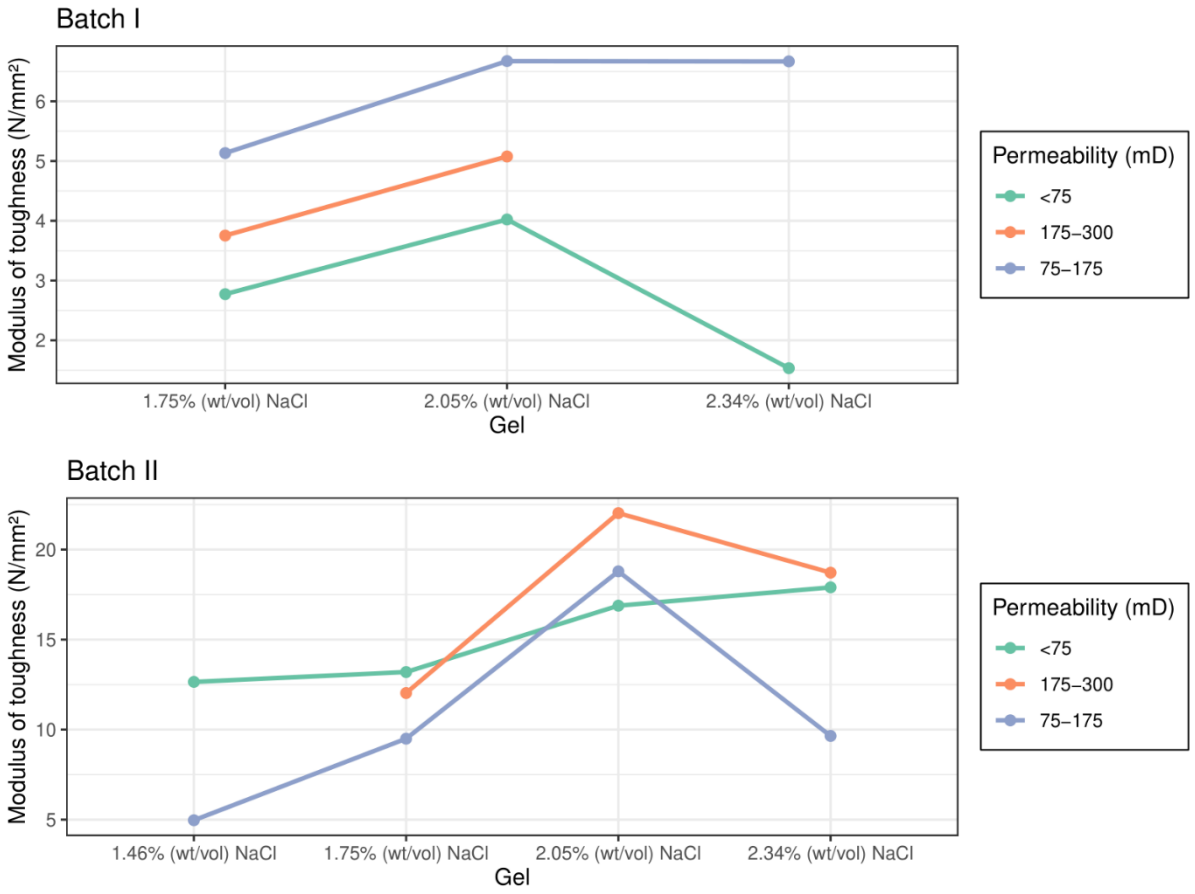

Figure 52. Modulus of toughness values of gel permeated samples in relation to the NaCl concentration of the gel and the initial permeability of the cores.

Intra-batch analysis of Batch I samples shows a roughly equal increase in the toughness modulus from all 1.75% to 2.05% gel samples, with an average % increase of 36.78%. Comparison of the mean modulus of toughness values between the two gel groups gives a statistically significant difference (p=0.00399, n=6). From comparing permeability groups within Batch I, it can be seen that there is a trend of mean toughness modulus values increasing roughly evenly from <75 mD (2.78 N/mm^2) to 175-300 mD (4.42 N/mm^2) to 75-175 mD (6.16 N/mm^2). The corresponding mean % increases between the permeabilities were found to be 30.79% from the <75

to 175-300 mD permeability group, and 25.40% from the 175-300 mD to 75-175 mD permeability group. Observation of gel groups in Batch II shows toughness modulus increasing, across all samples, from the 1.46% (wt/vol) NaCl gel group to the 1.75% group, with an average % increase of 47.78%. This is followed by a second increase from all 1.75% samples to 2.05% samples, showing a 69.61% average % increase.

Fracture energy

Fracture energy results for all samples are displayed in Figure 54. The mean fracture energy for Batch I was 3.54 N/mm^2 (range, 1.26 – 9.61 N/mm^2), Batch II was 1.12 N/mm^2 (range, 0.73 – 1.51 N/mm^2), and the control batch had an average fracture energy of 2.14 N/mm^2 (range, 0.46 – 5.35 N/mm^2). T tests between the fracture energy results of the batches showed a statistically significant difference between Batch I and II (p=0.029, n=16), and an insignificant difference in the means between Batch 0 and I (p=0.32, n=16) and Batch 0 and II (p=0.17, n=16). Average % changes in fracture energy between batches displayed a decrease of 57.99% from Batch I to Batch II, an increase of 65.24% from control to batch I, and another decrease of 42.3% from control to Batch II.

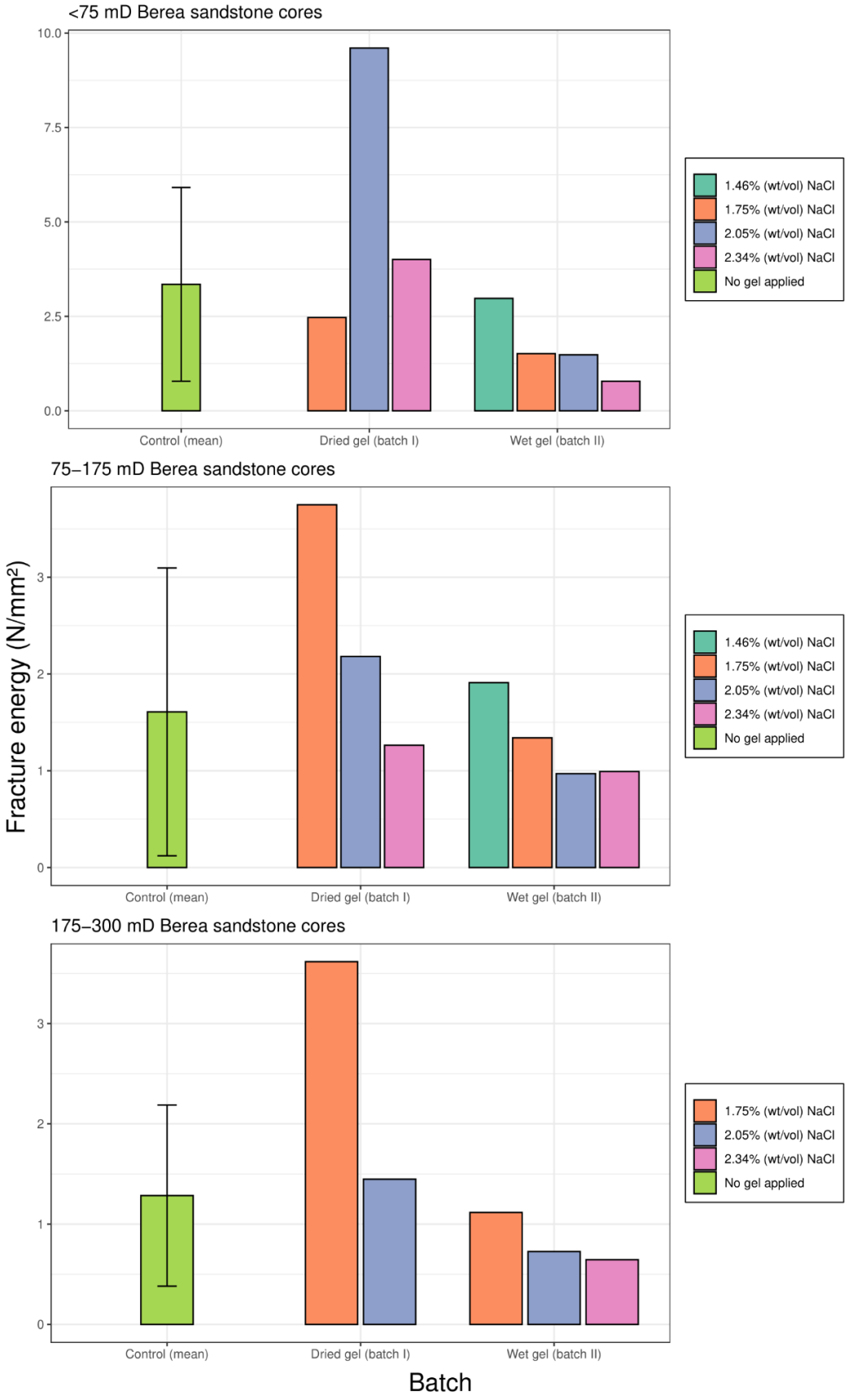

Figure 53. Fracture energy results for indented core samples. Error bars on control samples denote standard deviation (based on three samples for <75 mD cores, two samples for 75-175 mD cores, and three samples for 175-300 mD cores).

Subgroup analysis results are presented in Figure 55.

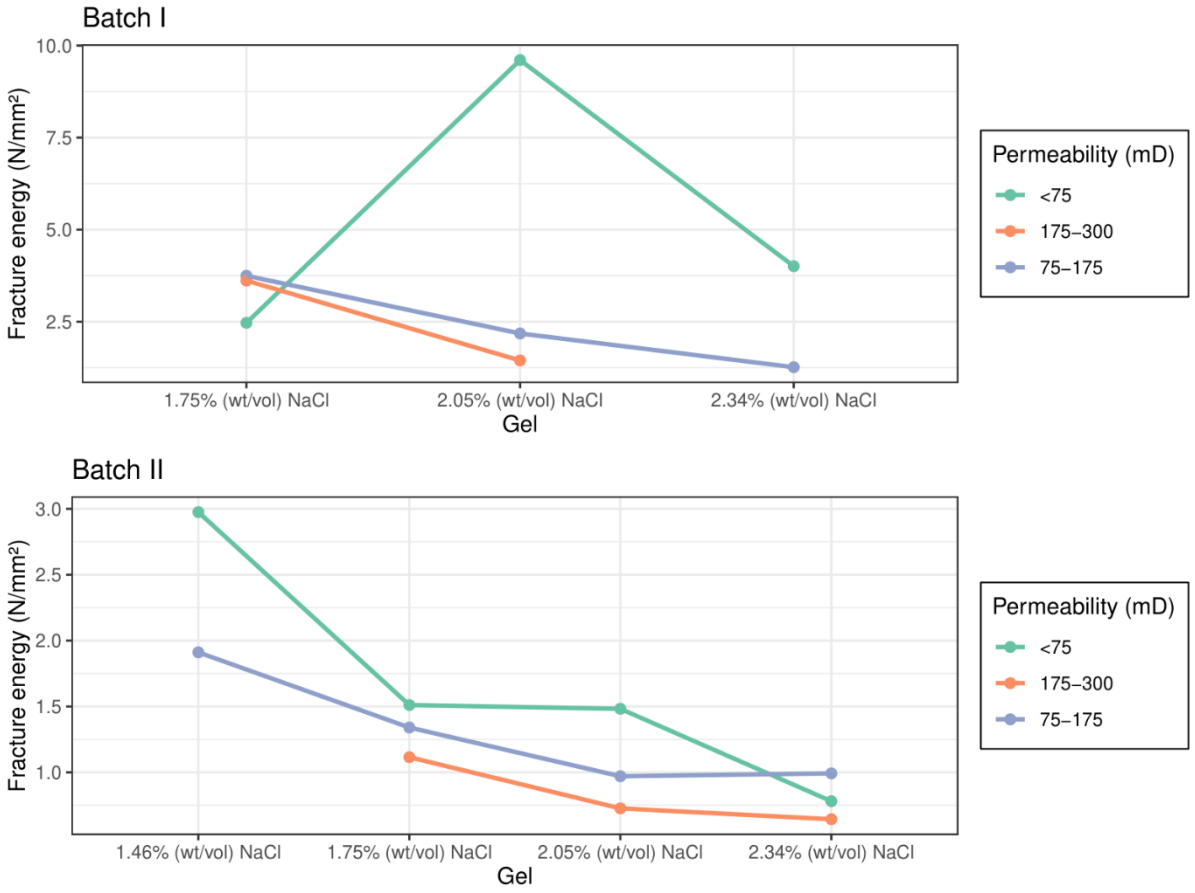

Figure 54. Fracture energy of gel permeated samples in relation to the NaCl concentration of the gel and the initial permeability of the cores.

Intra-batch comparison of gel groups in batch two shows a decrease in fracture energy with increasing NaCl concentration. An average % decrease of 39.53% was reported from 1.46% (wt/vol) NaCl gel to 1.75% gel samples, a 21.44% decrease was observed from 1.75% to 2.05% samples, followed by a 22.54% decrease from 2.05% to 2.34% samples. There is also an apparent trend between permeability groups in Batch II, with <75 mD group showing the highest mean fracture energy, followed by the 75-175 mD group, and lastly, the 175-300 mD group with the lowest mean fracture energy.

4. Discussion

4.1 Novel apparatus

4.1.1 Comparison between the novel press and commercially available alternatives

Commercially available counterparts to the novel press presented in this study are conventional and modified (Permeability Plugging Tester (PPT)) HTHP presses[1]. While producers and models vary, an example of the specifications and methods of operation for a generic HTHP and PPT press are provided in OFITE, 2019a and OFITE, 2019b, respectively. The novel press designed here has several advantages and disadvantages when compared to these alternatives.

A major upside of the novel kit is its low weight, size, and small manufacturing cost compared to the alternatives. To the author's knowledge, the smallest commercially available HTHP presses have a capacity of 175 ml. Comparing the novel press to commercial 175 ml HTHP presses manufactured by OFITE and Fann (the two biggest providers of oilfield testing equipment), the novel piece of kit is 0.45× the mass, 0.20× the height, and 0.31× the width of its industry counterparts (using mean weight and dimensons of the OFITE and Fann press[2]). Furthermore, the OFITE and Fann filter presses have to be pressurised through the use of either carbon dioxide or nitrogen gas bulbs, whereas the pressure inside the novel kit can be increased mechanically. These attributes combined with the fact that the apparatus requires no electricity, make it a potentially viable option (subject to further testing to verify the depth of gel

[1] Commercially available low temperature low pressure presses are only able to accommodate filter paper as the filtering medium as opposed to core samples and are therefore not considered in this comparison.

[2] Specifications of the OFITE press found in OFITE, 2019a. The Fann press weight and dimensions (14.52 kg, 33 cm × 33 cm × 58.42 cm) were obtained from personal communications with Fann Instrument Company.

permeation) for filtration characteristics and rock permeation analysis under fieldwork conditions.

Some drawbacks, however, have also become apparent in the use of the apparatus over the course of this study. Core fracturing during permeation occurred over a wide, seemingly random, range of torque values. This may be due to the natural heterogeneity of the sandstone samples, due to a pressure imbalance within the apparatus, or the gel (when it has force applied to it) initiating and/or propagating fractures within the rock. Another limitation of the press is that the amount of pressure it is possible to apply is limited by user strength. Although it should be noted that in the case of sandstone, it was found that to reliably permeate the core without fracturing, torque needed to be kept at <5 N m^{-1} (meaning that at this relatively low torque, user strength was not a limiting factor). The risk of fracturing posed another problem in that the speed of permeation is not able to be controlled as a variable as a low torque had to be maintained, this also resulted in permeation taking a significant amount of time (~1 hour on average).

4.2 Permeation of the gel as an analogue for clay migration during genesis

As the permeated clay gel within the sandstone cores was unable to be analysed via CT nor SEM, comparison with authigenic clay deposition was not able to be carried out.

4.3 Indentation

As seen from the results of the indentation experiments, the mechanical properties of the Berea sandstone cores are altered significantly by the presence of wet and dried gel. The discussion of the mechanism behind these alterations in each of the mechanical properties will now be presented. It should be noted, however, that due to the lack of petrographic and physicochemical data collected in this study, the proposed mechanisms must be inferred from established correlations between mechanical properties and various parameters in the literature, therefore making the matter speculative and subject to future work.

4.3.1 Ultimate strength

Whilst a body of literature exists for the analysis of the relationship between ultimate strength (i.e., the peak stress) and physicochemical properties of rocks, the strength values used in establishing these relationships have, in most cases, been determined under standardised uniaxial or Brazilian testing methods. Uniaxial testing provides uniaxial compressive strength (UCS) (ASTM, 1992) and direct ultimate tensile strength (UTS) (ASTM, 2008) measurements, whereas Brazilian tests are used for indirect tensile strength determination of core samples (ASTM, 2016). These tests are standardised (with defined sample dimensions and testing procedures) and as such, provide measurements that are directly comparable from study to study, which is, unfortunately, not the case with our indentation derived strength values, or any of the other mechanical parameters presented in this study. Nevertheless, to interpret the indentation results in a meaningful way, correlations must be established with the literature. As indentation pressure applied perpendicular to an applied surface is

considered compressive (Chen, Yan and Karlsson, 2006), the closest available analogue to the ultimate strength in this study is considered to be UCS. Indeed, Mousavi, Cheshomi and Ashtari, in 2018, showed an empirical relationship between sandstone UCS and critical transition force (CTF) of indentation, which they simply defined as the maximum force in their force-displacement graphs (comparable to the ultimate strength measurements in this study, for which dimensions have been accounted for). They observed a determination coefficient of >0.7 between UCS and CTF, which was deemed by the authors to be an acceptable linear correlation between the two.

Some of the factors that UCS has been correlated to, such as the ratio of matrix/detritus material and content of certain minerals (e.g., Chen and Hu, 2003) are not considered in the scope of this study as baseline homogeneity is assumed between our samples, and gel permeation would not have any effect on such rock properties. Such correlations will also be excluded in the discussion of the mechanisms behind alterations of other mechanical properties and instead focus will be given to properties that the gel is assumed to have a significant effect on.

Sandstones exhibiting a higher density and lower total pore volume are shown to have higher UCS values (e.g., Shakoor and Bonelli, 1991), similar to porosity, decreasing permeability is also correlated with increasing UCS (e.g., Cedola, 2017). Conversely, the presence of pre-existing fractures (or the assumed presence of microfractures in the case of the core samples in this study) significantly reduces UCS (Everall and Sanislav, 2018), and is in fact considered to be the most important factor in controlling both compressive and tensile strength, as rock most commonly fails along these pre-existing weakness planes (ibid). The effect that porosity/permeability and the presence of fractures have on UCS are interrelated. During the application of a compressive

force, microfractures will begin to propagate through structural weaknesses such as pores, leading to their collapse and eventually sample failure (Kemeny and Cook, 1991). From these observations in the literature, a mechanism for the increase in ultimate strength from non-saturated to wet-gel saturated samples can be proposed. Presuming the gel has filled all the available pore space, it is possible that as force is applied to a core sample, the gel, unable to escape from the sample due to its viscosity, will pressurise within the pores and thereby 'support' the existing pore space, preventing its collapse. This would inhibit the effectiveness of the pores in acting as stress concentrators, and as such, failure point would be reached at a higher stress value. An alternative mechanism, or a mechanism acting in conjunction with the previous one, may simply be the fact that the gel increases the density of the sample, thereby increasing its strength.

Recall that, contrary to the wet gel, there is a decrease in ultimate strength observed from non-permeated sandstone cores to those with a dried gel (Figure 44). It is speculated that this may be due to the filtering of fines, previously lodged within the pore space of the rock, during the gel permeation process, thereby increasing porosity and permeability. Unlike the wet gel, that fully occupied the pores in which it replaced the fines, the dry gel would have lost the majority of its volume when dried, leaving behind only a small residue of dried clay and salt within the pores. This residue does not provide the same 'strengthening' effect as the wet gel but rather makes the rocks comparatively weaker than those wherein the original fines occupy the pore space.

4.3.2 Displacement distance and post-peak behaviour

The mechanism behind the statistically significant increase in maximum displacement distance, or maximum strain when accounting for dimensions, from control to dry gel bearing cores will now be discussed. The stated increase in maximum displacement can primarily be attributed to longer post-peak strength regions in the stress strain curves for the dry gel samples (as seen from figure 41, 42, and 43, pages 95-97). These longer post-peak curves imply a change in post-deformation behaviour and an increase in the time it takes to fracture the cores in their entirety (which was the determined endpoint of the indentation experiments). Post-peak regions are of equal relevance to ultimate strength as they define how the rock fails, i.e., whether failure occurs in the form of stable spalling or violent rock ejection (Cai *et al.*, 2021). Whilst no literature exists (to the author's knowledge) discussing the length of the post-peak region, the angle of post-peak stress strain curves, and their implication on rock behaviour, has been investigated, with a comprehensive literature review on the topic provided by Crowder and Bawden, 2004. Based on these angles, several distinct post-peak behavioural patterns in rocks have been proposed (Figure 56).

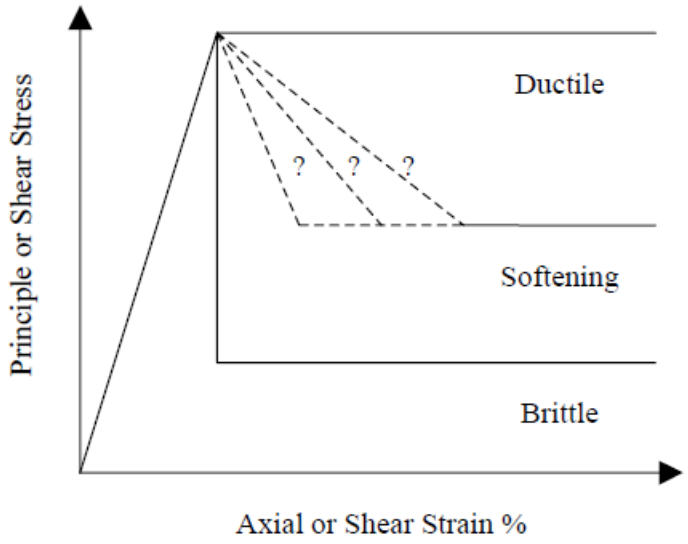

Figure 55. Post-peak behaviours of rock masses. Source: Crowder and Bawden, 2004.

Rock stress-strain curves displaying post-peak softening and brittle behaviour have been termed Class I and Class II curves, respectively (Wawersik and Fairhurst, 1970). Class I implies a gradual failure in rocks with prolonged crack propagation, whereas Class II is a near instantaneous change to residual parameters once peak-strength is reached (Crowder and Bawden, 2004). Observing the force-displacement curves from Figure 41, 42, and 43 once again, it can be seen that the angle of the post-peak curves tends to be less steep in dry gel samples than their wet gel and control counterparts (however, this is seemingly not always the case as some dry gel samples also exhibit brittle post-peak behaviour). From this general trend of greater ductility in the dried gel samples, and the apparent lack of any other relevant literature to correlate the results of this study to, the following two mechanisms are proposed. First, as the rock with the dried gel does not become cohesionless immediately after rupture, it could be assumed that the dried gel residue may act as a sort of adhesive that keeps post-fracture fragments together, thereby supporting the rock and prolonging its complete failure. The second theory is that the gel residue may deflect fractures, thus creating

a less direct fracture path through the rock and extending the time it takes for the rock to fail completely.

4.3.3 Yield strength and plasticity

The significant decrease in yield strength from control to Batch I samples, as well as the similarity between control and Batch II measurements, will now be explored. In general, yield strength has received little attention in the fields of rock engineering and rock mechanics in comparison to other mechanical properties (Diederichs and Martin, 2010), and to the author's knowledge, effects of material properties on rock yield strength values has not been explored. This can be attributed to rocks, under no confining pressure and room temperature, behaving in a brittle manner and displaying little to no plasticity. As such, UCS and yield strength values reported in the literature are often near-identical (e.g., Bratton *et al.*, 2004). Indeed, from the indentation results in this study, the difference between the mean yield strength and ultimate strength for non-permeated sandstone samples is only 3.92%. Interestingly, this is in contrast to the dry gel (Batch I) and wet gel bearing samples (Batch II), which show a 46.85% and 56.2% percentage difference, respectively, between their yield and ultimate strengths. From these results one could infer that that both types of gel permeated samples display greater plasticity than their control counterparts. The large difference in yield strength observed between control and dry gel permeated samples can be attributed to the fact that, overall, the dry gel permeated samples exhibit both a lower ultimate strength as well as plastic behaviour (meaning the yield point occurs before peak strength is reached). This is in comparison to the brittle control samples in which their higher peak strength is practically equivalent with the yield strength. In the case of the

similar yield strength values between control and Batch II samples, on average, the wet gel permeated samples seemingly start exhibiting plastic behaviour at roughly the same stress as when the control samples reach their peak force. Plasticity in the two types of gel permeated samples (examples for dry gel and wet gel samples provided in Figure 57) show contrasting behaviour. These results are further complicated by the fact that, much as in the case of post-peak behaviour, some of the gel samples (in both Batch I and II) also show brittle pre-peak behaviour, without any observable plasticity.

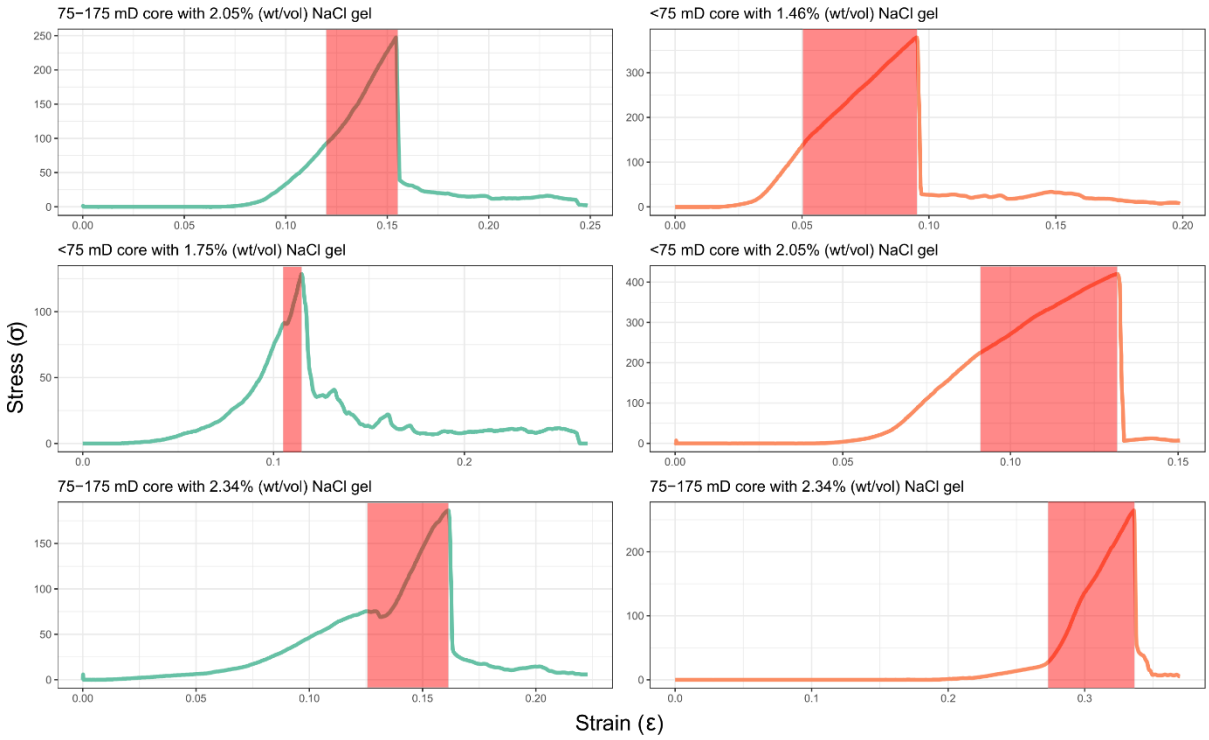

Figure 56. Strain hardening response of select samples permeated in gel. Regions between the yield strength and peak strength are highlighted. Green curves correspond to Batch I cores and orange curves correspond to Batch II.

Both Batch I and II samples that do show plasticity, exhibit a strain hardening response, which is when deformation in the rock does not localize once yield strength is achieved (as is the case in brittle behaviour), but rather, the deformation becomes widely distributed throughout the sample, allowing for rocks to sustain a larger amount of stress via ‘stable straining’ (Schultz, 2019) until ultimate strength is reached. Such

behaviour is commonly associated with increasing confining pressure and temperature as the average length of microcracks reduces under such conditions (Kemeny and Cook, 1991). What distinguishes Batch I and II behaviour from each other is that the wet gels exhibit conventional strain hardening whereby the curve becomes less steep after the linear portion, as is the case in virtually all studies assessing strain hardening in rocks (e.g., Schultz, 2019; Zinovyev, Patutin and Serdyukov, 2012; Cuss *et al.*, 2015). This is in contrast to the dry gels which exhibit a strain hardening response where the curve becomes more steep in the post-elastic region, which is highly unusual and to the author's knowledge, previously unobserved in the literature. Comparing these strain hardening behaviours, it could be proposed that the dry gel allows for a more uniform distribution of deformation throughout the sample and therefore exhibits 'greater' relative strain-hardening. The mechanisms behind the strain-hardening behaviours in the indentation tests at RTP are unable to be speculated upon due to a lack of any literature in which a similar phenomena has been observed and is therefore the subject of future work.

4.3.4 Young's modulus

The static Young's modulus (E) values of the indented cores were statistically different between all batches, with Batch II possessing the highest E and Batch I possessing the lowest. These results closely match those made for ultimate strength in both general trends and percentage differences between the batches. A significant amount of studies have investigated the correlation between UCS and Young's modulus in sandstones (e.g., Vasarhelyi, 2003; Elhakim, 2015; Farrokhrouz and Asef, 2017), with a strong, direct linear correlation having been found between the two material

properties. Additionally, many of the physicochemical and petrographic properties found to affect UCS earlier in the chapter have been found to have a similar effect on Young's modulus values (e.g., Shakoor and Bonelli, 1991). Based on the correlations between UCS and E within this study, as well as within literature, it is proposed that the mechanism behind the alteration of these properties upon the addition of either a dry or wet gel is the same.

4.3.5 Modulus of toughness and fracture energy

As both modulus of toughness and fracture energy are the areas under their respective parts of the stress strain curves, their values, for the most part, are simply a function of the aforementioned ultimate strength, displacement distance (or maximum strain), yield strength, and young's modulus. As such, the mechanism behind the changes in toughness modulus and fracture energy would be the same as those behind the mechanical parameters that define their respective areas, and are therefore not discussed separately. Additionally, as previously mentioned, direct comparison to toughness moduli and fracture energy in the literarue cannot be conducted due to an unstandardised testing method, and as such only relative differences between samples in this study can be inferred.

5. Conclusions

The work at hand was a pilot study conducted to see how simple gels consisting of only bentonite and NaCl affect rock mechanical properties in order to assess whether such a colloidal dispersion ought to be investigated further for use in wellbores to

prevent fracture propagation. These alterations in Berea sandstone mechanical properties by the permeation of bentonite gels was investigated in this study via the use of quasi-static indentation testing. Wet gel-permeated cores were found to significantly increase ultimate strength, Young's modulus, and the modulus of toughness of the sandstones, relative to their control counterparts. It is proposed that these effects are induced by the pressurisation of the wet gel within the pore space, as it is unable to escape the pores due to its viscous nature. The pressurised gel then supports the pore structure of the rock, preventing the pores from acting as stress concentrators, and thereby increasing the amount of force it takes for the sample to fail. Contrasting these results, the cores containing dried gel displayed a significant decrease in ultimate strength, young's modulus, and yield strength compared to control samples. This was attributed to filtering of the pore space, resulting in greater porosity and permeability. However, surprisingly, the dried gel bearing cores also showed an increase in both maximum displacement distance and fracture energy, implying greater resilience post-peak, with a more prominent residual stage in their stress-strain curves compared to wet gel-permeated and control samples. It is speculated that this behaviour may be due to the dry gel residue acting as an adhesive and as such, keeping the fragmented rock pieces together for longer. Alternatively, the residue could be deflecting fractures and prolonging the fracture path required for complete sample failure. It should be noted once more that due to the lack of any meaningful data in this study to correlate the mechanical findings to, the proposed mechanisms are speculative. Such data was attempted to be collected in the form of SEM and CT analysis, and while the analysis of gel bearing cores was ultimately unsuccessful using these methods, important considerations for future analysis regarding sample preparation and analysis methods were ascertained.

The study at hand shows an initial, albeit limited, set of promising results, that if studied and verified further under more scrutinous testing, could one day find use in wellbore strengthening during drilling operations. Presuming that the gel is able to be permeated effectively into reservoir rock, and that if behaves in a similar fashion under wellbore conditions, the simple colloidal clay salt dispersion could be an effective means to increase FIP and FPP.

6. Future Work

To properly validate and analyse the inferred ‘strengthening’ and ‘weakening’ effects of the wet and dry gel, respectively, significant improvements must be made to the experimental methods utilised this study (which were severely limited by COVID-19, failed experiments, and an unforeseen illness of a collaborative partner, amongst other things).

Firstly, if mechanical testing of gel permeated samples were to be attempted once more, an appropriate number of repeats for every permeability and gel concentration should be used (e.g., the required number of repeats could be determined via the central limit theorem). This is necessary as Berea sandstones display significant heterogeneity and no trends were able to be confidently established between gel concentration and mechanical properties nor between permeability and said properties. XRD also ought to be carried out to determine the mineralogical composition of the samples being indented, for example a series of XRD analyses through the depth profile of a core sample could be conducted, allowing for correlation between the mineralogical composition and the strength properties of the surface being indented. Alternatively, a synthetic rock-like material with homogeneous

properties from sample to sample, could be used instead of naturally occurring rock samples in order to assess the effects of the gels. To assess the feasibility of using the novel filter press in the future, a set of experiments comparing the press with commercially available counterparts should be carried out. The indentation testing process itself must also be made more rigorous, if indentation were to be used as the test method once more, it should be done with a purpose-built indenter, accompanied by in-situ imaging (and potentially digital volume correlation), rather than a UTM. These improvements must be made in order to obtain a more complete set of mechanical parameters (e.g., including Poisson's ratio, bulk modulus, and fracture toughness) without the need for any approximations as was the case in this study.

As sample preparation for conventional SEM analysis was found to displace the gel, environmental SEM or cryo-SEM, as well as high resolution CT, ought to be used to determine petrographic characteristics in both pre- and post-permeated core samples. In the case of CT, the same sample should be scanned pre- and post-impregnation to analyse changes to the structure. Rigorous imaging analysis would allow for correlation between changes in petrographic indices and changes observed in mechanical properties, allowing for a more meaningful analysis of the mechanisms at work. Additionally, to assess the depth of permeation of the gel within core samples, a fluorescent material or metal indicator could be added to the gel, allowing for the gel itself to be observed in CT imaging.

To further analyse the gel ageing effect, mechanical testing could be done on a series of cores in which the gel has been allowed to age incrementally from initial moisture content to completely dry (e.g., testing a core that has been allowed to dry for 3 hours at RTP, followed by a core that has been dried for 6 hours, etc). In addition, testing

under wellbore conditions (i.e., at higher temperatures and pressures) should also be considered to evaluate industry feasibility.

Some of the above-mentioned changes will be implemented in an in-progress research paper, in conjunction with the Institute for Energy and Environmental Flows of Cambridge University, planned for publication in 2023.

References

Alexiades, C. A. and Jackson, M. L. (1965) ‘Quantitative Determination of Vermiculite in Soils1’, *Soil Science Society of America Journal*. doi: 10.2136/sssaj1965.03615995002900050016x.

Allaby, M. (2013) *A dictionary of geology and earth sciences*. Oxford University Press.

Al-Yaseri, A., Zhang, Y., Ghasemiziarani, M., Sarmadivaleh, M., Lebedev, M., Roshan, H. and Iglauer, S., 2017. Permeability evolution in sandstone due to CO2 injection. *Energy & Fuels*, *31*(11), pp.12390-12398.

Anderson, R. L. *et al.* (2010) ‘Clay swelling—a challenge in the oilfield’, *Earth-Science Reviews*, 98(3–4), pp. 201–216.

Andrews, Edward, Gaetano Garfi, Ann H. Muggeridge, Alistair Jones, and Samuel C. Krevor. "Wetting alteration and oil redistribution within the pores of Berea sandstone during low salinity flooding." In *AGU Fall Meeting Abstracts*, vol. 2020, pp. H009-0003. 2020.

Anstis, G. R. *et al.* (1981) ‘A critical evaluation of indentation techniques for measuring fracture toughness: I, direct crack measurements’, *Journal of the American Ceramic Society*, 64(9), pp. 533–538.

ASTM (1992) ‘2938, Standard test method for unconfined compressive strength of intact rock core specimens’, *ASTM International, West Conshohocken, PA*.

Bailey, L. *et al.* (1998) ‘Filtercake integrity and reservoir damage’, in *SPE formation damage control conference*. OnePetro.

Baizhanov, B., Katsuki, D., Tutuncu, A.N. and Mese, A.I., 2019. Experimental investigation of coupled geomechanical, acoustic, and permeability characterization

of Berea sandstone using a novel true triaxial assembly. *Rock Mechanics and Rock Engineering*, *52*, pp.2491-2503.

Barton, C. D. (2002) 'Clay minerals', *In: Rattan Lal, comp., ed. Encyclopedia of Soil Science. New York, New York: Marcel Dekker: 187-192.*

Bello, A. M. *et al.* (2021) 'Role played by clay content in controlling reservoir quality of submarine fan system, Forties Sandstone Member, Central Graben, North Sea', *Marine and Petroleum Geology*, 128, p. 105058. doi: https://doi.org/10.1016/j.marpetgeo.2021.105058.

Benna, M. *et al.* (2001) 'Static filtration of purified sodium bentonite clay suspensions. Effect of clay content', *Applied Clay Science*. doi: 10.1016/S0169-1317(01)00050-3.

Benna-Zayani, M., Mgaidi, A., Stambouli, M., Kbir-Ariguib, N., Trabelsi-Ayadi, M. and Grossiord, J.L., 2009. Fractal nature of bentonite–water–NaCl gel systems evidenced by viscoelastic properties and model of gels. *Applied clay science*, *46*(3), pp.260-264

Billingham, J. and Ferguson, J. W. J. (1993) 'Laminar, unidirectional flow of a thixotropic fluid in a circular pipe', *Journal of Non-Newtonian Fluid Mechanics*, 47, pp. 21–55.

Bratton, T. *et al.* (2004) 'Rock strength parameters from annular pressure while drilling and dipole sonic dispersion analysis', in *SPWLA 45th Annual Logging Symposium*. OnePetro.

Caenn, R., Darley, H. C. H. and Gray, G. R. (2016) *Composition and Properties of Drilling and Completion Fluids: Seventh Edition*, *Composition and Properties of Drilling and Completion Fluids: Seventh Edition*.

Cai, M. *et al.* (2021) ‘Post-peak stress–strain curves of brittle hard rocks under axial-strain-controlled loading’, *International Journal of Rock Mechanics and Mining Sciences*, 147, p. 104921.

Cargnel, R. D. and Luzardo, J. P. (1999) ‘Particle size distribution selection of CaCO3 in drill-in fluids: theory and applications’, in *Latin American and Caribbean petroleum engineering conference*. Society of Petroleum Engineers.

Cecil, C. B. and Heald, M. T. (1971) ‘Experimental investigation of the effects of grain coatings on quartz growth’, *Journal of Sedimentary Research*, 41(2), pp. 582–584.

Cedola, A. E. (2017) ‘Using Drilling Data to Calculate Porosity & Permeability’. Oklahoma State University.

Chen, H. and Hu, Z.-Y. (2003) ‘Some factors affecting the uniaxial strength of weak sandstones’, *Bulletin of Engineering Geology and the Environment*, 62(4), pp. 323–332.

Chen, L., Xu, J. and Chen, J. (2015) ‘Applications of scanning electron microscopy in earth sciences’, *Science China Earth Sciences*, 58(10), pp. 1768–1778.

Chen, X., Yan, J. and Karlsson, A. M. (2006) ‘On the determination of residual stress and mechanical properties by indentation’, *Materials Science and Engineering: A*, 416(1–2), pp. 139–149.

Cheraghian, G. *et al.* (2014) ‘Adsorption polymer on reservoir rock and role of the nanoparticles, clay and SiO2’, *International Nano Letters*. doi: 10.1007/s40089-014-0114-7.

Churchel, P. L. *et al.* (1991) ‘Rock properties of Berea sandstone, Baker dolomite, and Indiana limestone’, in. doi: 10.2523/21044-ms.

Ciavarella, M. (1999) ‘Indentation by nominally flat or conical indenters with rounded corners’, *International Journal of Solids and Structures*, 36(27), pp. 4149–4181.

Civan, F. and Engler, T. (1994) ‘Drilling mud filtrate invasion-improved model and solution’, *Journal of Petroleum Science and Engineering*. doi: 10.1016/0920-4105(94)90039-6.

Clementz, D. M. (1976) ‘Interaction of petroleum heavy ends with montmorillonite’, *Clays and clay minerals*, 24(6), pp. 312–319.

Cook, J. *et al.* (2011) ‘Stabilizing the wellbore to prevent lost circulation’, *Oilfield Review*.

Crowder, J. J. and Bawden, W. F. (2004) ‘Review of post-peak parameters and behaviour of rock masses: current trends and research’, *Rocnews, fall*.

Cuiec, L. (1989) ‘Effect of drilling fluids on rock surface properties’, *SPE Formation Evaluation*, 4(01), pp. 38–44.

Cuss, R. J. *et al.* (2015) ‘Hydraulic fracturing: A review of theory and field experience’.

Derjaguin, B. and Landau, L. (1941) ‘Theory of the stability of strongly charged lyophobic sols and of the adhesion of strongly charged particles in solutions of electrolytes’, *Progress in Surface Science*, 43(1–4), pp. 30–59.

Dewers, T. and Ortoleva, P. (1991) ‘Influences of clay minerals on sandstone cementation and pressure solution’, *Geology*, 19(10), pp. 1045–1048.

Diederichs, M. S. and Martin, C. D. (2010) ‘Measurement of spalling parameters from laboratory testing’, in *ISRM International Symposium-EUROCK 2010*. OnePetro.

Donald, A. M. (2003) ‘The use of environmental scanning electron microscopy for imaging wet and insulating materials’, *Nature materials*, 2(8), pp. 511–516.

Donaldson, E. C. and Chernoglazov, V. (1987) ‘Characterization of drilling mud fluid invasion’, *Journal of Petroleum Science and Engineering*. doi: 10.1016/0920-4105(87)90010-6.

Duman, O. and Tunç, S. (2009) ‘Electrokinetic and rheological properties of Na-bentonite in some electrolyte solutions’, *Microporous and Mesoporous Materials*, 117(1–2), pp. 331–338.

Elhakim, A. F. (2015) ‘The use of point load test for Dubai weak calcareous sandstones’, *Journal of Rock Mechanics and Geotechnical Engineering*, 7(4), pp. 452–457.

Englehardt, J., Wilson, M. J. and Woody, F. (2001) ‘New abandonment technology new materials and placement techniques’, in *SPE/EPA/DOE Exploration and Production Environmental Conference*. OnePetro.

Evans, D. F. and Wennerström, H. (1999) ‘The colloidal domain: where physics, chemistry, biology, and technology meet’.

Everall, T. J. and Sanislav, I. V (2018) ‘The influence of pre-existing deformation and alteration textures on rock strength, failure modes and shear strength parameters’, *Geosciences*, 8(4), p. 124.

Farrokhrouz, M. and Asef, M. R. (2017) ‘Experimental investigation for predicting compressive strength of sandstone’, *Journal of Natural Gas Science and Engineering*, 43, pp. 222–229.

Feng, Y. and Gray, K. E. (2017) ‘Review of fundamental studies on lost circulation and wellbore strengthening’, *Journal of Petroleum Science and Engineering*, 152, pp.

511–522.

Feng, Y., Jones, J. F. and Gray, K. E. (2016) ‘A review on fracture-initiation and-propagation pressures for lost circulation and wellbore strengthening’, *SPE Drilling & Completion*, 31(02), pp. 134–144.

Ferrage, E. *et al.* (2005) ‘Investigation of smectite hydration properties by modeling experimental X-ray diffraction patterns: Part I. Montmorillonite hydration properties’, *American Mineralogist*, 90(8–9), pp. 1358–1374.

Fink, J. (2015) *Petroleum Engineer’s Guide to Oil Field Chemicals and Fluids*, *Petroleum Engineer’s Guide to Oil Field Chemicals and Fluids*. doi: 10.1016/c2015-0-00518-4.

Fisher, Q. J., Knipe, R. J. and Worden, R. H. (2000) ‘Microstructures of deformed and non-deformed sandstones from the North Sea: implications for the origins of quartz cement in sandstones’, *Quartz cementation in sandstones*, 29, pp. 129–146.

FPS (Federation of Piling Specialists), 2006. Bentonite support fluids in civil engineering.

Fuh, G. F. *et al.* (1992) ‘New approach to preventing lost circulation while drilling’, in *Proceedings - SPE Annual Technical Conference and Exhibition*. doi: 10.2523/24599-ms.

Gamal, H. *et al.* (2020) ‘Effect of exposure time on the compressive strength and formation damage of sandstone while drilling horizontal wells’, *Journal of Petroleum Science and Engineering*, 195, p. 107590. doi: 10.1016/j.petrol.2020.107590.

Gamal, H., Elkatatny, S. and Abdulraheem, A. (2020) ‘Effect of the Filtrate Fluid of Water-Based Mud on Sandstone Rock Strength and Elastic Moduli’, *ACS Omega*, 5(50), pp. 32677–32688. doi: 10.1021/acsomega.0c05067.

Gast, R. G. (1972) ‘Alkali metal cation exchange on Chambers montmorillonite’, *Soil Science Society of America Journal*, 36(1), pp. 14–19.

Gates, G. L. and Bowie, C. P. (1942) *Correlation of certain properties of oil-well drilling-mud fluids with particle-size distribution*. US Department of the Interior, Bureau of Mines.

Gossmann, R., Langer, K. and Mulac, D. (2015) ‘New perspective in the formulation and characterization of didodecyldimethylammonium bromide (DMAB) stabilized poly (lactic-co-glycolic acid)(PLGA) nanoparticles’, *Plos one*, 10(7), p. e0127532.

Griffith, A. A. (1921) ‘VI. The phenomena of rupture and flow in solids’, *Philosophical transactions of the royal society of london. Series A, containing papers of a mathematical or physical character*, 221(582–593), pp. 163–198.

Guéguen, Y. and Boutéca, M. (2004) *Mechanics of fluid-saturated rocks*. Elsevier.

Haimson, B. and Fairhurst, C. (1967) ‘Initiation and extension of hydraulic fractures in rocks’, *Society of Petroleum Engineers Journal*, 7(03), pp. 310–318.

Hamouda, A. A. and Valderhaug, O. M. (2014) ‘Investigating enhanced oil recovery from sandstone by low-salinity water and fluid/rock interaction’, *Energy & fuels*, 28(2), pp. 898–908.

Hannibal, J.T., 2020. Berea sandstone: A heritage stone of international significance from Ohio, USA. *Geological Society, London, Special Publications*, *486*(1), pp.177-204.

Hassenkam, T. *et al.* (2011) ‘Pore scale observation of low salinity effects on outcrop and oil reservoir sandstone’, *Colloids and Surfaces A: Physicochemical and Engineering Aspects*, 390(1–3), pp. 179–188.

Helgeson, H. C. (1968) ‘Evaluation of irreversible reactions in geochemical

processes involving minerals and aqueous solutions—I. Thermodynamic relations', *Geochimica et Cosmochimica Acta*, 32(8), pp. 853–877.

Hoek, E. and Martin, C. D. (2014) 'Fracture initiation and propagation in intact rock–a review', *Journal of Rock Mechanics and Geotechnical Engineering*, 6(4), pp. 287–300.

Howard, G. C. and Scott, P. P. (1951) 'An Analysis and the Control of Lost Circulation', *Journal of Petroleum Technology*. doi: 10.2118/951171-g.

Iassonov, P., Gebrenegus, T. and Tuller, M. (2009) 'Segmentation of X-ray computed tomography images of porous materials: A crucial step for characterization and quantitative analysis of pore structures', *Water resources research*, 45(9).

Idiart, A. *et al.* (2020) 'Hydro-chemo-mechanical modelling of long-term evolution of bentonite swelling', *Applied Clay Science*, 195, p. 105717.

Institute, A. P. (2009) 'Recommended Practice for Field Testing Water-Based Drilling Fluids'.

Irwin, G. R. (1957) 'Analysis of stresses and strains near the end of a crack traversing a plate'.

Irwin, G. R. (1958) 'Handbuch der Physik, vol. 6', *Springer Verlag (Berlin)*.

Joseph, E. and Singhvi, G. (2019) 'Chapter 4 - Multifunctional nanocrystals for cancer therapy: a potential nanocarrier', in Grumezescu, A. M. B. T.-N. for D. D. and T. (ed.). William Andrew Publishing, pp. 91–116. doi: https://doi.org/10.1016/B978-0-12-816505-8.00007-2.

Kammer, D. (2014) *Slip Fronts at Frictional Interfaces: A Numerical and Theoretical Study*. doi: 10.5075/epfl-thesis-6492.

Kareem, R. *et al.* (2017) ‘Multi-technique approach to the petrophysical characterization of Berea sandstone core plugs (Cleveland Quarries, USA)’, *Journal of Petroleum Science and Engineering*. doi: 10.1016/j.petrol.2016.09.029.

Kemeny, J. M. and Cook, N. G. W. (1991) ‘Micromechanics of deformation in rocks’, in *Toughening mechanisms in quasi-brittle materials*. Springer, pp. 155–188.

Kjellsen, K. O. *et al.* (2003) ‘Preparation of flat-polished specimens for SEM-backscattered electron imaging and X-ray microanalysis—importance of epoxy impregnation’, *Cement and concrete research*, 33(4), pp. 611–616.

Koteeswaran, S. *et al.* (2018) ‘Characterization of shale–fluid interaction through a series of immersion tests and rheological studies’, *Journal of Petroleum Exploration and Production Technology*, 8(4), pp. 1273–1286.

Krumbein, W. C. and Monk, G. D. (1943) ‘Permeability as a function of the size parameters of unconsolidated sand’, *Transactions of the AIME*, 151(01), pp. 153–163.

Kyriakou, Y., Prell, D. and Kalender, W. A. (2009) ‘Ring artifact correction for high-resolution micro CT’, *Physics in medicine & biology*, 54(17), p. N385.

Labrecque, S.P. and Blanford, W.J., 2021. Fate and transport of bromide and mononuclear aromatic hydrocarbons in aqueous solutions through Berea Sandstone. *Science of The Total Environment*, *766*, p.141714.

Lagaly, G. and Jasmund, K. (1993) ‘Tonminerale und tone’, *Struktur, Eigenschaften, Anwendung und Einsatz in Industrie und Umwelt*.

Lai, P., Moulton, K. and Krevor, S. (2015) ‘Pore-scale heterogeneity in the mineral distribution and reactive surface area of porous rocks’, *Chemical Geology*, 411, pp. 260–273.

Lal, M. (1999) ‘Shale stability: drilling fluid interaction and shale strength’, in *SPE Asia Pacific Oil and Gas Conference and Exhibition*. Society of Petroleum Engineers.

Lavrov, A. (2016) *Lost circulation: Mechanisms and solutions*, *Lost Circulation: Mechanisms and Solutions*. doi: 10.1016/C2015-0-00926-1.

Li, D. and Wang, W. (2019) ‘Quantitative analysis of the influence of saturation on rock strength reduction considering the distribution of water’, *Geomechanics and Geophysics for Geo-Energy and Geo-Resources*, 5(2), pp. 197–207.

Lichtner, P. C. (1988) ‘The quasi-stationary state approximation to coupled mass transport and fluid-rock interaction in a porous medium’, *Geochimica et Cosmochimica Acta*, 52(1), pp. 143–165.

Liu, J. *et al.* (2006) ‘A fully-coupled hydrological–mechanical–chemical model for fracture sealing and preferential opening’, *International Journal of Rock Mechanics and Mining Sciences*, 43(1), pp. 23–36.

Lu, A. *et al.* (2021) ‘Impact of moisture content on the brittle-ductile transition and microstructure of sandstone under dynamic loading conditions’, *Advances in Civil Engineering*, 2021.

Luckham, P. F. and Rossi, S. (1999) ‘Colloidal and rheological properties of bentonite suspensions’, *Advances in Colloid and Interface Science*. doi: 10.1016/S0001-8686(99)00005-6.

M’Bodj, O. *et al.* (2004) ‘Plastic and elastic properties of the systems interstratified clay-water-electrolyte-xanthan’, *Journal of Colloid and Interface Science*. doi: 10.1016/j.jcis.2004.02.028.

ASTM (2016) *Standard test method for splitting tensile strength of intact rock core specimens*. ASTM International.

Matthiesen, J. *et al.* (2014) ‘How naturally adsorbed material on minerals affects low salinity enhanced oil recovery’, *Energy & Fuels*, 28(8), pp. 4849–4858.

Mees, F. *et al.* (2003) ‘Applications of X-ray computed tomography in the geosciences’, *Geological Society, London, Special Publications*, 215(1), pp. 1–6.

Mering, J. (1946) ‘On the hydration of montmorillonite’, *Transactions of the Faraday Society*, 42, pp. B205–B219.

Miranda, C. R. *et al.* (2017) ‘Materials for controlling severe lost circulation-laboratory evaluation’, in *SPE Latin America and Caribbean Petroleum Engineering Conference*. Society of Petroleum Engineers.

Mody, F. K. and Hale, A. H. (1993) ‘Borehole-Stability Model To Couple the Mechanics and Chemistry of Drilling-Fluid/Shale Interactions’, *Journal of Petroleum Technology*, 45(11), pp. 1093–1101. doi: 10.2118/25728-PA.

Mokhtari, M. and Tutuncu, A. N. (2016) ‘Impact of laminations and natural fractures on rock failure in Brazilian experiments: a case study on Green River and Niobrara formations’, *Journal of Natural Gas Science and Engineering*, 36, pp. 79–86.

Mooney, R. W., Keenan, A. G. and Wood, L. A. (1952) ‘Adsorption of water vapor by montmorillonite. II. Effect of exchangeable ions and lattice swelling as measured by X-ray diffraction’, *Journal of the American Chemical Society*, 74(6), pp. 1371–1374.

Morita, N., Black, A. D. and Fuh, G.-F. (1996) ‘Borehole breakdown pressure with drilling fluids—I. Empirical results’, in *International journal of rock mechanics and mining sciences & geomechanics abstracts*. Elsevier, pp. 39–51.

Mostaghimi, P., Blunt, M. J. and Bijeljic, B. (2013) ‘Computations of absolute permeability on micro-CT images’, *Mathematical Geosciences*, 45(1), pp. 103–125.

Mousavi, E., Cheshomi, A. and Ashtari, M. (2018) ‘Estimating elasticity modulus and

uniaxial compressive strength of sandstone using indentation test', *Journal of Petroleum Science and Engineering*, 169, pp. 157–166.

Murthy, C. S. N. (2021) *Rock indentation: experiments and analyses*. CRC Press.

Nasiri, A. *et al.* (2017) 'Experimental and field test analysis of different loss control materials for combating lost circulation in bentonite mud', *Journal of Natural Gas Science and Engineering*, 44, pp. 1–8. doi: 10.1016/j.jngse.2017.04.004.

Odom, I. E. (1984) 'Smectite clay minerals: properties and uses.', *Philosophical Transactions of the Royal Society of London*. doi: 10.1098/rsta.1984.0036.

OFITE (2019a) 'HTHP Filter Press for Drilling Fluid Testing Instruction Manual'.

OFITE (2019b) 'Permeability Plugging Tester Instruction Manual'. Available at: https://www.ofite.com/doc/171-90_instructions.pdf.

van Olphen, H. (1964) 'An introduction to clay colloid chemistry. By H van Olphen. Interscience Publishers, Div. of John Wiley & Sons, 605 Third Ave., New York 16, N. Y, 1963.', *Journal of Pharmaceutical Sciences*. doi: 10.1002/jps.2600530238.

Oluwadebi, A. G., Taylor, K. G. and Dowey, P. J. (2018) 'Diagenetic controls on the reservoir quality of the tight gas Collyhurst sandstone formation, lower Permian, east Irish Sea basin, United Kingdom', *Sedimentary Geology*, 371, pp. 55–74.

Øren, P.E. and Bakke, S., 2003. Reconstruction of Berea sandstone and pore-scale modelling of wettability effects. Journal of petroleum science and engineering, 39(3-4), pp.177-199.

Osuji, C. E., Chenevert, M. E. and Sharma, M. M. (2008) 'Effect of porosity and permeability on the membrane efficiency of shales', in *SPE Annual Technical Conference and Exhibition*. OnePetro.

Outmans, H. D. (1963) ‘Mechanics of static and dynamic filtration in the borehole’, *Society of Petroleum Engineers Journal*, 3(03), pp. 236–244.

Parris, T.M. and Nuttall, B.C., 2021. Berea Sandstone: New developments in a mature oil and gas play, eastern Kentucky and Ohio. *AAPG Bulletin*, *105*(3), pp.485-492.

Pepper, J.F., De Witt Jr, W. and Demarest, D.F., 1954. *Geology of the Bedford shale and Berea sandstone in the Appalachian basin* (No. 259). US Geological Survey.

Pilehvari, A. A. and Nyshadham, V. R. (2002) ‘Effect of material type and size distribution on performance of loss/seepage control material’, in *International Symposium and Exhibition on Formation Damage Control*. OnePetro.

Pittman, E. D. (1972) ‘Diagenesis of quartz in sandstones as revealed by scanning electron microscopy’, *Journal of Sedimentary Research*, 42(3), pp. 507–519.

Ponomarev, A. A., Mamadaliev, R. A. and Semenova, T. V (2016) ‘Tomography in Geology: 3D Modeling and Analysis of Structural Features of Rocks Using Computed MicroTomography’, in *IOP Conference Series: Materials Science and Engineering*. IOP Publishing, p. 12030.

Razavi, O. *et al.* (2017) ‘Comprehensive analysis of initiation and propagation pressures in drilling induced fractures’, *Journal of Petroleum Science and Engineering*, 149, pp. 228–243.

Reed, S. J. B. (2005) *Electron microprobe analysis and scanning electron microscopy in geology*. Cambridge university press.

Rye, O.J., 2017. *Statistical Analysis of Rheological characterization of Water-based Drilling Fluids* (Master's thesis, NTNU).

ASTM (2008) *Standard test method for direct tensile strength of intact rock core*

specimens. ASTM International.

Safari-Zanjania, M., Whitea, C. D. and Hanorb, J. S. (2013) 'IMPACTS OF ROCK-BRINE INTERACTIONS ON SANDSTONE PROPERTIES IN LOWER MIOCENE SEDIMENTS, SOUTHWEST LOUISIANA'.

Saka, E. E. and Güler, C. (2006) 'The effects of electrolyte concentration, ion species and pH on the zeta potential and electrokinetic charge density of montmorillonite', *Clay Minerals*. 2018/07/09, 41(4), pp. 853–861. doi: DOI: 10.1180/0009855064140224.

Sarris, E. and Papanastasiou, P. (2012) 'Modeling of hydraulic fracturing in a poroelastic cohesive formation', *International Journal of Geomechanics*, 12(2), pp. 160–167.

Schapel, A. *et al.* (2018) 'Offsetting greenhouse gas emissions through increasing soil organic carbon in SA clay-modified soils: knowledge gap analysis', *Goyder Institute for Water Research Technical Report Series*, (18/05).

Schultz, R. A. (2019) *Geologic fracture mechanics*. Cambridge University Press.

Segad, M. *et al.* (2012) 'Microstructural and swelling properties of Ca and Na montmorillonite:(in situ) observations with cryo-TEM and SAXS', *The Journal of Physical Chemistry C*, 116(13), pp. 7596–7601.

Severin, K. P. (2004) *Energy dispersive spectrometry of common rock forming minerals*. Springer.

SHAKOOR, A. and BONELLI, R. E. (1991) 'Relationship between petrographic characteristics, engineering index properties, and mechanical properties of selected sandstones', *Bulletin of the Association of Engineering Geologists*, 28(1), pp. 55–71.

Sharma, M. M. and Wunderlich, R. W. (1987) 'The alteration of rock properties due

to interactions with drilling-fluid components', *Journal of Petroleum Science and Engineering*, 1(2), pp. 127–143.

Smith, S. M. and Scattergood, R. O. (1992) 'Crack-shape effects for indentation fracture toughness measurements', *Journal of the American Ceramic Society*, 75(2), pp. 305–315.

Soboyejo, W. (2002) *Mechanical properties of engineered materials*. CRC press.

Solberg, P., Lockner, D. and Byerlee, J. (1977) 'Shear and tension hydraulic fractures in low permeability rocks', *Pure and Applied Geophysics*, 115(1), pp. 191–198.

Spears & Assoc. Inc., Tulsa, O. (2004) 'Oilfield Market Report'. Available at: www.spearsresearch.com.

Steefel, C. I. and Maher, K. (2009) 'Fluid-rock interaction: A reactive transport approach', *Reviews in mineralogy and geochemistry*, 70(1), pp. 485–532.

Stöckhert, F. (2015) 'Fracture mechanics applied to hydraulic fracturing in laboratory experiments'. Ruhr-Universität Bochum.

Swaco, M. I. (2001) 'Engineering drilling fluid manual', *MI Swaco*.

Swartzen-Allen, S. L. and Matijevic, E. (1976) 'Colloid and surface properties of clay suspensions. III. Stability of montmorillonite and kaolinite', *Journal of Colloid and Interface Science*, 56(1), pp. 159–167. doi: https://doi.org/10.1016/0021-9797(76)90158-2.

Tare, M. *et al.* (2009) 'Drosophila adult eye model to teach Scanning Electron Microscopy in an undergraduate cell biology laboratory', *Drosophila Information Service*, 92.

Taud, H. *et al.* (2005) ‘Porosity estimation method by X-ray computed tomography’, *Journal of petroleum science and engineering*, 47(3–4), pp. 209–217.

Teich-McGoldrick, S. L. *et al.* (2015) ‘Swelling properties of montmorillonite and beidellite clay minerals from molecular simulation: comparison of temperature, interlayer cation, and charge location effects’, *The Journal of Physical Chemistry C*, 119(36), pp. 20880–20891.

Trefalt, G. and Borkovec, M. (2014) ‘Overview of DLVO theory’, *Laboratory of Colloid and Surface Chemistry, University of Geneva, Switzerland*, pp. 1–10.

Vasarhelyi, B. (2003) ‘Some observations regarding the strength and deformability of sandstones in dry and saturated conditions’, *Bulletin of Engineering Geology and the Environment*, 62(3), pp. 245–249.

Velde, B. (1992) *Introduction to clay minerals: chemistry, origins, uses and environmental significance.* Chapman and Hall Ltd.

Verwey, E. J. W. (1947) ‘Theory of the stability of lyophobic colloids.’, *The Journal of Physical Chemistry*, 51(3), pp. 631–636.

Veveakis, M., Stefanou, I. and Sulem, J. (2013) ‘Failure in shear bands for granular materials: thermo-hydro-chemo-mechanical effects’, *Géotechnique Letters*, 3(2), pp. 31–36.

Vipulanandan, C. and Mohammed, A. (2020) ‘Effect of drilling mud bentonite contents on the fluid loss and filter cake formation on a field clay soil formation compared to the API fluid loss method and characterized using Vipulanandan models’, *Journal of Petroleum Science and Engineering*, 189, p. 107029.

Wang, H. *et al.* (2008) ‘Best practice in understanding and managing lost circulation challenges’, *SPE Drilling and Completion*, pp. 168–175. doi: 10.2118/95895-pa.

Wang, H. Y., Marongiu-Porcu, M. and Economides, M. J. (2014) 'Poroelastic versus poroplastic modeling of hydraulic fracturing', in *SPE Hydraulic Fracturing Technology Conference*. OnePetro.

Wang, Y. *et al.* (2014) 'Meso-damage cracking characteristics analysis for rock and soil aggregate with CT test', *Science China Technological Sciences*, 57(7), pp. 1361–1371.

Wawersik, W. R. and Fairhurst, C. H. (1970) 'A study of brittle rock fracture in laboratory compression experiments', in *International Journal of Rock Mechanics and Mining Sciences & Geomechanics Abstracts*. Elsevier, pp. 561–575.

Wennberg, O. P. and Rennan, L. (2018) 'A brief introduction to the use of X-ray computed tomography (CT) for analysis of natural deformation structures in reservoir rocks', *Geological Society, London, Special Publications*, 459(1), pp. 101–120.

Whitfill, D. L. and Hemphill, T. (2003) 'All lost-circulation materials and systems are not created equal', in *SPE annual technical conference and exhibition*. Society of Petroleum Engineers.

Wu, J. *et al.* (2005) 'The influence of water-base mud properties and petrophysical parameters on mudcake growth, filtrate invasion, and formation pressure', *Petrophysics*.

Wuyep, E. O. *et al.* (2020) 'Evaluation of Interactions Between Oilfield Chemicals and Reservoir Rocks', *Natural Resources Research*, 29(2), pp. 1239–1258. doi: 10.1007/s11053-019-09523-3.

Xu, X. *et al.* (2018) 'Review of the relationships between crack initiation stress, mode I fracture toughness and tensile strength of geo-materials', *International Journal of Geomechanics*, 18(10), p. 4018136.

Yadav, P. K. *et al.* (2016) ‘Effect of drilling fluid on rock mechanical properties at near-drilling conditions: an implication of fluid design on wellbore stability’, in *Offshore Technology Conference Asia*. Offshore Technology Conference.

Young, R. (1975) *Soil properties and behaviour*. Elsevier.

Zehnder, A. T. (2013) ‘Stress intensity factors’, *Encyclopedia of Tribology*, pp. 3335–3340.

Zhang, Y. *et al.* (2022) ‘Fracture Characteristics of Sliding Crack in Brittle Rock: Analysis Based on an Improved Equivalent Crack Model’, *Frontiers in Earth Science*, 10, p. 893549.

Zhou, W. *et al.* (2006) ‘Fundamentals of scanning electron microscopy (SEM)’, in *Scanning microscopy for nanotechnology*. Springer, pp. 1–40.

Ziegler, P. A. (1983) ‘Tectonics of the North Sea Basin and their Possible Relation to Historical Earthquakes BT - Seismicity and Seismic Risk in the Offshore North Sea Area’, in Ritsema, A. R. and Gürpinar, A. (eds). Dordrecht: Springer Netherlands, pp. 3–13.

Zinovyev, A. A., Patutin, A. V and Serdyukov, S. V (2012) ‘Optimization of coal measure rocks stress relief to increase the efficiency of the degassing process: numerical modeling using FLAC software’, in *46th US Rock Mechanics/Geomechanics Symposium*. OnePetro.

Appendix

Time, position, and force values for each of the indentation experiments are provided in Excel files under the supplementary material, with the values for each Batch provided in a separate xlsx file.